RHEOLOGY AND MODELLING OF THE POLYMER ENCAPSULATION OF MIXED WASTES

by

Seth S. Gleiman

ProQuest LLC.
789 East Eisenhower Parkway
P.O. Box 1346
Ann Arbor, MI 48106 – 1346

A thesis submitted to the Faculty and the Board of Trustees of the Colorado School of Mines in partial fulfillment of the requirements for the degree of Master of Science (Chemical and Petroleum-Refining Engineering).

Golden, Colorado

Date 21 JAN 97

Signed: Seth S. Gleiman
Seth S. Gleiman

Approved: John R. Dorgan
John R. Dorgan, Ph. D.
Thesis Advisor

Golden, Colorado

Date 1/21/97

James F. Ely
James F. Ely, Ph. D.
Professor and Head,
Department of Chemical Engineering
and Petroleum Refining

ABSTRACT

The decomissioning of nuclear weapons facilities entails many facets of remediation sciences. The Rocky Flats Environmental Technology Site, formerly a nuclear bomb trigger manufacturer, has taken steps to remediate its largest (by volume) waste stream. This low-level mixed waste stream consists of nitrate salts which, due to their low bulk density in spray dried form, cannot be transported and disposed of without prior stabilizing treatment.

Polymer encapsulation is the treatment technology being investigated for remediation of the nitrate salt stream. A comprehensive understanding of the flow behavior of the filled system under various processing conditions is essential to predict extrudate behavior during waste performance testing. Major contributions of this work include: (1) The development of rheological protocol for filled system testing which eliminates spurious behaviors due to inhomogeneities in the melt state, (2) The development of a finite element model of the extruder die to investigate the flow behavior in the die region under processing conditions, and (3) The investigation of anomalous rheological behavior found in the filled system such as stress and thermally dependent filler maximum packing fractions, time and shear history dependent moduli, and yield stresses.

Experiments were performed on a parallel plate rheometer with samples of known weight percentages of salt filler dispersed in low density polyethylene via twin-screw extrusion. A filler density of 1.75 g/cm^3 was determined from the method of

Wildemuth (1984). A complex stress and thermally-dependent maximum packing fraction was elucidated: $\phi_m(\tau,\ T)$ increases with increasing τ and decreasing temperature. This was then implemented in a comparison of the experimental data with published theory on relative viscosity functionality on normalized volume fraction. Master curves from application of the time-temperature superposition principle were generated. Parameters for the Power Law constitutive equation were extrapolated and used in the finite element solution of the Cauchy momentum and energy equations. Comparison with extruder performance showed excellent agreement of the pressure drop with mass flowrate of extrudate. Particulate interactions resulted in networking structures present in the sample evidenced by hystereses and yield stresses.

TABLE OF CONTENTS

LIST OF FIGURES

LIST OF TABLES

LIST OF SYMBOLS

ROMAN SYMBOLS

a_T	shift factor used in time-temperature superposition
A	emperical parameter related to filler packing geometry
A	heat transfer area
A_o	stress equation prefactor
A_1	temperature coefficient in Power Law model
C_v	suspension specific heat [=] joule/g °C
D, D_o	scalar invariant of rate of deformation tensor
G	shear modulus for perfect Hookean solid
G'	storgae modulus [=] dyne/cm^2
G''	loss modulus [=] dyne/cm^2
k	thermal conductivity [=] watt/m °C
k_2	yield stress coefficient
K	consistency parameter in Power Law model
$\dot{M}$	mass flow rate [=] kg/hr
$m_{filler,polymer}$	mass of filler and polymer, respectively [=] kg
n	power law index
ΔP	pressure drop [=] psi
q	heat flux based on Fourier's Law [=] W/m^2

r	radial coordinate
t	time [=] sec
$t_T, t_{T_\circ}$	time required to reach viscous response [=] sec
$T, T_\circ$	temperature; reference temperature [=] °C
$v_{r,z}$	velocity components
$V_{filler,polymer}$	volume of filler and polymer, respectively [=] m^3
Y	yield stress from Casson's equation [=] dyne/cm^2

GREEK SYMBOLS

α'	crowding effect arising from non-uniform particle size
β'	hydrodynammic constant
$\gamma, \gamma_\circ$	strain (dimensionless)
$\dot{\gamma}$	strain rate [=] s^{-1}
δ	phase angle
Δ	shear rate tensor
ϵ_a	particle packing constant
η	viscosity, steady state viscosity [=] poise
η^*	complex viscosity [=] poise
η_m	matrix viscosity [=] poise
η_r	relative viscosity (dimensionless)
η_s	suspension viscosity [=] poise
λ_c	characteristic chain relaxation time [=] sec
$\rho_{filler,polymer}$	filler and polymer densities, respectively [=] kg/m^3
τ, τ_s	stress, shear stress [=] dyne/cm^2

ϕ filler volume fraction (dimensionless)

ϕ_m filler maximum packing fraction (dimensionless)

ω oscillatory frequency [=] rad/sec

Chapter 1

INTRODUCTION

1.1 Preface

The flow of filled systems is an increasingly important technological area. Generally, and for use in this work, a filled system can be defined as a heterogeneous mixture containing a solid particulate material dispersed in a liquid carrier matrix. Filled systems are found in many industrial applications including ceramic pastes, cements, foodstuffs, slurry flow in pipelines, the manufacture of composite materials, solid rocket fuel manufacture, and in wastewater treatment processes.

Particle-filled polymer melts are a distinct type of filled system. Fillers are added to polymer melts for pigmentation, material property enhancement (strength, durability, flexibility, dimensional stability), or to reduce raw material cost without sacrificing final product physical performance. Common fillers include carbon black and titanium dioxide as pigments, glass fibers used in polyester resins form fiberglass, and fillers such as talc, calcium carbonate, mica, and silica often reduce costs.

Particle-filled systems are found in many polymer processing applications. Most filled polymers are compounded in an extruder (a mixing and pumping device). The extruder intimately mixes unfilled polymer with filler in the appropriate physical form so that the latter is dispersed evenly through the melt, ensuring a uniform product for further processing applications. The extrudate, usually produced in

pellet form, is commonly used as feedstock for other applications such as injection molding. In this secondary operation, the pre-mixed polymer composite is re-melted and forced into a mold under intense pressure where the polymer cools and hardens. The mold is then opened and the composite plastic form is removed. Some examples of injection molded products where fillers are present include computer housings, automobile bumpers and hoods, and consumer electronics components.

Filled polymer systems are also found in environmental remediation operations. Here, the polymer is used to physically immobilize and encapsulate waste material to ensure containment, minimize release probability and provide ultimate storage (Dorgan et al. 1995). As a physical treatment procedure, polymer encapsulation does not reduce the toxicity level of the waste component yet minimizes potential leaching into groundwater. Specific application of the encapsulation process is being performed on a nitrate salt mixed-waste stream at the U. S. Department of Energy (DOE) Rocky Flats Environmental Technology Site (RFETS). The waste salt stream, in the form of a highly-dispersible spray-dried particulate, is well-suited for polymer encapsulation procedures. This conforms to Department of Transportation (DOT) and Environmental Protection Agency (EPA) regulations protecting human health and the environment from potential hazardous waste release during transport and disposal. The spray-dried salt is added to a molten polyethylene stream and is then dispersed throughout the polymer with the aid of a twin-screw extruder. Cooled samples of the uniform composite material are subjected to EPA mandated Toxicity Characterization Leaching Procedure (TCLP) tests for waste containment.

1.2 Technical Contributions

There are many significant contributions from this research project. New procedures are developed for rheological testing of filled polymer systems. The

diversity and complexity of the rheology of filled polymer systems are demonstrated. Comparison with established relative viscosity models of filled polymeric melts are also demonstrated from results of the work presented herein.

This work also represents important technology development in polymer encapsulation and hazardous waste remediation at RFETS. A state-of-the-art level of understanding of the macroscopic behavior of the filled polymer system is demonstrated through the agreement observed between flow modelling and experimental results obtained during an extrusion process.

Chapter 2

BACKGROUND

The background is structured as three primary literature review sections based on the complex melt rheology and analysis of filled systems. First, a background of the need for filled polymer melt rheology is given. The second section reviews the literature concerning the development and application of various relative viscosity models. Third, rheological behavior of filled systems is discussed in terms of the rheological responses *specifically* due to interactions of the filler particles with other filler particles and with the polymer matrix. The concept of a stress-dependent maximum packing fraction (ϕ_m) is introduced and discussed. Finally, a brief discussion of the use of the Finite Element Method for fluid dynamics analysis is given.

2.1 Filled Polymer Melt Rheology

Composite materials, defined as having two or more components and two or more phases, are found throughout the polymer industry. Typical filled systems can be generalized into three classes: (1) particulate-filled materials consisting of a continuous matrix phase and a discontinuous filler phase made up of discrete particles, (2) fiber-filled composites, and (3) skeletal or interpenetrating network composites consisting of two continuous phases (Nielsen 1994). The samples examined in this work are of the first group.

Many commercial polymeric materials are composites such as those used in wire coatings, automobile tires, thermosetting resins, and glass or graphite fiber-filled plastics. The wide commercial and industrial use of filled polymeric composites has resulted in a increased demand for accurate and reliable rheological data. The complex behavior inherent to filled polymeric composites makes description of system flow behavior more difficult, as the properties of the composite materials are determined by the properties of the components, the shape of the filler phase, the morphology of the system, and the nature of the interface between the phases (Nielsen 1994).

As stated, filled polymer composites are now commonly used in environmental remediation processes, specifically at the RFETS. Recently, Chang (1996) and co-workers studied the rheology of the neutralized acid waste stream at the DOE-Hanford site. The authors found characterization of the stream difficult, mainly because of the non-equilibrium nature of the strongly flocculated suspension structure. Yet, this type of rheological characterization is extremely important, as the material must be transported for further treatment and vitrification on the Hanford site. Similarly, the rheological properties of the encapsulated waste stream at the RFETS must be well-known to reduce the potential of hazardous material release during processing and transportation of the final wasteform.

An important step in the rheological characterization of the filled polymer melt is the determination of the material response to increased filler loading levels. It is economically advantageous to fill the polymer with a maximum amount of salt. Yet, the rheological properties of a highly filled system differ greatly from those a nearly unfilled system. This response is typically elucidated through analysis of the relative viscosity of the polymeric composite.

2.2 Relative Viscosity

The viscosity enhancement of a suspending medium due to the presence of particles has been studied since Einstein's (1956) early work on dilute suspensions of spheres. Since then, many authors have experimentally investigated the rheology of polymer solutions and melts filled with materials such as glass beads and balloons, carbon black, calcium carbonate, titanium dioxide, polystyrene beads and fumed silica. In these studies, the filler particle size distribution was usually either monomodal or bimodal. The particle diameters ranged from nanometers in the case of fumed silica to millimeters in the case of polystyrene beads and glass spheres in solvents ranging from water to mineral oil.

The addition of filler particles to a polymeric solution or melt has long been known to increase the viscosity of the resultant dispersion. Based on the volume fraction of filler, several constitutive equations for the relative viscosity of the dispersion have been developed. Einstein's original equation for relative viscosity (η_r) states that

$$\eta_r = \frac{\eta_s}{\eta_m} = 1 + 2.5\phi \tag{2.1}$$

where η_s is the viscosity of the suspension, η_m is the viscosity of the unfilled matrix, and ϕ is the volume fraction of filler. Equation 2.1 is an accurate representation of the behavior of the suspension only over a vanishingly small range of solids concentrations (Metzner 1985). As a result, many alternative equations have been proposed for the relative viscosity of suspensions of spheres up to moderate or high concentrations.

Maron and Pierce (1956) developed a relative viscosity relationship based on the volume fraction of latex particles suspended in water. They found the relative

viscosity η_r, neglecting higher order terms in volume fraction (ϕ), to be

$$\eta_r = \frac{1}{(1 - \epsilon_a \phi)^2}, \tag{2.2}$$

where ϵ_a is a temperature-independent constant dependent only on the packing of the spheres and the particle size distribution. They found only satisfactory agreement between experimental data and their relative viscosity expression (Equation 2.2).

Frankel and Acrivos (1967) derived the functional dependence of relative viscosity on uniform solid sphere concentration from an asymptotic model based on the viscous dissipation on energy within the narrow gaps separating the various solid spheres from one another. In the limit of maximum concentration, Frankel and Acrivos showed

$$\eta_r = \frac{9}{8}\left[\frac{(\phi/\phi_m)^{\frac{1}{3}}}{1 - (\phi/\phi_m)^{\frac{1}{3}}}\right] \text{ as } \phi/\phi_m \to 1, \tag{2.3}$$

where ϕ_m is the maximum packing fraction of filler particles. Notice that as $\phi/\phi_m \to 1, \eta_r \to \infty$ indicating that as the solids fraction is increased, the composite material response tends toward solid-like behavior with infinite viscosity. Metzner (1985) found this to be the only theoretical equation which correctly predicts trends in the region of high concentrations.

To account for non-uniform filler particle structures, Mooney developed an expression for the relative viscosity shown in Equation 2.4.

$$\ln \eta_r = \frac{\beta' \phi}{1 - \alpha' \phi} \tag{2.4}$$

α' represents the crowding effect arising from the packing of non-uniform particle size and β' is the hydrodynamic constant defined by Einstein. The Mooney equation was shown by Kataoka and coworkers (1978) to fit experimental data below about $\phi = 0.4$. Furthermore, Kataoka used a scaling argument to develop an essential result regarding the calculation of relative viscosity.

Kataoka et al. (1978) demonstrated that flow curves could be superimposed by a shift along the viscosity axis through a factor f, such that $\eta = (\tau_s / f\dot{\gamma})$, where τ_s and $\dot{\gamma}$ are the shear stress and shear rate, respectively, calculated at a *constant shear stress level.* By this scaling, the relative viscosity curves then reached asymptotic or constant values for shear stresses above about 10^4 poise. Kataoka further showed that relative viscosity values calculated from measurements at the *same shear rate* levels did not reach asymptotic values.

Kitano et al. (1981) intensely studied the Maron and Pierce equation and found excellent agreement with a wide array of experimental data. The authors employed Equation 2.2 where ϵ_a was replaced with the parameter A, as shown in the following equation:

$$\eta_r = \frac{1}{(1 - \phi/A)^2}. \tag{2.5}$$

The parameter A was related to the packing geometry of the filler, i.e. the value of A decreased with an increasing aspect ratio in the fiber-filled systems. A comparison of relative viscosity models is presented in Figure 2.1.

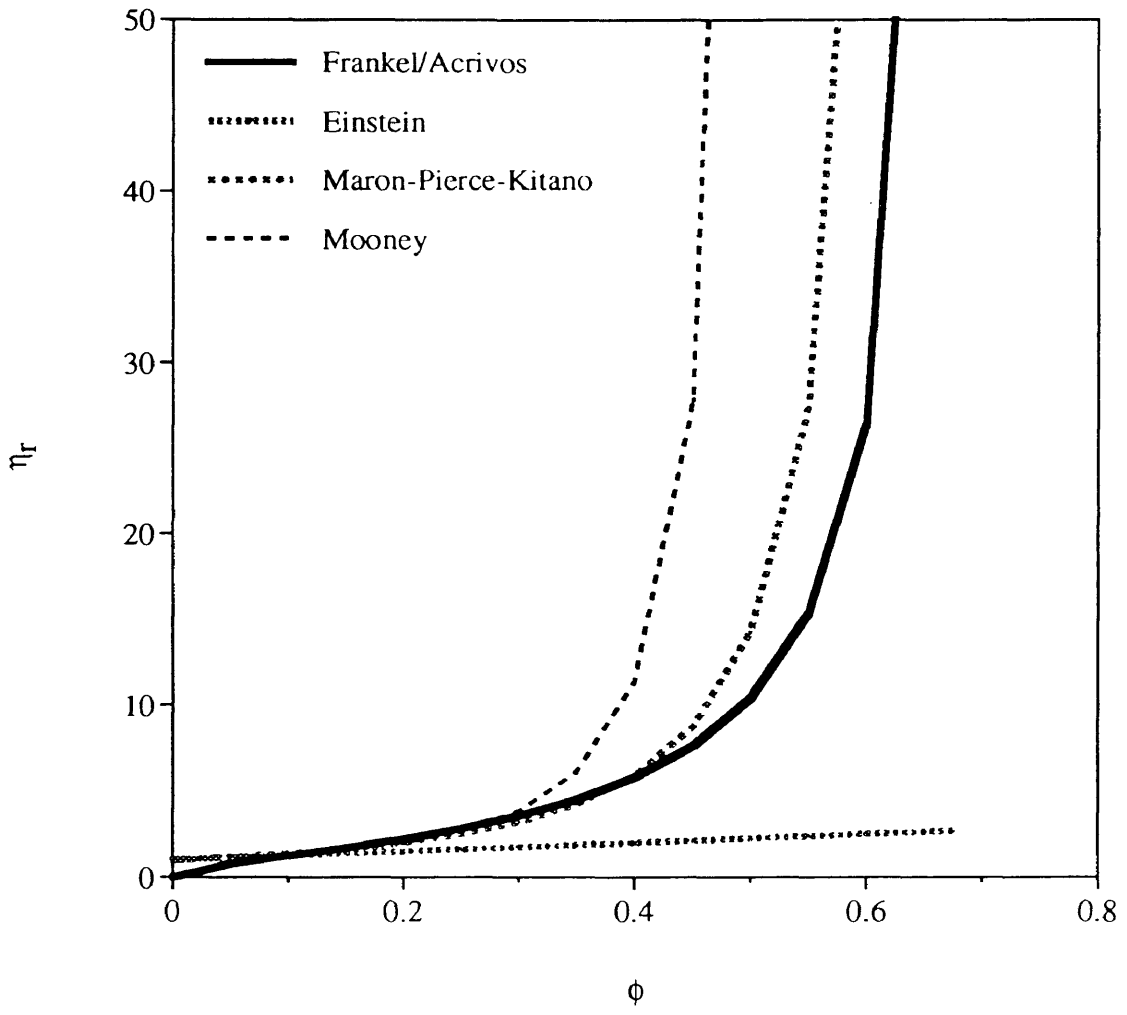

Figure 2.1: Relative viscosity (η_r) versus filler volume fraction (ϕ). This suggests the rheological behavior predicted by the theoretical expressions discussed. ($\phi_m = A = 0.68$)

When the filler exhibits a particle size distribution for the same volume fraction of filler particles, the relative viscosity of the mixture decreases with increasing polydispersity (Farris 1968, Metzner 1985, Chang 1994). Smaller particles can occupy the interstices between larger particles, thus increasing the maximum packing density (the value of A in Equation 2.5). This result is more striking when the filler particle size ratio is high, as seen in Table 2.1.

Modality	Relative Viscosity, η_r
Uni	1200 (from Eq. 2.5)
Bi	51
Tri	30
Tetra	23

Table 2.1: Relative viscosity of multimodal dispersions at constant volume fraction $\phi = 0.66$ (Taken from Metzner (1985)).

The literature base on filled system rheology is extensive. The papers referenced make up a small fraction of those used to develop a comprehensive understanding. For convenience, the reviewed literature covering experimental determination of complex rheological behavior of filled systems is presented in Table 2.2 on page 23.

Summary

The determination of mixture relative viscosity as a function of filler volume fraction has been studied extensively. A multitude of polymer/filler combinations have been investigated since Einstein's work with dilute suspensions of non-interacting spheres. Researchers have had moderate success in the development of

constitutive equations for relative viscosity. The equation of Maron and Pierce modified by Kitano et al. has been shown to predict relative viscosity very well, with only a single parameter based on the packing of the filler particles.

It has been demonstrated that rheological behavior of filled systems is extremely dependent on the type of filler particle present in the mixture. Many times, the rheology of the system is confounded by the presence of the filler due to filler interactions within the polymer matrix. Some fillers have a tendency to aggregate and flocculate, thereby modifying the maximum packing fraction and ultimately changing the relative viscosity of the composite. These flocs are fragile; upon shearing, the flocs can break apart causing an increase in the maximum packing fraction. Other fillers, specifically fibers and rods, tend to cause anisotropy within the melt after a period of steady shear making rheological characterization more difficult. The effect of filler interactions on melt rheology will be discussed in the next section.

2.3 Particulate Phase Interactions

The mechanical response of a dispersion is influenced by the presence of macroscopic agglomerates and flocculates. Also, the inclusion of suspending fluid in the aggregates and flocculates artificially increases the filler loading level, further effecting a modified mechanical response. If the filler concentration is high, i.e. $\phi \rightarrow \phi_m$, the rheological behavior of the dispersion may be dominated by the relaxation of the flocs and agglomerates disrupted while under shear. This section outlines experimental work investigating the nature of the particulate phase interactions and the associated difficulties in measuring rheological behavior of filled melts. Although the macroscopic behavior of filled melts is understood, the microscopic mechanisms believed responsible for such behaviors are not well characterized.

First, some important IUPAC terms used by Mewis and Spaull (1976) will be used throughout the discussion to describe the filled system components. A *colloidal system* is a two-phase system of interacting particles whose particles are influenced by Brownian motion. A *suspension* is a heterogeneous two-phase system of buoyant particulate solid, not colloidal, distributed in a continuous liquid. A *dispersion* is a two-phase solid in liquid system in which the particles are colloidal. An *aggregate* is a tight cluster of particles, strongly held together, so that it cannot be disrupted in a given rheological experiment. A *floc or flocculate* is a loose, thermodynamically metastable structure of colloidal particles. A floc may be destroyed by the application of stresses in a given rheological experiment and may reform when these stresses are removed.

2.3.1 Nature of the Particle Interaction

Particulate phase interactions can be dictated through hydrodynamic and colloidal effects, particle shape, surface morphology, and surface charge interaction. Each may influence the behavior of the composite material differently such that a given response may be due to a combination of two or more interactions.

Hydrodynamic effects mainly result from the presence of solid particles in the flowing medium (Mewis 1976). Under shear, the particles act as energy sinks, increasing the dissipation in the melt evidenced as a modification of the rheological properties. The amount of energy dissipation is dependent on the shape, size, and concentration of the solid filler material. If the particles are primarily in flocs, then upon the application of shear the flocs will absorb the stress (energy) by breaking into smaller aggregates. Under certain conditions, the particles may arrange themselves in streamlines through the interaction of a particle with the wake of a

neighboring particle. Particles may also migrate across streamlines due to a concentration gradient, interparticle interaction frequency, or Brownian motion. Sergé and Silberberg (1962) were the first to report this phenomena during their study of spherical rigid particles in Poiseuille flow. Phillips et al. (1992) developed a constitutive equation which accounts for the migration of particles under shear. They found that particles tend to migrate towards regions of low shear rate from high shear rate.

Colloidal stability in dispersion rheology has also been studied. Colloidal effects have mainly been attributed to particle surface morphology and surface chemistry (Mewis 1976). The interparticle forces, due to London-van der Waals forces, electrostatic attraction or repulsion, hydrophillicity or hydrophobicity, are a direct consequence of the surface chemistry of the particle. For example, particles may tend to aggregate if their surfaces exhibit polar character while the matrix polymer is non-polar, similar to micelle formation in solution.

In terms of a mechanistic understanding of the aggregate and flocculate formation, Doi and Chen (1989) performed Stokesian dynamics computer simulations of aggregating colloids in shear flow. Doi implemented a "sticky-sphere" model which assumed the colloidal spheres would stick to each other until the critical attractive force between stuck spheres is exceeded due to a particle collision. Results of their simulations showed that cluster shape changed from compact flocs to loose networks with increases in concentration and decreases in shear rate. Implementation of simulation methods including Brownian, Stokesian, and Molecular Dynamics to elucidate microscopic mechanisms in filled systems has a broad history and is beyond the scope of this thesis.

2.3.2 Experimental Evidence of Particle Interaction

As previously discussed, filler particles enhance the rheological properties of composite materials through energy (viscous) dissipation. Fillers also exhibit their collective solid-like character through rheological responses such as stress-dependent maximum packing fractions, moduli plateaus, yield stresses in the melt, shear history dependence, and time dependent moduli. If the filler is rod shaped or fibrous the material may also exhibit anisotropy.

The filler material present in the suspension may interact strongly enough to behave as a solid. Theoretically, this is known as a Hookean solid. Perfect Hookean solids have constant shear moduli G, independent of applied strain γ. The stress τ is then computed as in Equation 2.6,

$$\tau = G\gamma. \tag{2.6}$$

As the structure increases throughout the melt, the solid-like response dominates and the material exhibits an increase in the viscosity. At low shear levels flocculated particulate structures may support the internal stresses. Yet, the application of shear has the potential to break down metastable flocculated structure. When the applied strain exceeds the maximum supportable strain of the flocculated material the structure subsequently fails and breaks apart. At this point, the behavior of the material becomes dominated by the hydrodynamics of the polymer phase modified with filler particles.

2.3.2.1 Stress-Dependent Maximum Packing Fraction

The concept of a stress-dependent maximum packing fraction originates from the breakup of flocculated internal structure. This can be followed in Figure 2.2.

Under low stresses the flocs may not break apart uniformly, resulting in large aggregates. Even if the aggregates are uniformly shaped, they will have a low maximum packing fraction due to the large void spaces between packed bodies (See Figure 2.2a). Higher levels of stress cause further breakdown of the remaining flocs as well as some aggregates (Figure 2.2b). These smaller particles can pack together more efficiently, some in the interstices between larger particles, partially due to their more regular shape. A moderate level of packing efficiency denoted by an increased maximum packing fraction is then evident. At the highest stress levels, the aggregates begin to breakup into their primary particles (Figure 2.2c). The packing efficiency is maximized through more regularly shaped particles of smaller size. This corresponds to a higher maximum packing fraction.

Numerous experiments have shown different packing structures and hence different maximum packing fraction values (Chong et al. 1971). Raghavan and Khan (1995) performed rheological experiments on suspensions of fumed silica in mineral oil and polyethylene glycols. They found that "gel-like" behavior at high silica concentrations was primarily due to the formation of a network consisting of interconnected silica flocs. Raghavan also found the reformation of network flocs, based on G' measurements, depended strongly on the amplitude of imposed pre-shear strain. Determination of ϕ_m for monodisperse, well-behaved samples as well as highly polydisperse, irregularly shaped particles has been shown to be a straightforward manipulation of well-known theoretically-obtainable results (Wildemuth 1984).

Tsutsumi et al. (1994) used an extension of the Robinson equation (see Equation 2.7) to develop plots of $\phi/(\eta_r - 1)$ versus ϕ which depicted accurate values of the maximum packing fraction of coal-oil mixtures (COM).

$$\eta_r = 1 + \frac{k'\phi}{1 - \phi/\phi_m} \tag{2.7}$$

Tsutsumi showed a thermal dependence of the maximum packing fraction; higher

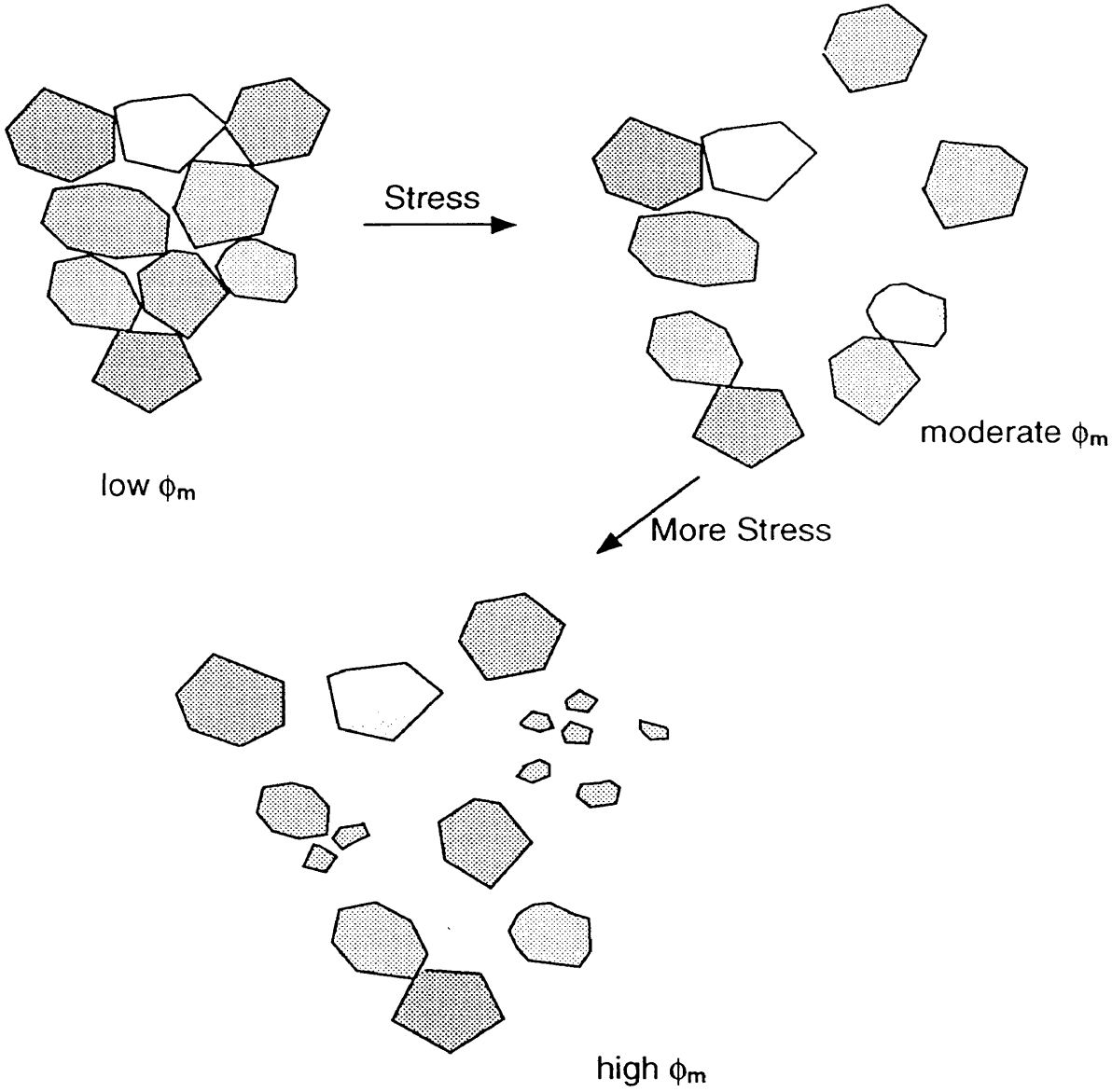

Figure 2.2: Cartoon depiction of stress-dependent maximum packing fraction.

temperatures caused increased values of ϕ_m in the COM. The stress dependence of ϕ_m was not discussed, although the slope of lines of $\phi/(\eta_r - 1)$ versus ϕ increased with increasing shear rate. In this analysis, the stress dependence is contained in the parameter k' which decreased to a constant value with increasing shear rate. This implies that the agglomerates become more regularly shaped with increasing shear rate.

Recently, researchers have used this technique to aid in the characterization of Hanford neutralized current acid waste simulant slurries (Chang et al. 1996). In their analysis, the authors used the technique of Tsutsumi yet incorporated the weight fraction (w) instead of volume fraction because of the difficulty in obtaining the density of the NACW simulant particles due to their hydrated and flocculated nature.

A similar graphical analysis technique was used by Wildemuth and Williams (1984) to predict shear dependence of ϕ_m. They suggested that most system parameters (shape effects [S], charge potential [e]) are manifested in the maximum packing fraction since $\phi_m = \phi_m(S)$. Most significantly, Wildemuth proposed, ϕ_m reflects the state of aggregation. Wildemuth examined the non-Newtonian data of Maron and coworkers on latex spheres in terms of the empirical Eilers model (see Equation 2.8). Manipulation of this expression led to the following for ϕ_m determination:

$$\eta_r = \left[1 + \frac{0.5[\eta]\phi}{1 - \phi/\phi_m}\right]^2 \tag{2.8}$$

$$\frac{(\eta_r^{\frac{1}{2}} - 1)}{\phi} = \frac{1}{\phi_m}(\eta_r^{\frac{1}{2}} - 1) + 0.5[\eta], \tag{2.9}$$

where $[\eta]$ is the intrinsic viscosity of the polymer. A plot of $(\eta_r^{\frac{1}{2}} - 1)/\phi$ versus $(\eta_r^{\frac{1}{2}} - 1)$ should therefore produce a line with slope equal to $1/\phi_m$ and intrinsic viscosity $[\eta]$.

2.3.2.2 Moduli Plateaus, Yield Stresses, and Transients

Low frequency moduli plateaus have been observed in systems such as calcium carbonate filled polypropylene. Li and Masuda (1990) investigated the build up of calcium carbonate structures in the melt through successive shearing experiments. Three sequenced tests were conducted from high to low shear rate under small strain. The viscoelastic behavior at high shear rate was dominated mainly by the matrix polymer. The structure buildup was evident as an increase in the storage modulus to a shear rate-independent value. The authors concluded that a particulate network structure may be formed from small amplitude oscillations at high temperatures and that the structure was broken up by high shear rates. Recently, Raghavan and Khan (1995) showed instantaneous reformation of the network structure in fumed silica/mineral oil and fumed silica/polypropylene glycol suspensions at cessation of shear. They found that the resultant storage modulus plateau was also shear history dependent. The authors hypothesized that large oscillatory shearing caused the network structure to be broken into smaller flocs which formed a stronger, more highly branched solid-like structure at shear abatement.

The existence of an apparent yield stress in filled polymer systems has been examined. Originally, Casson (as referenced in Matsumoto 1970) showed that the yield stress Y, proposed for a Newtonian fluid modified with filler, could be determined from Equation 2.10:

$$\tau_s^{1/2} = Y^{1/2} + k_2\dot{\gamma}^{1/2}, \tag{2.10}$$

where τ_s was the shear stress and $\dot{\gamma}$ the shear rate. For non-Newtonian fluids, the equation must incorporate the system relative viscosity (Equation 2.11).

$$\tau_s^{1/2} = Y^{1/2} + k_2(\frac{\eta_s}{\eta_m}\dot{\gamma})^{1/2} \tag{2.11}$$

Lobe and White (1979) used another technique to determine the yield stress of a carbon black filled polystyrene melt. The authors showed that yield stress could be measured from a plot of viscosity versus shear stress. They reasoned that at the point at which the curve turned toward infinity, the material had transitioned into a solid characteristically exhibiting an infinite viscosity. Further studies showed yield stress values to be particle size dependent, with smaller particles leading to higher yield stresses.

One feature of concentrated dispersions is the appearance of considerable transient behavior upon instantaneous changes in the kinematics of the flow. This response can be described by an initial stress overshoot, and increases or decreases of moduli with time. For samples with dispersed particles, this time-dependent behavior is usually associated with the reversible breakdown or formation of particulate structure. Li and Masuda (1990) showed that the gradual flocculation of particles in the melt state led to an increase in the dynamic storage modulus over the time of the experiment. Conversely, Lobe and White (1979) showed that if a network structure of particles exists in the melt prior to shearing, the modulus will decrease over time to a finite value.

2.3.2.3 Thermal Simplicity

Han et al. (1993, 1987, 1985) showed that experimental rheological data for different concentrations of a minor component is only meaningful as long as the morphology of the system remains the same over the temperature range of interest. Han demonstrated that plots of $\log G'$ versus $\log G''$ are very sensitive to variations in the morphological state of multicomponent polymer systems. Although Han focused specifically on the time-temperature superposition (discussed in Section 4.3 beginning on page 56) of polymer blends and multiphase polymer systems, his

analysis has been extended to the particulate filled system in this study.

In Han's description, rheological data for multiphase polymer systems should collapse to a single line on a plot of $\log G'$ versus $\log G''$ if the system is truly temperature-independent over the range of frequencies tested. This behavior indicates the morphological consistency of the system at various temperatures; the ability to apply the superposition principles is therefore valid.

Summary

The presence of small particles in the melt has been shown to alter the rheological behavior of the system. Significant to rheological behavior is the nature of particulate interactions. The interaction of billiard ball-type particles is dictated mainly through flow field hydrodynamics and the presence of other particles in the melt. If the particles interact through electrostatics, surface morphology or chemistry, the behavior of the melt will be affected through colloidal interactions.

Many researchers have published experimental results on the effect of interacting fillers on rheological properties. Particulate interactions have been shown to cause stress-dependent maximum packing fractions, moduli plateaus, yield stresses and time-dependent behavior. Thermal simplicity must also be obeyed for correct rheological superposition. Elucidation of these complex behaviors and determination of the interaction mechanisms are two problems associated with the analysis of filled systems.

2.4 Finite Element Method Analysis

The Finite Element Method (FEM) has seen widespread use in many engineering fields. Of particular interest to the fluid flow engineer, the FEM has the

ability to treat complex 2-D, axi-symmetric, and 3-D flow domains and boundary conditions. Specifically, the flow field in a twin screw extruder is extremely complex and lends itself well to mesh discritization and finite element analysis. Yang and Manas-Zloczower (1992) studied the kneading disc region in a co-rotating twin screw extruder with the FIDAP package. The finite element method has also been used to analyze the flow field and transport characteristics of specific extruder elements (Sastrohartono et al. 1990a, 1990b, 1994).

FIDAP (Fluid Dynamics Analysis Package) v7.0 is manufactured by Fluid Dynamics International, Inc., and is an integrated UNIX-based computation fluid dynamics (CFD) environment for the simulation of fluid flow problems. The program can be viewed as an integrated set of components and program modules designed to perform all aspects of the model generation, problem setup, solution phases, and post-processing of a flow analysis. FIDAP employs the FEM for the solution of the set of governing differential equations.

The FEM is unique in that it discritizes complex flow geometries to many smaller simple ones, called finite elements. The governing partial differential equations (see Table 3.1) are then replaced by ordinary differential (in the case of transient flows) or algebraic (for steady state flow) equations in each finite element. This system of equations is then solved through matrix inversion using LU (lower triangle-upper triangle) decomposition for the set of undetermined coefficients. These coefficients appear in polynomial approximations of the velocity, temperature, pressure, species concentration or any other unknown throughout the region. FIDAP has an extensive library of finite elements. The interpolating functions (approximating polynomials) are of either linear or quadratic functional form, while the elements range from (4, 8, 9 node) quadrilaterals and (3, 6, 7 node) triangles in 2-D to (8, 27 node) bricks, (4, 10 node) tetrahedrons, and (6, 18 node) wedges in 3-D.

Summary

The ability to numerically solve the differential equations for flow in complex geometries lends itself well for use in applications such as twin screw extrusion. The FEM is robust; the accuracy of the solution depends on the degree of the approximating polynomial and the number of finite elements used to discritize the flow domain. Standard computational packages, like FIDAP, have made analysis of fluid flow patterns more exact, providing insight into mixing behavior in flow fields. For filled system applications, computational fluid dynamics has the potential to trace particle movement, allowing manipulation of the flow field for desired product morphology without expensive machining and experimental costs.

Reference	Polymer	Filler
(Mills, 1971)	polystyrene	glass sphere
		glass rod
		nylon rod
	polyethylene	platelets
		colloidal silica
(Nicodemo and Nicolais, 1974)	polyisobutylene (in decalin)	glass bead
(Faulkner and Schmidt, 1977)	polypropylene	glass bead
(Kataoka et al., 1978)	polyethylene	glass bead
	and polystyrene	glass balloon
		silas balloon
(Lobe and White, 1979)	polystyrene	carbon black
(Tanaka and White, 1980a)	polystyrene	calcium carbonate
		titanium dioxide
		carbon black
(Kitano et al., 1981)	polyethylene	glass fiber
		carbon fiber
		calcium carbonate
		talc
	polypropylene	carbon fiber
(Suetsugu and White, 1983)	polystyrene	calcium carbonate
(Kitano et al., 1984)	polyethylene	glass fiber
(Ottani et al., 1988)	polyethylene	calcium carbonate
(Poslinski et al., 1988)	polybutene	glass spheres
(Li and Masuda, 1990)	polypropylene	calcium carbonate
(Park et al., 1990)	polystyrene	crosslinked PS beads
(Tsiprin et al., 1992)	polyethylene	chalk
		ground limestone
(Chang and Powell, 1994)	silicone fluid	polystyrene spheres
		polymethyl methacrylate beads
(Acrivos et al., 1994)	glycerine	polymethyl methacrylate
	and water	beads
(Mamunya et al., 1994)	polyethylene and polypropylene	carbon black
(Tsutsumi et al., 1994)	oil	coal particles
(Raghavan and Kahn, 1995)	mineral oil and propylene glycol	fumed silica

Table 2.2: Source list of publications based on experimental characterization of filled system rheological behavior.

Chapter 3

EXPERIMENTAL METHODS AND MATERIALS

3.1 Research Objectives

The research objectives for this thesis include comprehensive characterization of the rheological properties of the filled system, the successful generation of a continuum scale transport model and subsequent numerical simulation of the die region of the twin-screw extruder, and a comparison of the results from the numerical simulations and actual extruder operation diagnostic data collected during sample generation. The rheological data will be used to parameterize the constitutive equation in the numerical model. Numerical solution of the continuum equations will be via the Finite Element Method. The methods of completion of these objectives are outlined in the following chapter.

3.2 Methods

3.2.1 Parallel Plate Rheometry

A Rheometrics RMS 605 constant strain rheometer interfaced to a Pentium P60 PC was used for dynamic measurements. A schematic of the parallel plate geometry is shown in Figure 3.1. During dynamic testing, the top plate was driven

by the servo motor in an oscillatory fashion with a sine wave of known frequency ω such that the shear strain as a function of time was given by:

$$\gamma(t) = \gamma_o \sin(\omega t), \tag{3.1}$$

where γ_o is the strain amplitude. If the sample was a perfect Hookean solid described previously in Equation 2.6, the resulting stress would be *in-phase* with the driving sine waveform: $\tau = G\gamma_o \sin(\omega t)$. If the sample was a perfect linear dashpot (a piston moving in a cylinder with Newtonian fluid), the stress, $\tau = \eta\dot{\gamma}$, would be 90° *out-of-phase* with the driving waveform. Therefore, the stress for the linear dashpot, would be the time derivative of the driving sine waveform.

$$\tau = \eta\omega\gamma_o \cos(\omega t) \tag{3.2}$$

Since viscoelastic materials exhibit both solid- and liquid-like behavior, especially when modified with filler particles, the sample contained between the plates exhibits both in-phase and out-of-phase components of stress. A mechanical representation of this is the linear combination of a Hookean spring and a linear dashpot known as a Maxwell element shown in Figure 3.2. The variable δ is known as the phase angle, or the angle by which the out-of-phase response lags the in-phase response.

$$\tau = A_o(\omega)\sin(\omega t + \delta) \tag{3.3}$$

$$\tau = A_o(\omega)(\sin(\omega t)\cos(\delta) + \sin(\delta)\cos(\omega t)). \tag{3.4}$$

Using trigonometric identities, the stress can be decomposed as shown in Equation 3.4. The storage modulus G', or solid-like behavior is based on the in-phase component of the stress response: $G' = A_o(\omega)\cos(\delta)$. Analogously, the loss modulus G'' or liquid-like behavior, is based on the out-of-phase component of stress response: $G'' = A_o(\omega)\sin(\delta)$.

$$\tau = G'(\omega)\sin(\omega t) + G''(\omega)\cos(\omega t) \tag{3.5}$$

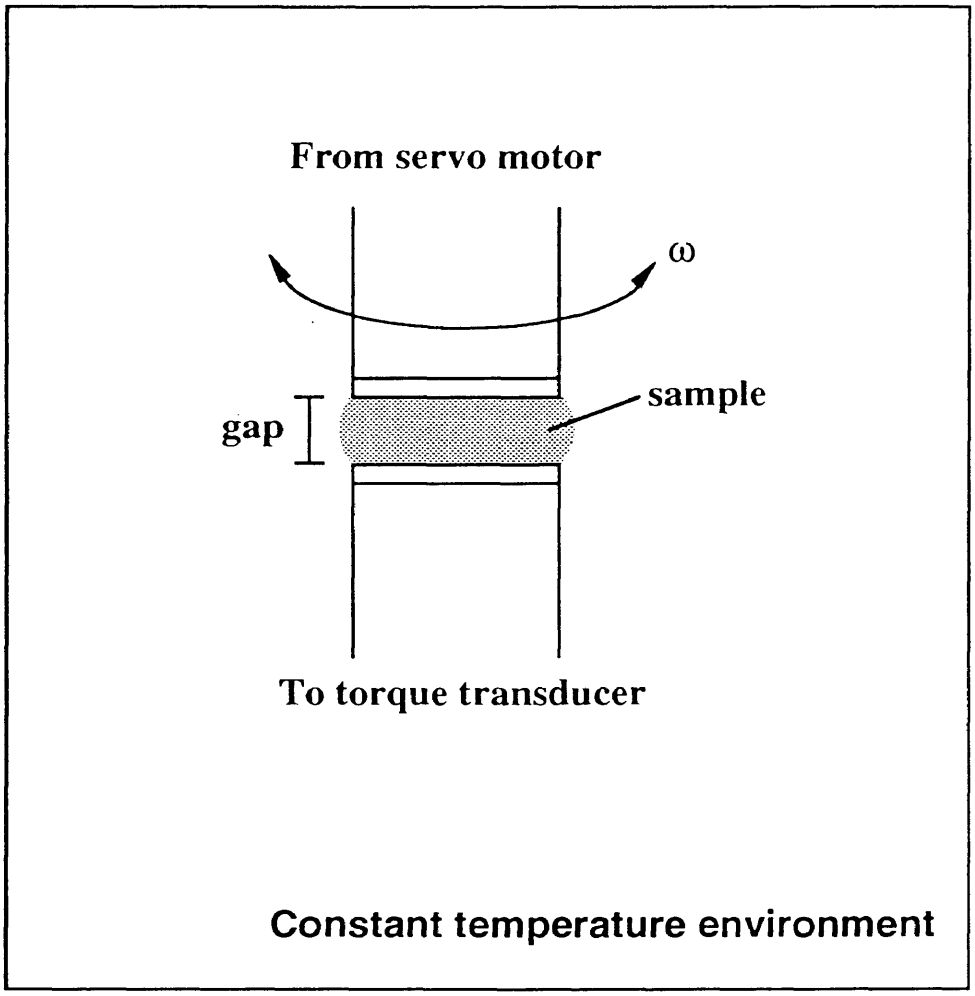

Figure 3.1: Diagram of parallel plate rheometer.

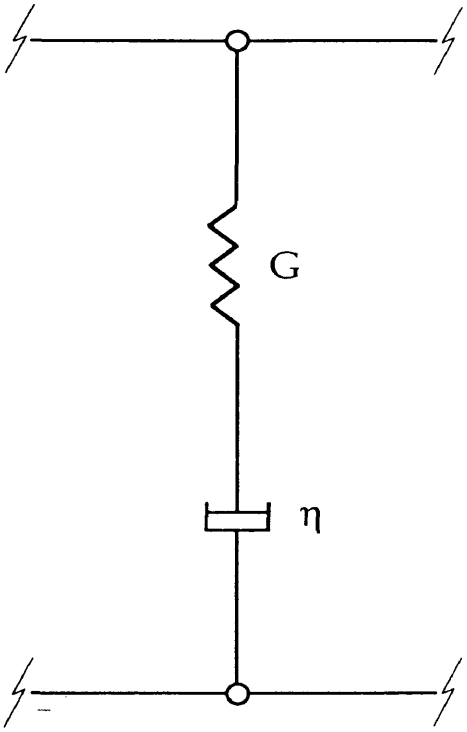

Figure 3.2: Schematic diagram of Maxwell element.

The complex viscosity η^*, a measure of the dynamic viscosity of the melt, is then calculated from Equation 3.6.

$$\eta^* = \sqrt{\left(\frac{G'}{\omega}\right)^2 + \left(\frac{G''}{\omega}\right)^2} \tag{3.6}$$

Generally, for homopolymer melts the complex viscosity is numerically equal to the steady-state shear viscosity.

3.2.2 Rheometer Configuration

The geometry for dynamic testing consisted of parallel plates 25 millimeters in diameter held at a separation of 1.6–2.0 millimeters. Rheometer control and data collection were controlled by RHIOS, a PC based software package produced by Rheometrics. RHECALC, a data calculation package produced by Rheometrics was used to convert strain, frequency and torque values from the rheometer to moduli used in the analysis based on the equations listed above.

Temperature control of the forced-air oven ranged within $\pm 1.0°C$ of the set point. Prior to experimentation, the rheometer plates were brought to the desired temperature and the plate spacing zeroed. Samples were then placed in the rheometer and allowed to anneal as plate separation was adjusted. Once the desired separation was achieved, the oven was opened and the excess material was trimmed. Samples were then allowed to thermally equilibrate for up to ten minutes. Prior to conducting frequency sweep tests, a series of strain sweeps were conducted at various frequencies, processing temperatures, and weight loadings of waste material in order to determine the limits of linear viscoelastic response.

The linear viscoelastic region can be defined as that in which the deformation is sufficiently mild so that the molecules of a polymeric material are minimally disturbed from their equilibrium configuration and entanglement state (Dealy 1990).

In practice this is observed as the ratio of overall stress to overall strain, the overall modulus $G(t)$ as a function only of time (or frequency) and temperature and not of stress or strain magnitude. Experimentally, this is denoted by the invariant region of a storage modulus (G') versus strain (in %) plot at a given frequency.

The Hookean spring responds instantaneously to an applied stress (τ) to reach an equilibrium strain (γ), according to Equation 2.6. Since G is a constant, $G(t) = G$. The Newtonian dashpot responds to an applied stress through Equation 3.7,

$$\tau = \frac{\eta}{t}\gamma. \tag{3.7}$$

The modulus G is then shown to be only time dependent: $G(t) \equiv \tau/\gamma = \eta/t = G(t\text{only})$. Therefore, both the Hookean spring and the Newtonian dashpot are linear. Furthermore, any combination of linear elements must be linear. If the filled polymer system is to be considered linear, it can be mechanistically described through a series of Maxwell elements.

Frequency sweeps at constant temperatures of 145, 165, and 185°C were conducted in both the "forward" (increasing frequency) and "reverse" (decreasing frequency) directions. The forward sweeps were run from 0.5 to 500 sec^{-1}; the reverse runs from 300 to 0.3 sec^{-1}. Each frequency sweep test consisted of a sequence of four consecutive test runs with a variable time delay of 0 to 15 minutes between sequence runs.

3.2.3 Computational Fluid Dynamics Modelling

The rheology results were implemented in a FEM analysis for flow modelling characterization and analysis and were used to parameterize the Power Law fluid non-Newtonian constitutive equation. FIDAP was then used to numerically solve

the equations of motion and energy for the non-isothermal flow field present in the die (exit) region.

The viscous response measured by the rheometer can be incorporated into FIDAP through the generalized Power Law model for a non-Newtonian fluid. The form of the model for the viscosity is as follows where $D^2 = \frac{1}{2} d_{ij} d_{ij}$, and T is temperature.

$$\eta = \begin{cases} \eta_o K \exp(A_1 T) D_o^{n-1} & D < D_o \\ \eta_o K \exp(A_1 T) D^{n-1} & D \geq D_o \end{cases} \tag{3.8}$$

The parameter n is the Power Law Index characteristic of the material; $(n-1)$ determines the shear thinning behavior. D is the scalar invariant of the rate of deformation tensor; D_o is the constant shear rate cutoff which gives the generalized model a shear rate-invariant but temperature-dependent zero shear viscosity.

FIDAP models were generated and used to estimate the die region conditions of the Berstorff twin screw extruder at RFETS. Quadratic elements were used in the finite element mesh. Material properties including mixture density, specific heat and thermal conductivity were calculated as weighted averages from the two components. The thermal boundary conditions were taken from actual extruder practice runs. The inlet velocity profile was modelled as a "blunted" parabola at known flowrates, fit to an analytical solution of the Power Law fluid. The governing differential equations solved during numerical simulation are listed in Table 3.1.

Equations of Motion:

$$\begin{aligned} \textit{r-component: } \rho\left(v_r\frac{\partial v_r}{\partial r}+v_z\frac{\partial v_r}{\partial z}\right) &= -\frac{\partial p}{\partial r}+\left(\frac{1}{r}\frac{\partial}{\partial r}\left(r\tau_{rr}\right)+\frac{\partial \tau_{rz}}{\partial z}\right) \\ \textit{z-component: } \rho\left(v_r\frac{\partial v_z}{\partial r}+v_z\frac{\partial v_z}{\partial z}\right) &= -\frac{\partial p}{\partial z}+\left(\frac{1}{r}\frac{\partial}{\partial r}\left(r\tau_{rz}\right)+\frac{\partial \tau_{zz}}{\partial z}\right) \end{aligned}$$

$$\textit{Shear Rate tensor: } \boldsymbol{\Delta}=\begin{bmatrix} 2\partial v_r/\partial r & 0 & (\partial v_r/\partial z+\partial v_z/\partial r) \\ 0 & 2v_r/r & 0 \\ (\partial v_z/\partial r+\partial v_r/\partial z) & 0 & 2\partial v_z/\partial z \end{bmatrix}$$

$$\begin{aligned} \textit{Constitutive Relationship:} \quad \tau_{ij} &= \eta(\boldsymbol{\Delta})\Delta_{ij}, \\ \tau_{rr} &= 2\eta(\boldsymbol{\Delta})\partial v_r/\partial r, \\ \tau_{rz} &= \eta(\boldsymbol{\Delta})\left(\partial v_z/\partial r+\partial v_r/\partial z\right) \\ \textit{Power Law Model:} \quad \eta(\boldsymbol{\Delta}) &= K\left(\frac{1}{2}II_\Delta\right)^{\frac{n-1}{2}} \\ II_\Delta &= \frac{1}{2}[(tr\boldsymbol{\Delta})^2-tr(\boldsymbol{\Delta}^2)] \end{aligned}$$

$$\eta(\boldsymbol{\Delta})=K\left[2\frac{v_r}{r}\left(\frac{\partial v_r}{\partial r}+\frac{\partial v_z}{\partial z}\right)+2\frac{\partial v_r}{\partial r}\frac{\partial v_z}{\partial z}-\frac{1}{2}\left(\frac{\partial v_r}{\partial z}+\frac{\partial v_z}{\partial r}\right)^2\right]^{\frac{n-1}{2}}$$

Equation of Energy:

$$\begin{aligned} \rho C_v\frac{DT}{Dt} &= -(\nabla:\mathbf{q})+(\tau:\nabla\mathbf{v}) \\ (\tau:\nabla\mathbf{v}) &= \tau_{rr}\left(\frac{\partial v_r}{\partial z}\right)+\tau_{rz}\left(\frac{\partial v_z}{\partial r}+\frac{\partial v_r}{\partial z}\right) \\ \mathbf{q} &= -kA\left(\nabla T\right) \\ \rho C_v\left(v_r\frac{\partial T}{\partial r}+v_z\frac{\partial T}{\partial z}\right) &= kA\left(\frac{1}{r}\frac{\partial}{\partial r}\left(r\frac{\partial T}{\partial r}\right)+\frac{\partial^2 T}{\partial z^2}\right) \\ &+ \eta\left(\boldsymbol{\Delta}\right)\left[2\left(\frac{\partial v_r}{\partial r}\right)^2+\left(\frac{\partial v_z}{\partial r}+\frac{\partial v_r}{\partial z}\right)^2+2\left(\frac{\partial v_z}{\partial z}\right)^2\right] \end{aligned}$$

Table 3.1: Governing partial differential equations for axi-symmetric geometry.

3.3 Materials

The materials for this experimental study were supplied by the RFETS. The waste was a surrogate (non-radioactive) composed of various Group I and Group II metal nitrate salts. This filler had a spray dried, hollow sphere morphology with an average particle diameter of 28 μm; there was little polydispersity in the sample. For filler characterization, see Appendix B. The bulk density of the salt filler was approximately 0.3 g/cm^3. Low density polyethylene supplied under the market name "Chevron 1409 LDPE" was used as the carrier phase in this study. The material was rated with a melt index (MI) of 50 g/10 min and a density of 0.924 g/cm^3.

Samples used for rheological characterization were generated through filled system extrusion at known weight percentages of waste salt filler. The extruder, a Berstorff 25mm co-rotating, self-wiping, intermeshing twin-screw extruder, was equipped with loss-in-weight feeders for accurate sample preparation. Samples were produced with 0 (neat), 12.5, 25, 37.5, and 50 weight percent (wt%) filler.

Rheology samples were then molded using a hydrostatic Carver press; approximately 2.0 grams of extrudate was placed in the mold and pressed at 220°C and 500 psi. These samples were dried in a vacuum oven (Precision Model) at 100°C overnight prior to rheological testing.

Chapter 4

RESULTS AND DISCUSSION

4.1 Rheological Characterization

4.1.1 Development of Experimental Protocol

Development of the filled system experimental rheological protocol consists of determining the limits of linear viscoelasticity of the samples as functions of filler weight loading and temperature as well as generation of homogeneous, reproducible samples prior to data collection.

Linear Viscoelasticity Limits

A typical strain sweep result for the filled system is shown in Figure 4.1. The limits of linear viscoelasticity are determined for each loading level and operating temperature over a series of oscillatory frequencies. As described in Section 3.2.2, the upper limit of viscoelasticity for the sample is taken to be the point at which the storage modulus deviates approximately 10% from its initial value at low strains.

The limits of linear viscoelastic behavior, i.e. maximum strain at a given frequency, for each filler loading and temperature are then used to tailor frequency sweep experiments. In these, the strain level is dynamically adjusted such that the material behaves in a linear manner across all tested frequencies.

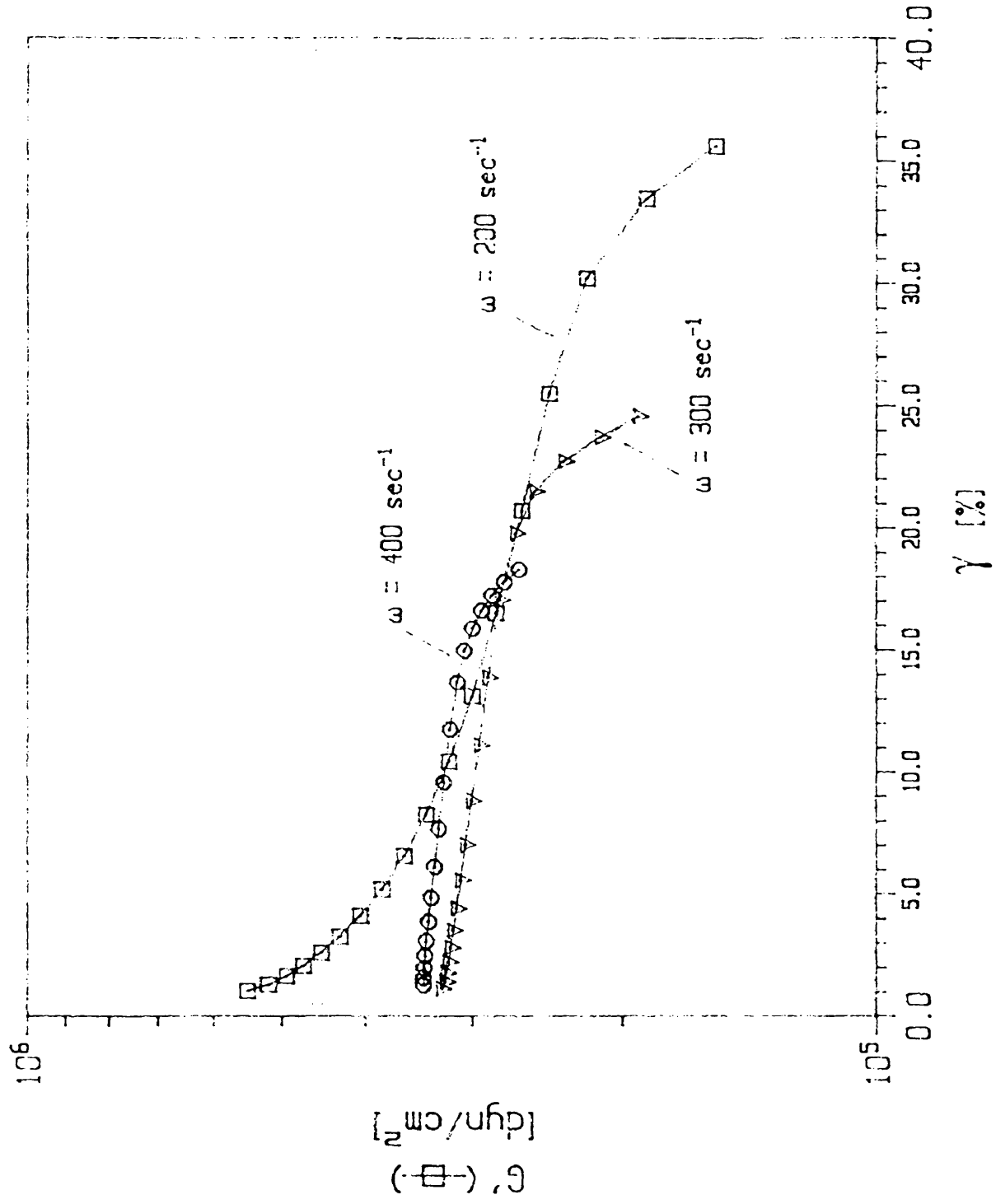

Figure 4.1: Strain sweep result for 37.5 wt% filled sample at 185°C.

Frequency Sweep Sequencing

Initial rheological results such as to those presented in Figure 4.2 were collected with the rheometer configured to complete a sequence of tests with no time delay between tests. As evidenced by the results, the material response is not uniform. Instead, the material's viscoelastic behavior is dependent on the number of deformation cycles. Only after a large number of sequenced runs do the flow curves begin to converge. In order to eliminate the effect of flow curve non-uniformity and banding, the sample was allowed to relax for as long as fifteen minutes between sequenced experiments. This time delay was added such that a sequence run was immediately followed by a *rest* period at the operating temperature. This proved to be a valuable procedure as the data in Figure 4.3 demonstrate. Even with highly filled samples at lower temperatures, originally believed to result in a highly non-uniform "band" of viscosities by Cheng (1984), the flow curves superimpose almost immediately after the first sequence run.

The sequence run #1 of 4 in Figure 4.3 has an anomalous response that has no correlation to the final viscosity profile in the low frequency region. This first run is termed "as-molded". Mills (1971) suggested that the molded-in packing structure of the filler particles causes an initial reinforcement of the Youngs modulus (Y, see Equation 2.10 on page 18) of the melt. While no determination of actual molded-in structure has been made, the reproducibility of the results demonstrates that this initial structure can be eliminated from the samples.

Further analysis of the filled system rheological response reveals behavior indicative of "molded-in" flocculated structure. Figure 4.4 shows complex viscosity (η^*) and calculated stress (τ_s) versus frequency (ω) at T=145°C and 37.5 wt% filler. The data for curve (A) represent a sample tested without prior deformation or dynamic strain level adjustment. Following curve (A2), a maximum stress level

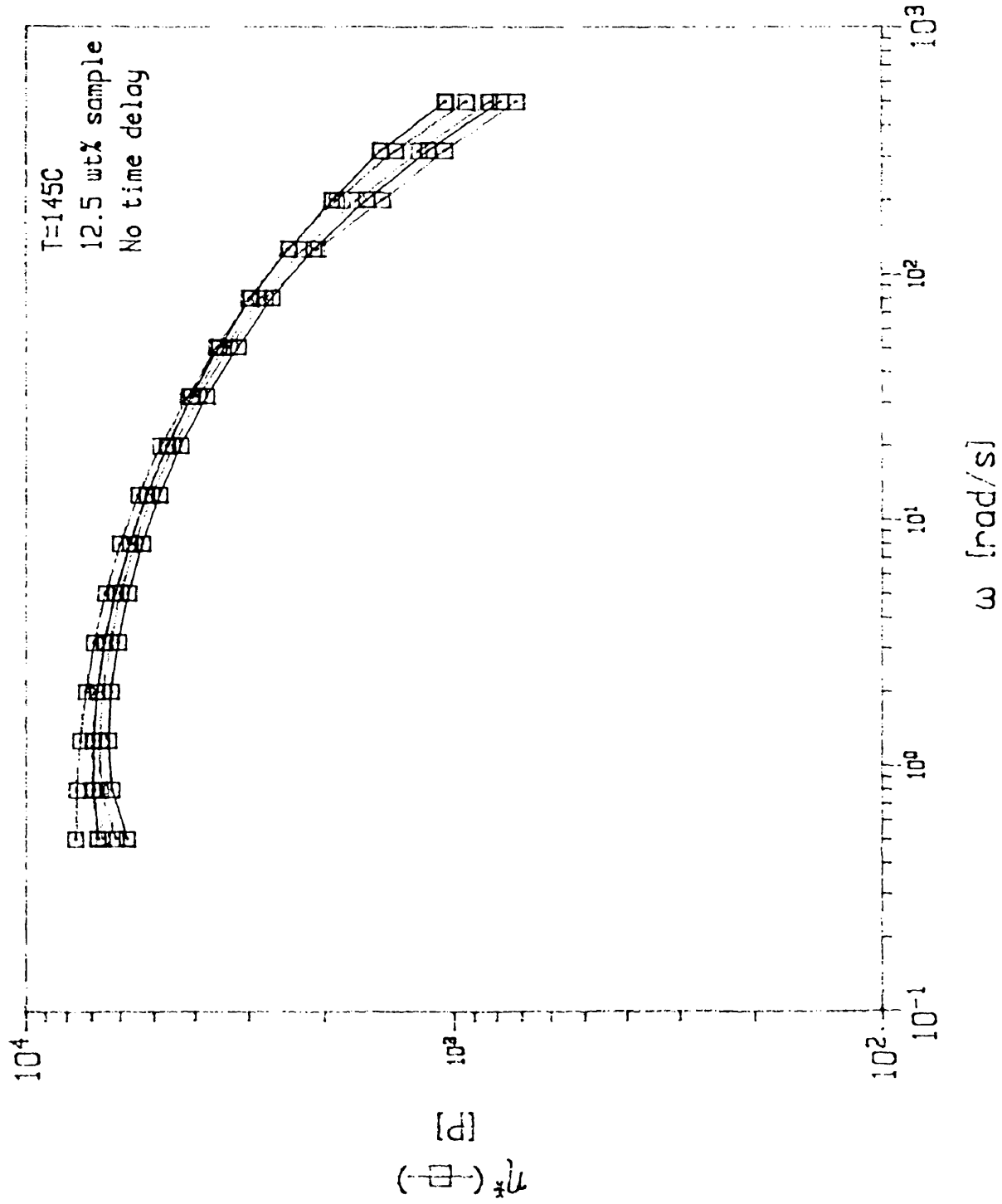

Figure 4.2: Complex viscosity (η^*) versus shear rate (ω): the banding is associated with no time delay.

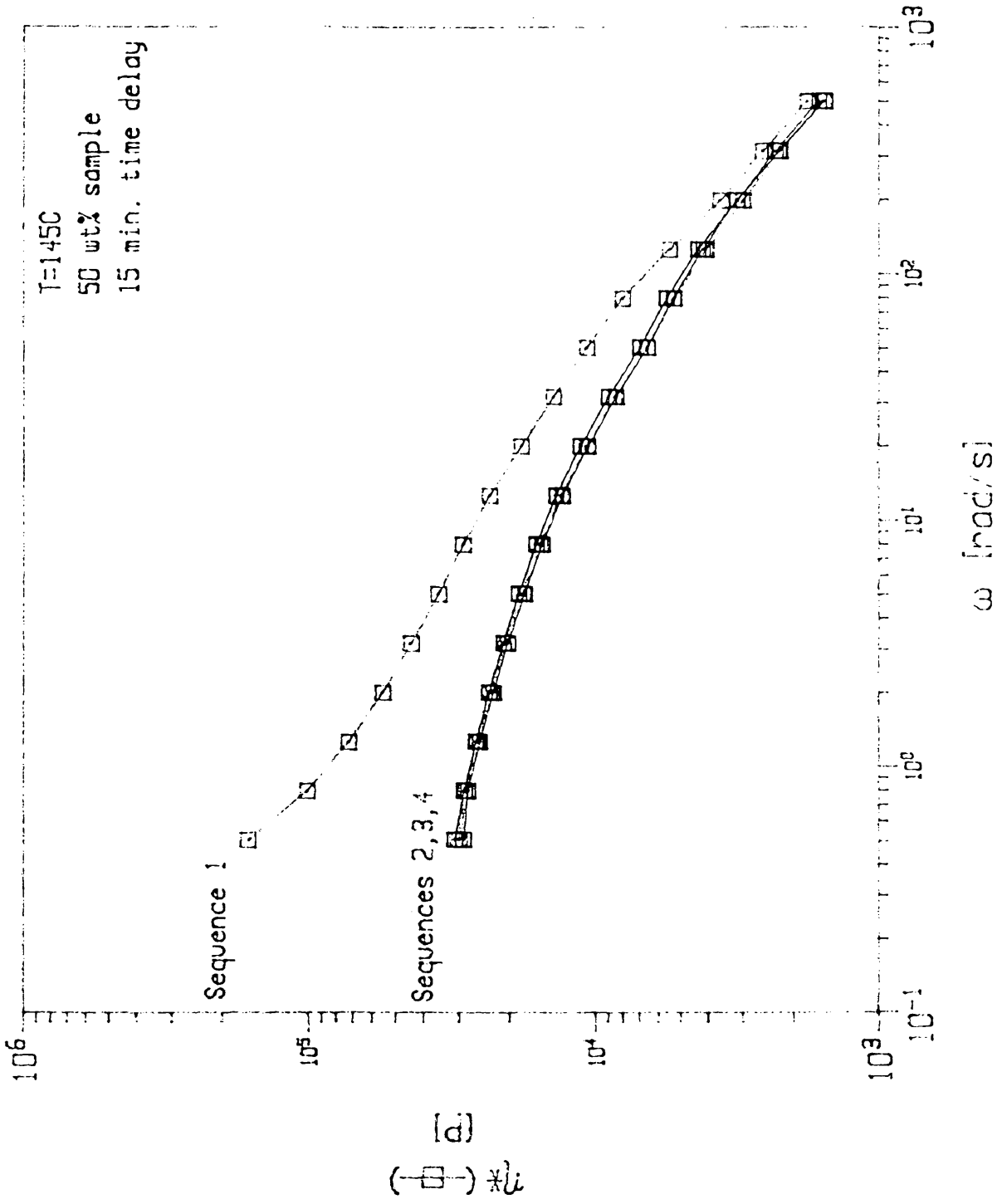

Figure 4.3: Complex viscosity (η^*) versus shear rate (ω): low temperature, highly loaded sample reproducibility provides support for incorporating time delay.

is reached at approximately 10 sec^{-1} at which point the stress quickly becomes nonlinear and the companion viscosity profile (A1) decreases rapidly. This is consistent with yielding behavior of flocculated suspensions: the internal structure cannot support the shear stress levels and fails, releasing energy and decreasing the level of supported stress.

In contrast, curve (B) (shown here for a pre-sheared sample under dynamic strain level adjustment), denotes linear behavior over the entire frequency range: the pre-sheared sample responds with a monotonically increasing stress level with increasing shear rate. The pre-shearing process involves a sequence of four frequency sweeps over the desired frequency range; the data reported is generated from the fourth frequency sweep. Typically a time delay is included between sequence runs to allow ample recovery time for the dispersed structure. It will be demonstrated that the pre-shearing procedure generates a homogeneous sample for rheological testing consistent with the theory proposed by Han and discussed in Section 2.3.2.3.

The data in Figures 4.5, 4.6, and 4.7 represent dynamic frequency sweep results for 25, 37.5, and 50 wt% samples, respectively. While it is evident that each wt% sample coincides with itself, the different loading level samples are slightly less comparable at the same temperature, as shown in Figure 4.8. Based on Han's criteria for homogeneous morphological characteristics of multiphase polymer blends, further analysis such as time-temperature superposition and relative viscosity calculations can be completed.

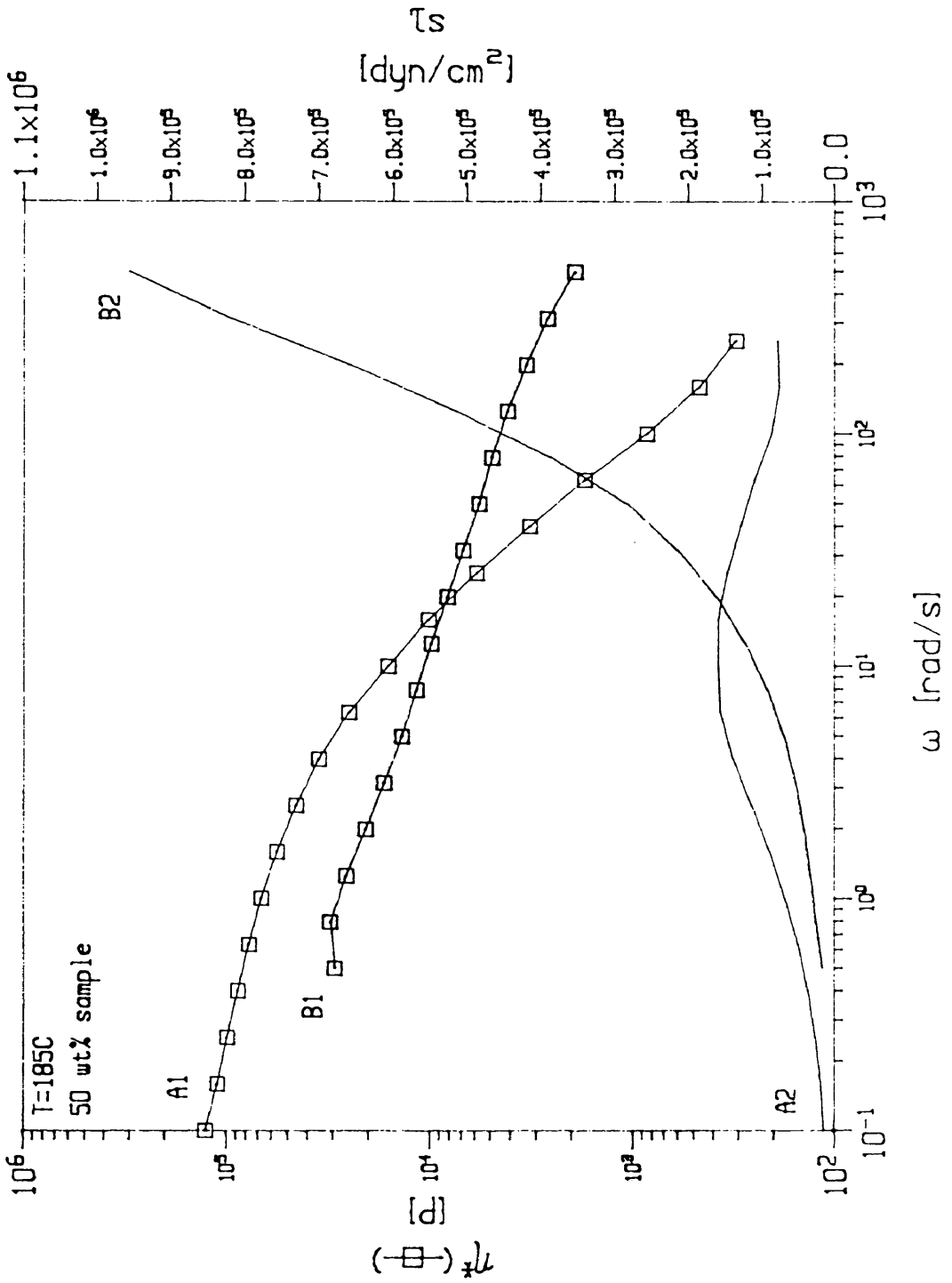

Figure 4.4: Complex viscosity (η^*) and shear stress (τ_s) versus shear rate (ω). This plot provides an example of the linear viscoelastic region in the polymer sample.

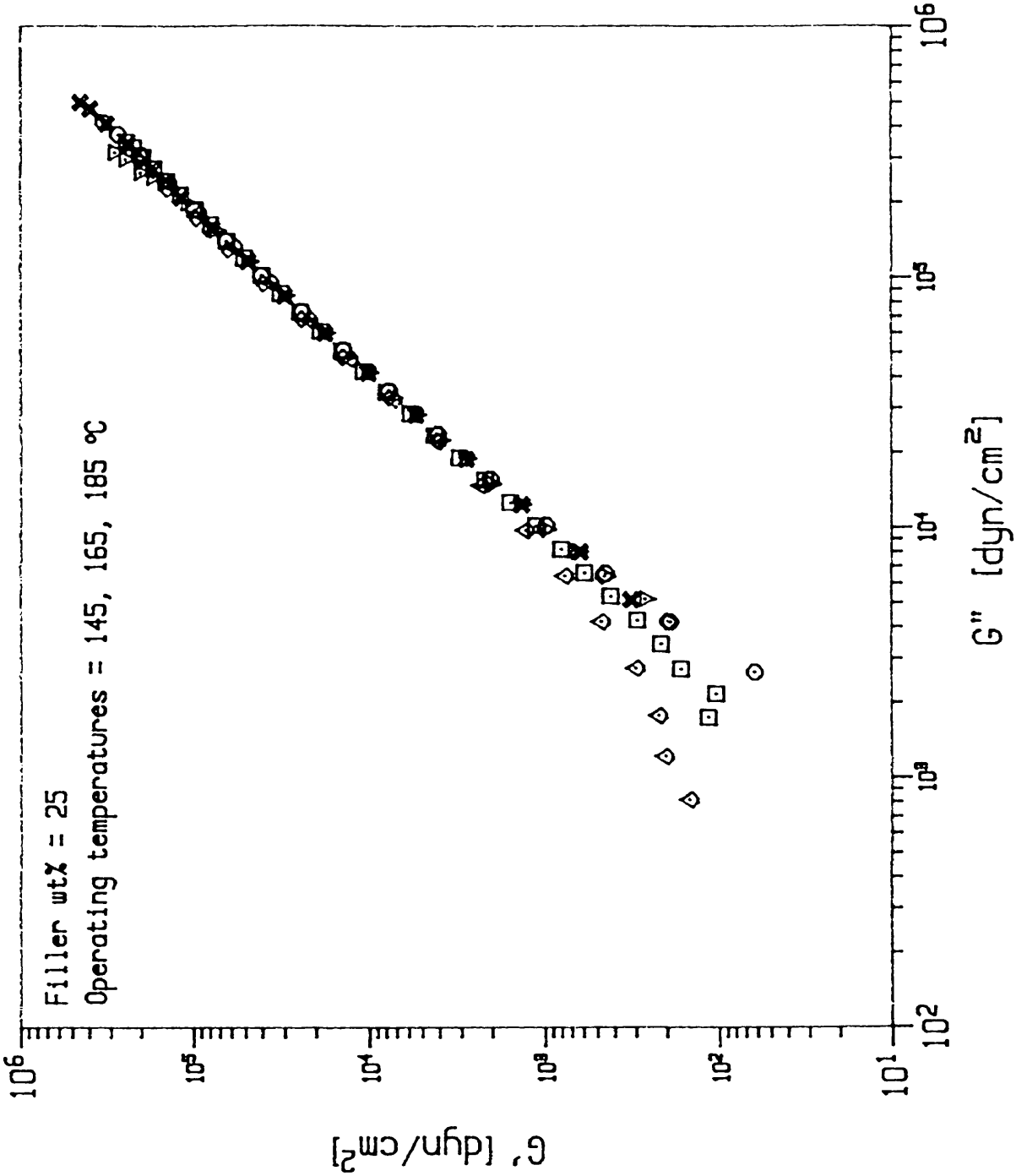

Figure 4.5: Plot of $\log G'$ versus $\log G''$ for 25 wt% filler. Homogeneous sample exists at all temperatures.

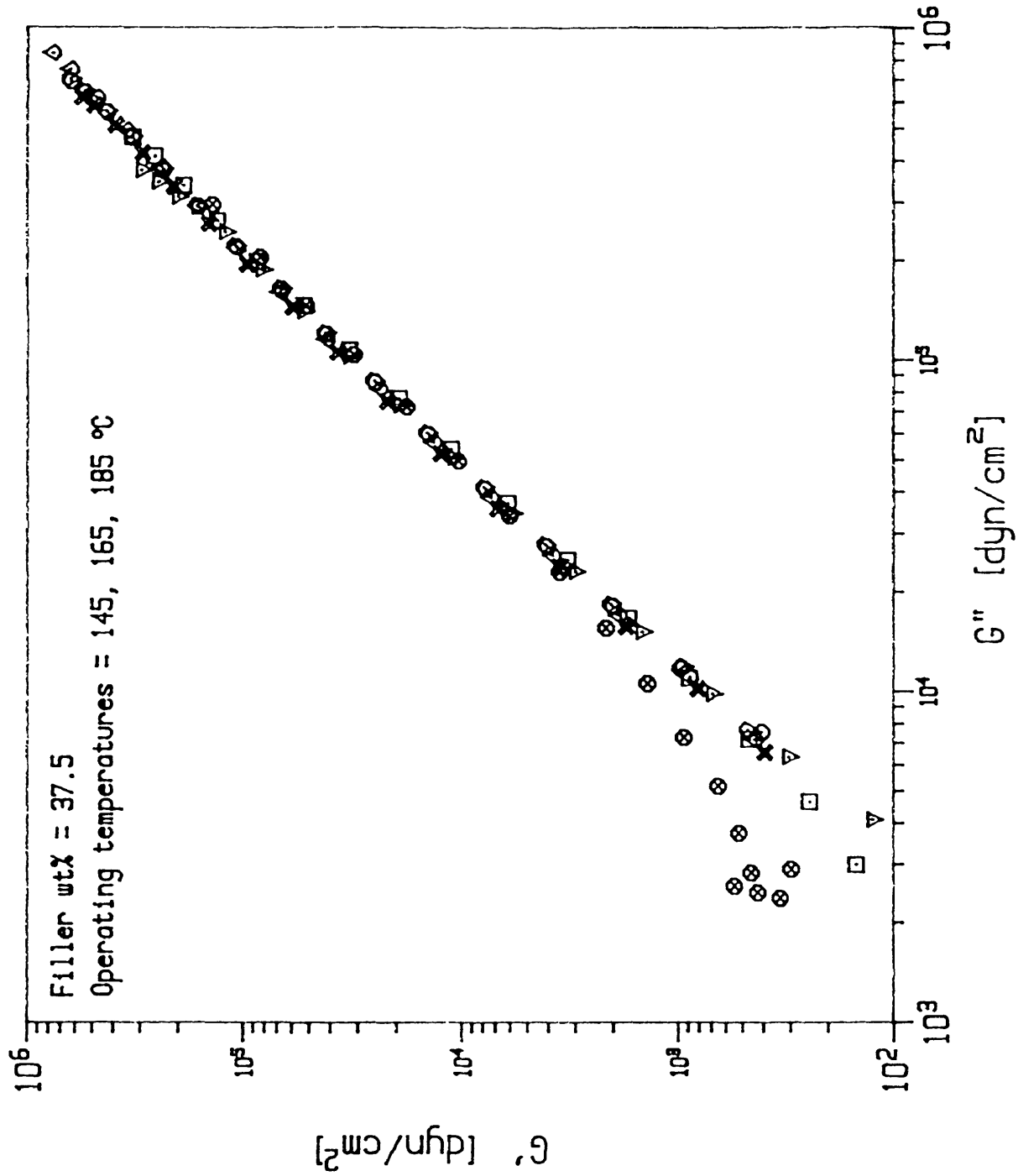

Figure 4.6: Plot of $\log G'$ versus $\log G''$ for 37.5 wt% filler. Homogeneous sample exists at all temperatures.

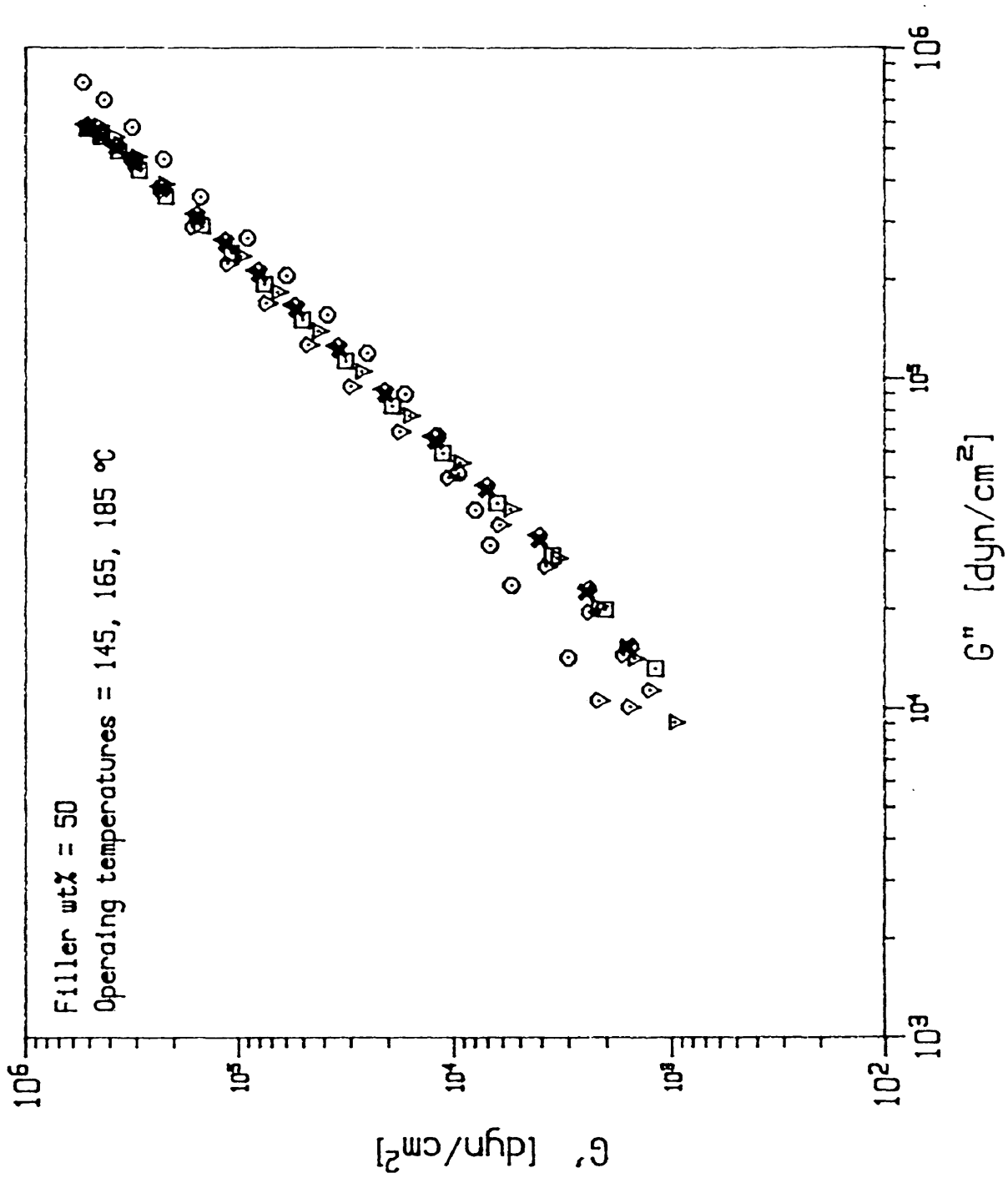

Figure 4.7: Plot of $\log G'$ versus $\log G''$ for 50 wt% filler. Homogeneous sample exists at all temperatures.

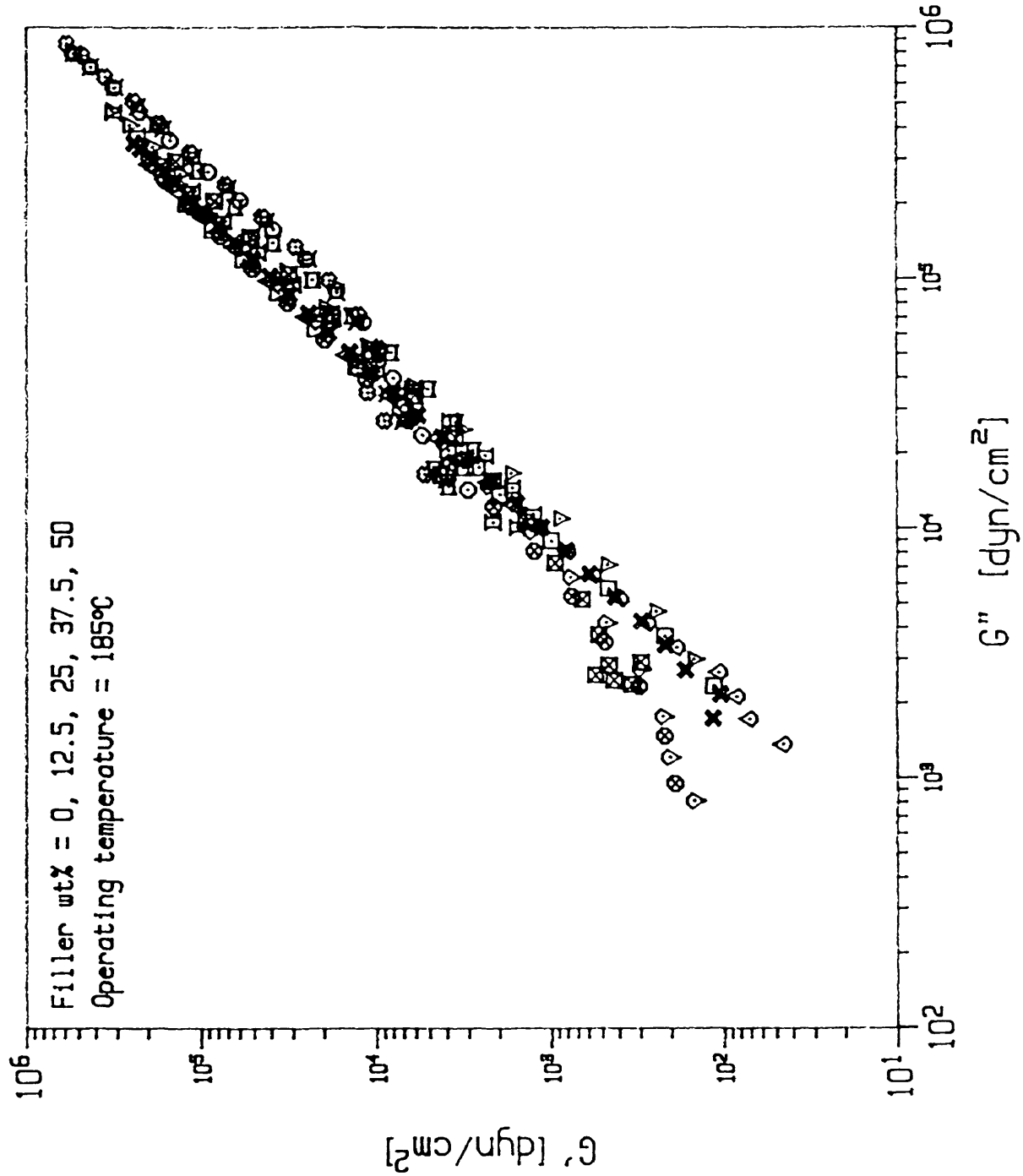

Figure 4.8: Plot of $\log G'$ versus $\log G''$ for all filler loading levels at 185°C. It is believed samples exist in same homogeneous state at this operating temperature.

4.1.2 Filler Density, Maximum Packing Fraction, and Intrinsic Viscosity

In order to compare the theoretical expressions introduced in Section 2.2 with the experimental data for the filled system, the filler dependent term known as the maximum packing fraction (ϕ_m) needs to be known for the spray dried salt filler. The method of Wildemuth and Williams (1984) will be used for the explicit determination of ϕ_m and $[\eta]$.

Prior to calculation of ϕ_m, the experimental data (η_r versus filler weight fraction) must be reevaluated to attain proper filler volume fraction (ϕ) values. Calculation of filler volume fraction follows Equation 4.1:

$$\phi = \frac{V_{filler}}{V_{filler} + V_{polymer}} = \frac{m_{filler}(\frac{\rho_{polymer}}{\rho_{filler}})}{m_{filler}(\frac{\rho_{polymer}}{\rho_{filler}}) + m_{polymer}} \tag{4.1}$$

where ϕ is the volume fraction of filler, and $m_{filler}, m_{polymer}, \rho_{filler}, \rho_{polymer}$ are mass of filler in the sample, mass of polymer in the sample, apparent density of filler, and polymer density, respectively. However, the actual filler density is unknown, as SEM results show crushed spheres in the post-extruded sample (see Figure B.1). Hence, filler densities are assumed to range from 0.3 g/cm^3 (powder bulk density) to 3.0 g/cm^3 (salt specific density). Values for ϕ are calculated for each filler weight loading level based on the series of filler densities. The technique employed to determine ϕ_m is also used here because of the a priori knowledge that $[\eta] \approx 2.5$ in the theoretical limit (Wildemuth 1984). It is also believed that (ϕ_m) will approach the theoretical limit for close packed spheres as $[\eta] \rightarrow 2.5$. This does not account for polydispersity of the filler, which will tend to increase ϕ_m for a fixed volume fraction. Results for ϕ_m and $[\eta]$ are shown in Table 4.1. The figures used to determine ϕ_m and $[\eta]$ can be found in Appendix A.

Examination of the data presented indicates significant trends. First, it is seen that ϕ_m generally increases with increasing stress. This is expected due to the

Salt Density (gm/cm^3)	Stress ($dyne/cm^2$)	ϕ_m	$[\eta]$
1.25	1.60E+04	0.460±0.001	1.051±7.88E-03
	1.00E+05	0.524±0.002	1.174±9.50E-03
	2.00E+05	0.545±0.002	1.435±0.011
	3.00E+05	0.736±0.009	1.870±0.019
1.50	1.60E+04	0.417±0.001	1.243±0.010
	1.00E+05	0.489±0.002	1.452±0.012
	2.00E+05	0.500±0.002	1.730±0.014
	3.00E+05	0.709±0.010	2.255±0.024
1.75	1.60E+04	0.381±0.001	1.434±0.012
	1.00E+05	0.461±0.002	1.745±0.015
	2.00E+05	0.462±0.002	2.000±0.017
	3.00E+05	0.684±0.011	2.640±0.030
2.00	1.60E+04	0.350±0.001	1.623±0.015
	1.00E+05	0.439±0.002	2.056±0.018
	2.00E+05	0.429±0.003	2.267±0.021
	3.00E+05	0.661±0.013	3.025±0.036
2.25	1.60E+04	0.325±0.001	1.817±0.018
	1.00E+05	0.421±0.002	2.384±0.022
	2.00E+05	0.400±0.003	2.531±0.025
	3.00E+05	0.639±0.014	3.409±0.043

Table 4.1: Filler maximum packing fraction (ϕ_m) and intrinsic viscosity $[\eta]$ for varying filler densities. Method from Wildemuth and Williams (1984).

Filler Weight Fraction	ϕ
0.0000	0.0000
0.1250	0.0701
0.2500	0.1450
0.3750	0.2406
0.5000	0.3455

Table 4.2: Filler volume fraction ϕ corresponding to filler weight percent in samples prepared through extrusion. Data compiled at $\rho_{filler} = 1.75$ g/cm^3.

incomplete breakup of flocs in the suspension under lower stress levels. Second, $[\eta]$ also increases with increasing stress. This response is not as predicted by WIldemuth and Williams. Yet, in the high stress limit, $[\eta] \rightarrow 2.5$ *and* $\phi_m \rightarrow 0.68$ for a filler density of 1.75 g/cm^3. For the conclusion of the discussion, a filler density of 1.75 g/cm^3 will be assumed. At a filler density of 1.75 g/cm^3, the analogous filler volume fraction for each weight loading is compiled in Table 4.2.

Upon closer examination of the data presented in Table 4.1, it is evident that a pseudo-plateau exists in which the filler structure can support the imposed stress without breakup. Initial shearing breaks the unstable structure, yet further shearing causes little structure breakup (τ=1.00 and 2.00E+05, ϕ_m=0.461$\pm$0.002 and 0.462$\pm$0.002, respectively). Once the stress can no longer be supported by the filler structure, further breakdown occurs, rendering the sample with a higher ϕ_m.

4.1.3 Stress and Thermally-Dependent Maximum Packing Fraction

Analysis of ϕ_m has shown a clear stress dependence such that $\phi_m = \phi_m(\tau)$. It can be argued that because the stress response in the polymer is a function of temperature, the maximum packing fraction must also be temperature dependent.

	Stress			
Temp	1.60E+04	1.00E+05	2.00E+05	3.00E+05
145	0.476±5.02E-03	0.530±7.11E-03	0.613±0.011	0.895±0.029
165	0.471±5.24E-03	0.546±8.75E-03	0.693±0.015	0.696±0.017
185	0.367±1.99E-03	0.431±3.13E-3	0.478±4.36E-03	
195	0.393±2.15E-03	0.421±3.42E-03	0.552±9.72E-03	

Table 4.3: Filler maximum packing fraction (ϕ_m) as a function of stress and temperature. Method from Wildemuth and Williams (1984).

Independent of a shearing environment, the salt-filled system exhibits thermal dependencies through differential thermal and thermogravimetric analysis (see Figures B.3 and B.4). The stress and thermal dependencies of ϕ_m can be decoupled by examining the data at single values of stress (or temperature) via the Wildemuth method. Data from this analysis is compiled in Table 4.3 and can be found in Appendix A beginning on page 122. Data was unable to be collected for samples at combinations of high stress and temperature.

Analysis shows the maximum packing fraction increases similarly with increasing stress, yet reaches a much higher value at 145°C than at 165 or 185°C. From this, it may be inferred that the network structure is more fragile at lower temperatures and is therefore broken up more easily while under strain. This level of packing efficiency is indicative of high polydispersity within the filler phase. For each stress, ϕ_m generally decreases with increasing temperature. This is believed due in part to increased particle attraction and network stability. Hence, ϕ_m can now be described such that $\phi_m = \phi_m(\tau, \textit{ and } \mathrm{T})$.

4.2 Relative Viscosity

As previously discussed in Section 2.2, determination of the viscosity enhancement through filler loading is conducted by relative viscosity comparisons. Typically, the filler loading is normalized to the specific filler maximum packing fraction. This is usually a single value characteristic of monodisperse spheres. In the surrogate salt-filled low density polyethylene system investigated, it has been shown that $\phi_m(\tau,\ \mathrm{T})$ is a complex function of both stress and temperature. This precludes the use of a single value for ϕ_m and requires the combination of $\phi_m(\tau,\ \mathrm{T})$ values.

4.2.1 Experimental Results

A plot of the relative viscosity (η_r) as a function of filler volume fraction normalized by the stress and thermally-dependent maximum packing fraction ($\phi_m(\tau,\ \mathrm{T})$ is shown in Figure 4.9. It is immediately apparent from the data in the figure that scatter exists within the data set, especially in the highly loaded samples. As expected, a band of viscosities dominate when the filler loading tends toward a maximum as depicted in Figure 4.10.

Upon examination of the data collected at $\phi = 0.3455$, some important thermal effects are revealed. Figure 4.11 shows the respective temperature and stress level configuration at which the measurement was made. At the highest stress level measured, 2.0E+05 dyne/cm^2, the relative viscosities at 185 and 195°C are approximately equal. The reduction in normalized volume fraction with increasing temperature is an uncharacteristic response of this system, indicating higher levels of complexity within the filler structure. At τ=1.0E+05 dyne/cm^2, the relative viscosity and normalized volume fraction values virtually coincide between 185 and

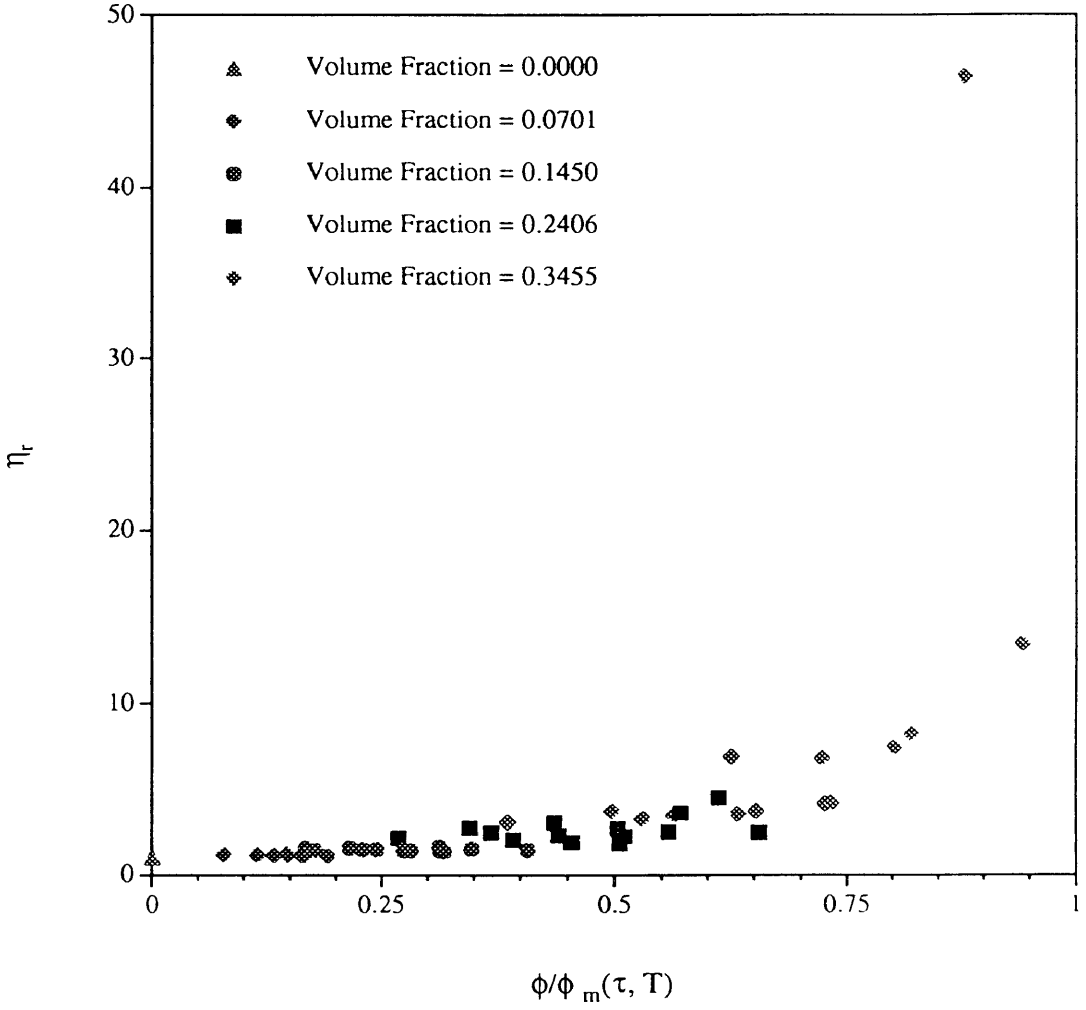

Figure 4.9: Relative viscosity (η_r) versus normalized filler volume fraction ($\phi/\phi_m(\tau,\ T)$).

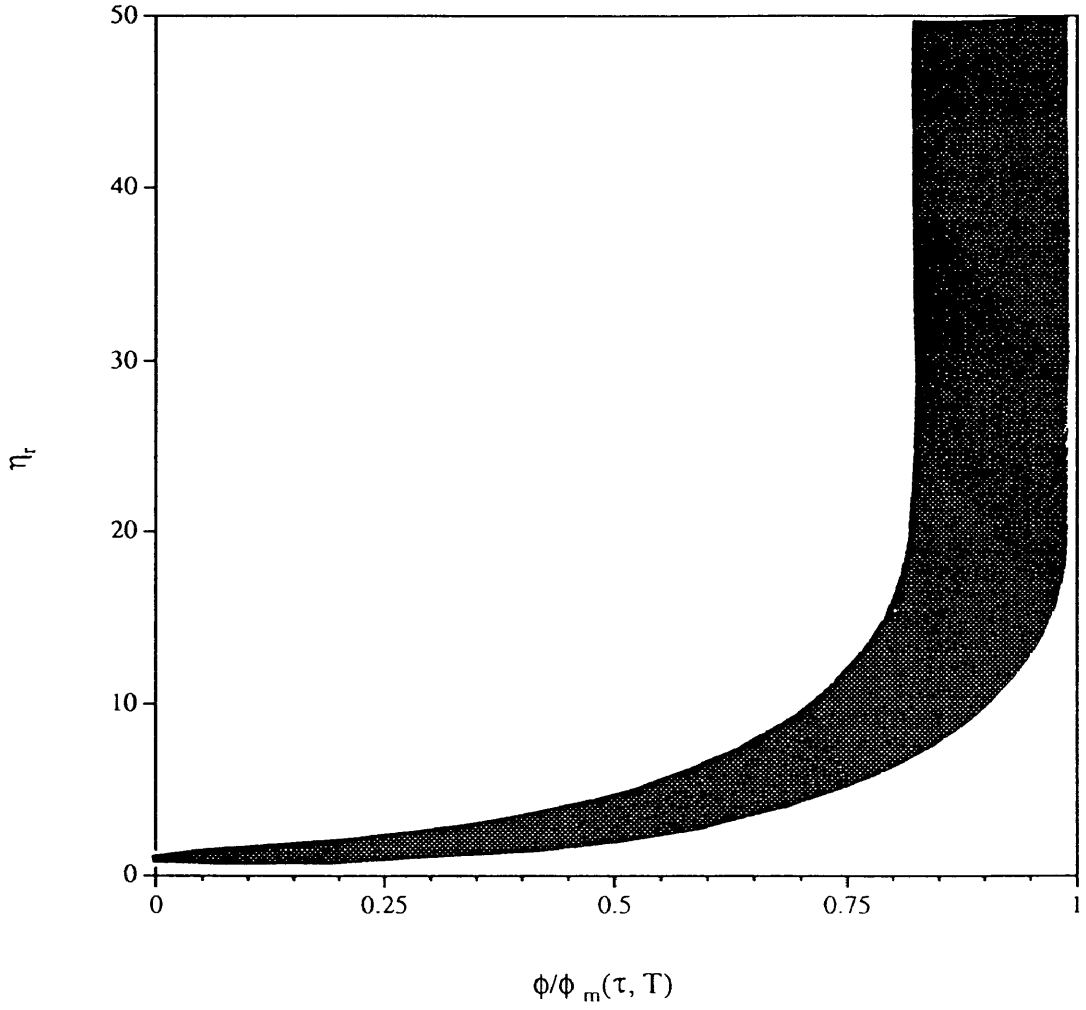

Figure 4.10: Relative viscosity (η_r) versus normalized filler volume fraction ($\phi/\phi_m(\tau,\ T)$). The shaded area outlines the band of possible viscosities.

195°C. Examination of the data collected at τ=1.6E+04 dyne/cm^2 does not elucidate a concise mechanism for the spread in the data. Possible reasons for this spread include polymer degradation accelerated by the catalytic action of the filler. Once the polymer has begun to crosslink, the basis for relative viscosity calculation is no longer valid. Another possibility is a filler chemical transition. The filler may undergo a surface chemistry transition and become highly attractive (or repulsive) for the polymer chains. In this instance, the filler may preferentially interact with the polymer, tending to form a lightly crosslinked structure.

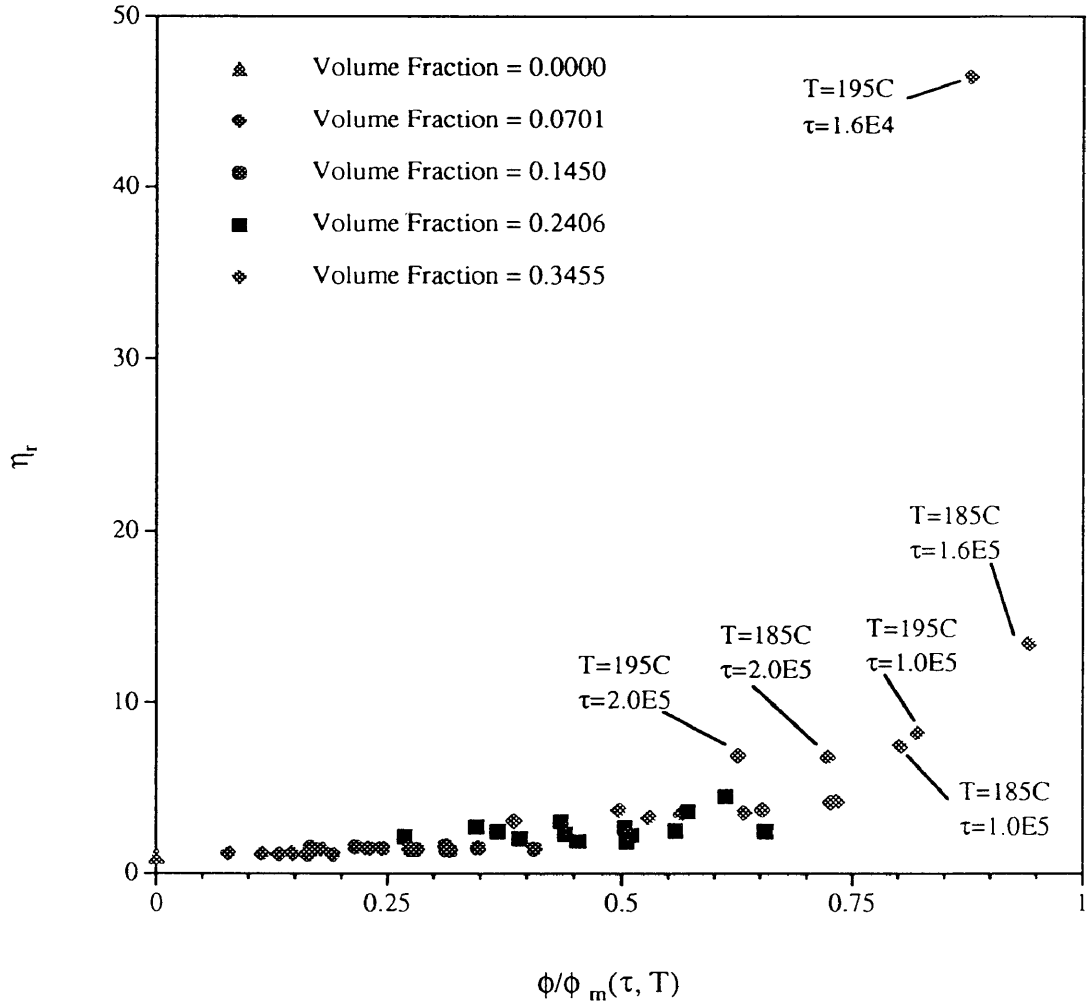

Figure 4.11: Relative viscosity (η_r) versus normalized filler volume fraction ($\phi/\phi_m(\tau, T)$). The labels designate the temperature and stress level configuration.

4.2.2 Comparison of Experimental Results and Theoretical Predictions

In Figure 4.12, the experimental data is compared to the theory proposed by the Frankel and Acrivos equation (Equation 2.3). The predicted response from the Maron-Pierce-Kitano equation (Equation 2.5) is shown in Figure 4.13.

It is evident from the comparison to both theories that insufficient data exists in the high loading level region. This is primarily due to the sample preparation technique; a filler loading level of 50% by weight limited the extrusion operation. It is believed that rheological testing of higher loading levels will complete the curve. Although the relative viscosity data exhibits somewhat characteristic curvature in the high loading regime, the data cannot definitively describe the relative viscosity functionality. The curve defined by Equation 2.3 in Figure 4.12 seems to depict a better function al fit than that of the Maron-Pierce-Kitano equation (Equation 2.5, Figure 4.13). This can be attributed to the complex filler behavior. Notice that few data points reside *above* either curve. The decreased relative viscosity values from those predicted possibly arises from the polydispersity of the samples. Also, the Frankel and Acrivos equation is a weaker function of normalized volume fraction [on the order of 1] whereas the Maron-Pierce-Kitano equation is a much stronger function of normalized volume fraction [on the order of $1/(\phi/\phi_m)$]. This can be interpreted as a reduction in the significance of filler inhomogeneities such as polydispersity and surface chemistry.

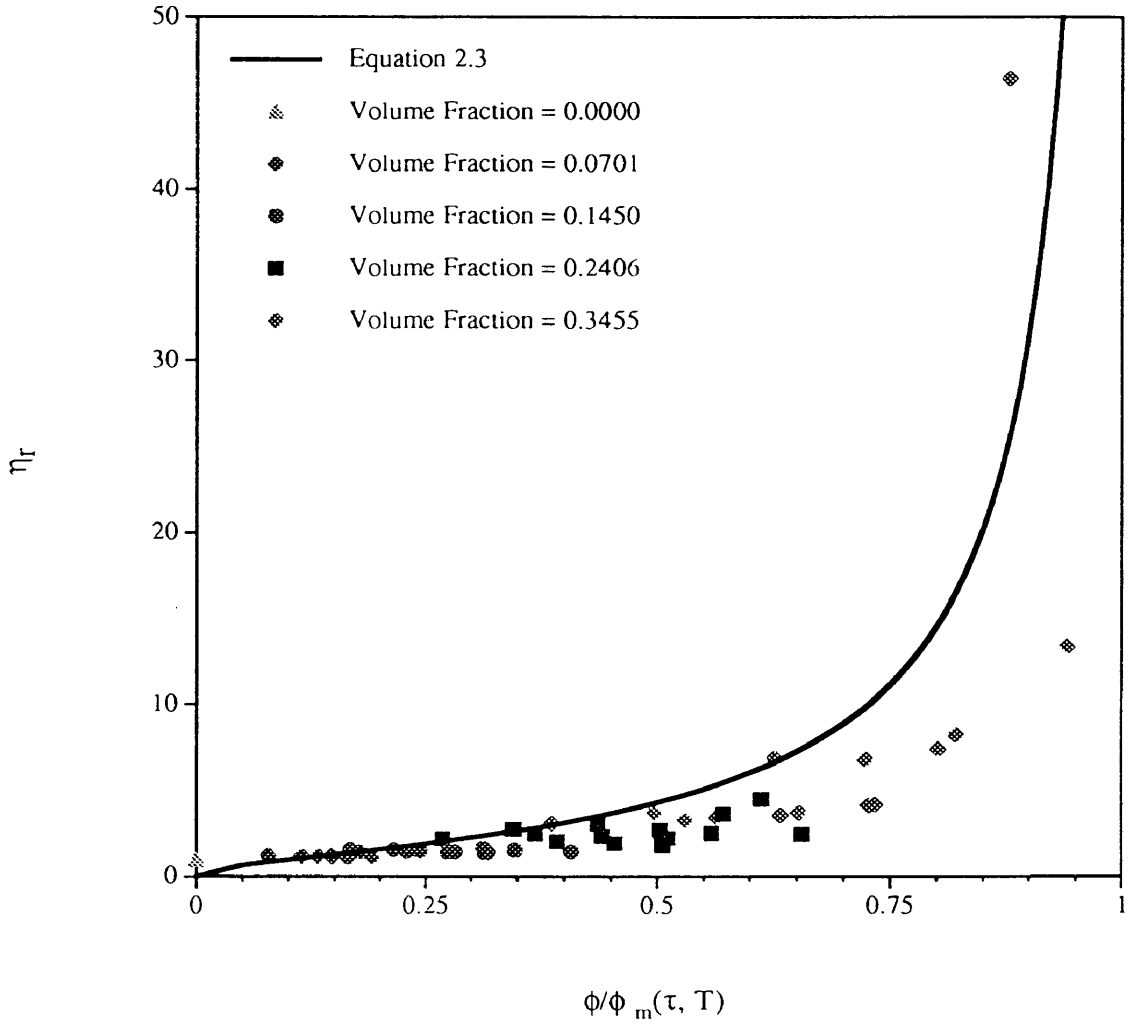

Figure 4.12: Relative viscosity (η_r) versus filler volume fraction (ϕ). Solid line generated form theoretical prediction given by Equation 2.3.

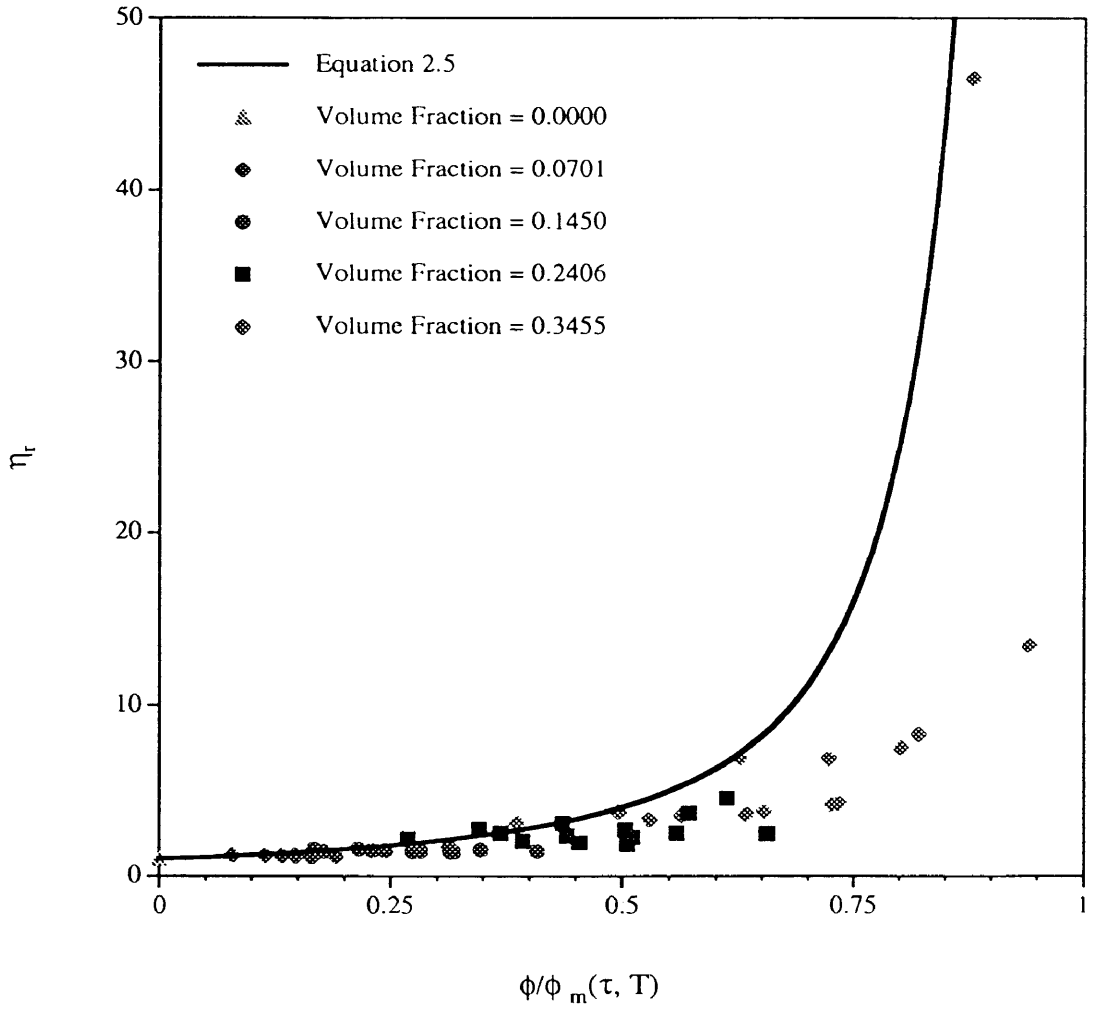

Figure 4.13: Relative viscosity (η_r) versus filler volume fraction (ϕ). Solid line generated form theoretical prediction given by Equation 2.5.

4.3 Application of Superposition Principles

4.3.1 Time-Temperature Superposition

The principle of time-temperature superposition (TTS) uses the scalable relaxation spectrum inherent to a viscoelastic material to relate a material property, such as viscosity, under separate conditions of deformation rate (time) and temperature. The Deborah number ($De = \lambda_c \omega$) relates the chain relaxation time λ_c to the time of deformation ω. A colder material has high λ_c; a large deformation rate corresponds to high ω values. Therefore based on the Deborah number, cooling the sample has the same effect as rapid deformation and vice versa.

The relationship of viscosity measurements under separate conditions of deformation rate and temperature is taken into account through a shift factor a_T:

$$a_T = \frac{t_T}{t_{T_o}} \text{ (for same response)}, \tag{4.2}$$

where t_T is the time required to reach a particular response at temperature T and t_{T_o} is the time required to reach the *same response* at the reference temperature T_o (Rosen 1993). The shift factor is then used to modify rheological data horizontally along the log time or ω axis, since $t_T = a_T t_{T_o}$. Rheological data may also be shifted vertically; this procedure is very similar to the horizontal shift procedure and will not be discussed here. The resulting curve is a master curve which extends the applicable range of rheological data at the reference temperature.

Using the reproducible flow curves resulting from the developed protocol, master curves are constructed according to the principle of time-temperature superposition at each loading level. Figure 4.14 shows that the master curves span almost four orders of magnitude in shear rate thus extending the data to realistic processing conditions. The scatter in the low and high shear rate ranges is associated with sample variability and possible structure effects. It is important to note

that while TTS is a viable method for extending the applicable range of viscosity data, the agreement with Han's (1993) premise suggested in Figure 4.8 enables the application of *time-particle* superposition.

4.3.2 Time-Particle Superposition

Time-particle superposition (TPS) uses the characteristic relaxation time of the polymer chains incorporating the influence of the filler particles to produce master curves of viscosity (η^*) versus frequency (ω). The horizontal and vertical shift factors are determined through analysis of flow curves at the same temperature and varying *loading levels*. The master curves are referenced to that of the neat sample. Similar referencing takes place in the TTS analysis where the curves are referenced to the highest temperature flow curve; the viscous response is lowest for both the higher temperature curves (in the case of TTS) and the neat rheograms (in the case of TPS). Nicodemo and Nicolais (1974) showed comparable results for a suspension of glass beads in a solution of polyisobutylene in decalin. A similar shifting procedure indicated that the system behavior at high shear rates was due to the influence of the filler on the flow properties of the polymer chains, in particular on relaxation time.

The TPS master curves calculated across all filler loading levels are shown in Figure 4.15 for 145, 165, and 185°C. Examination of the data shows what appears to be periodic spikes in the complex viscosity values. This is an artifact of the superposition algorithm. Since the polymer chain relaxation time is a well defined physical property, it is proposed that the filler has the effect of increasing the characteristic relaxation time λ_m of the polymer/filler composite material, thereby increasing De for fixed ω. Comparison of the TPS results with the master curves from TTS analysis reveals striking similarities in the extreme frequency regions (see Figures 4.14

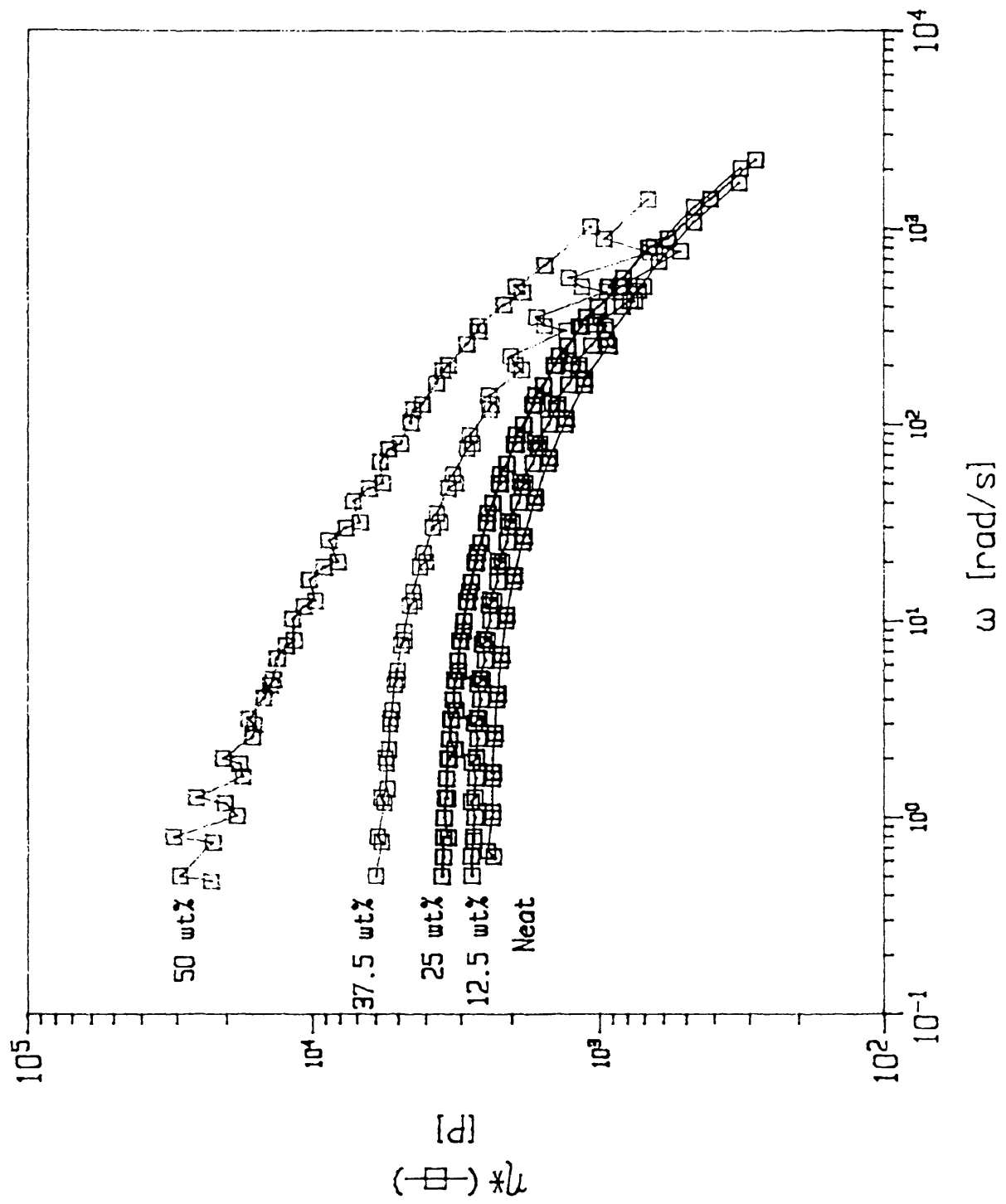

Figure 4.14: Time-temperature superposition result: Master curves of filled system data referenced to T=185°C.

and 4.15, respectively). In the low frequency region TTS results indicate zero-shear viscosities (η_o) of $\eta_o|_{\text{neat},12.5} \approx 2.5 \times 10^3$ poise; TPS results in $\eta_o|_{185°\text{C}} \approx 2.2 \times 10^3$ poise. Zero-shear viscosity vanishes with decreasing temperature (TPS) much the same as with increasing filler loading (TTS). In the high frequency region, the master curves from both analyses tend together, indicating dominance of the rheological response by the polymer chain hydrodynamics. Essentially, material relaxation is being dominated by polymer chain dynamics as the interactions of the filler particles become insignificant.

The smooth superposition of the data in the low frequency region on the T=185°C curve should be noted. In this region, the morphology is very reproducible across filler loading levels and well characterized. As the temperature decreases the scatter increases indicating sample inhomogeneities based on filler loading. These discrepancies are believed to be based on thermal effects at the filler/polymer interface.

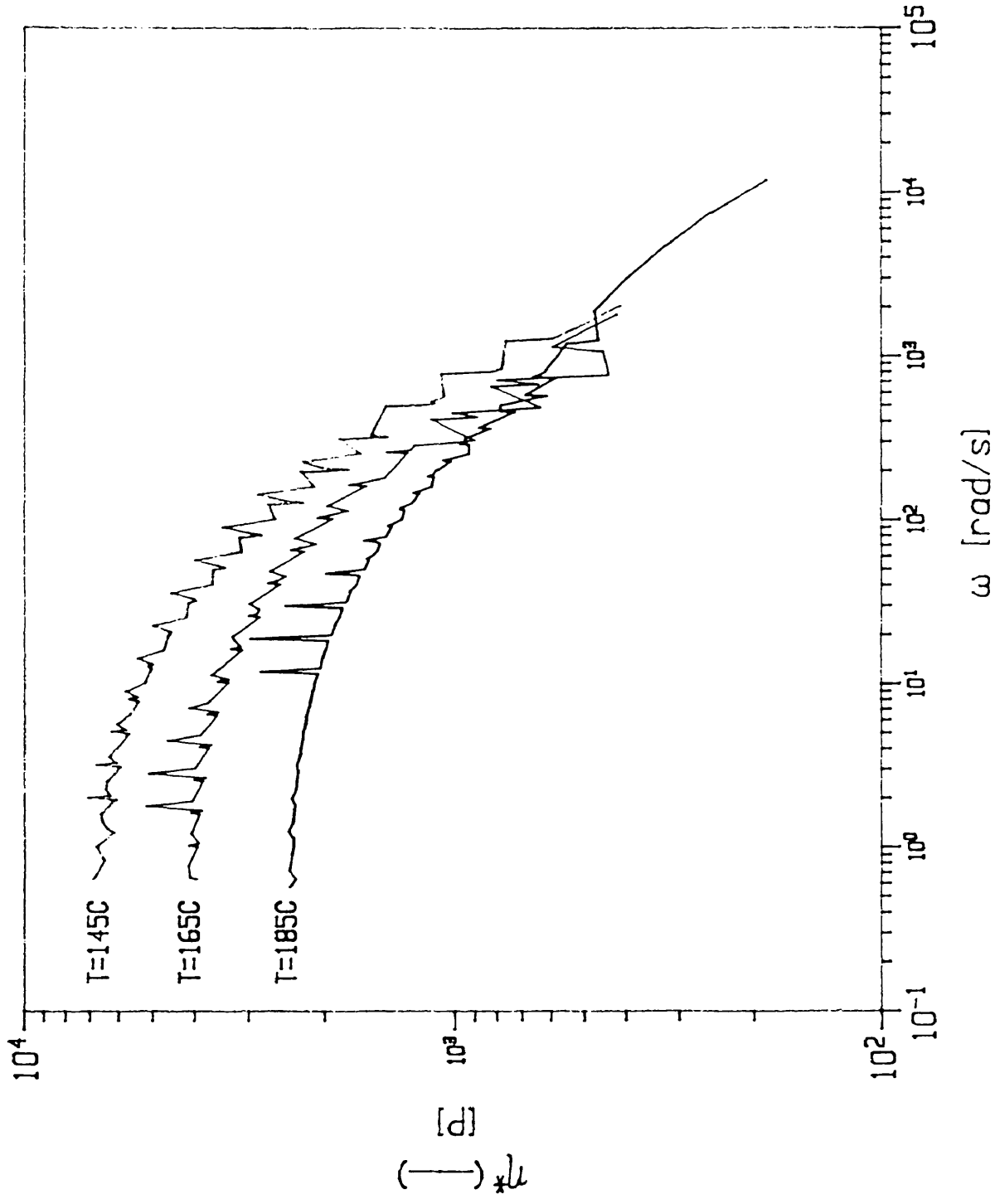

Figure 4.15: Time-particle superposition result: Master curves of filled system data referenced to neat sample.

4.4 Particle Interaction Investigation

Preliminary filled system analysis has provided evidence of unique filler interaction behavior. The rheological results indicate apparent microscopic phenomena present in the samples. The unusual flow behavior exhibited by this system includes shear-history-dependent properties such as a hysteresis envelope, time-dependent modulus, and a low shear rate modulus plateau. Another important property exhibited by this system in terms of microscopic structural formation is the existence of an apparent yield stress value.

4.4.1 Hysteresis Envelope

The mechanical hysteresis of a polymer represents the fractional energy that is lost as a result of subjecting that material to a defined deformation cycle (Gorce et al. 1993). Specifically in polymeric systems, a hysteresis is defined as the irreversible loss of polymer chain memory upon successive deformations. Often, polymer systems modified by the addition of another structure forming material exhibit hysteresis behavior. This added material may be of a particulate or rod-like nature having the tendency to form network structures (flocs or aggregates) from particle-particle interactions, especially if the particles are colloidal in nature.

Rheological experiments were conducted in both forward and reverse frequency sweep modes to elucidate specific time and shear history behaviors. Figure 4.16 shows the results of frequency sweep experiments for a 12.5 wt% sample and Figure 4.17 for a 25 wt% sample. Hysteresis envelopes are not found in the lower salt loaded samples. It is believed that the particle concentration is not high enough for long-range structural interactions; rather, the particles are sufficiently separated from each other such that the system behaves as a dilute suspension.

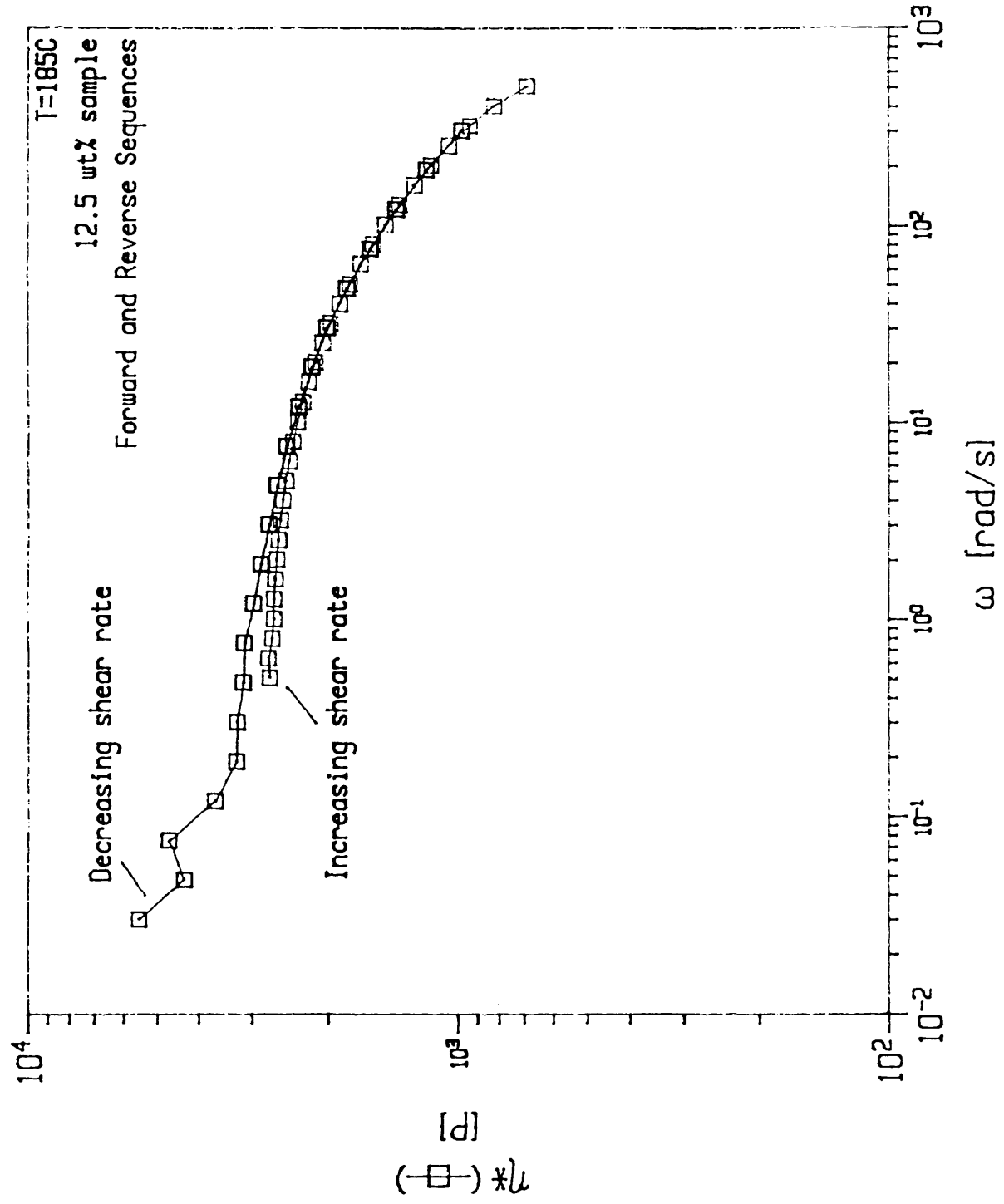

Figure 4.16: Complex viscosity (η_*) versus shear rate (ω). Notice a hysteresis does not exist at this weight loading.

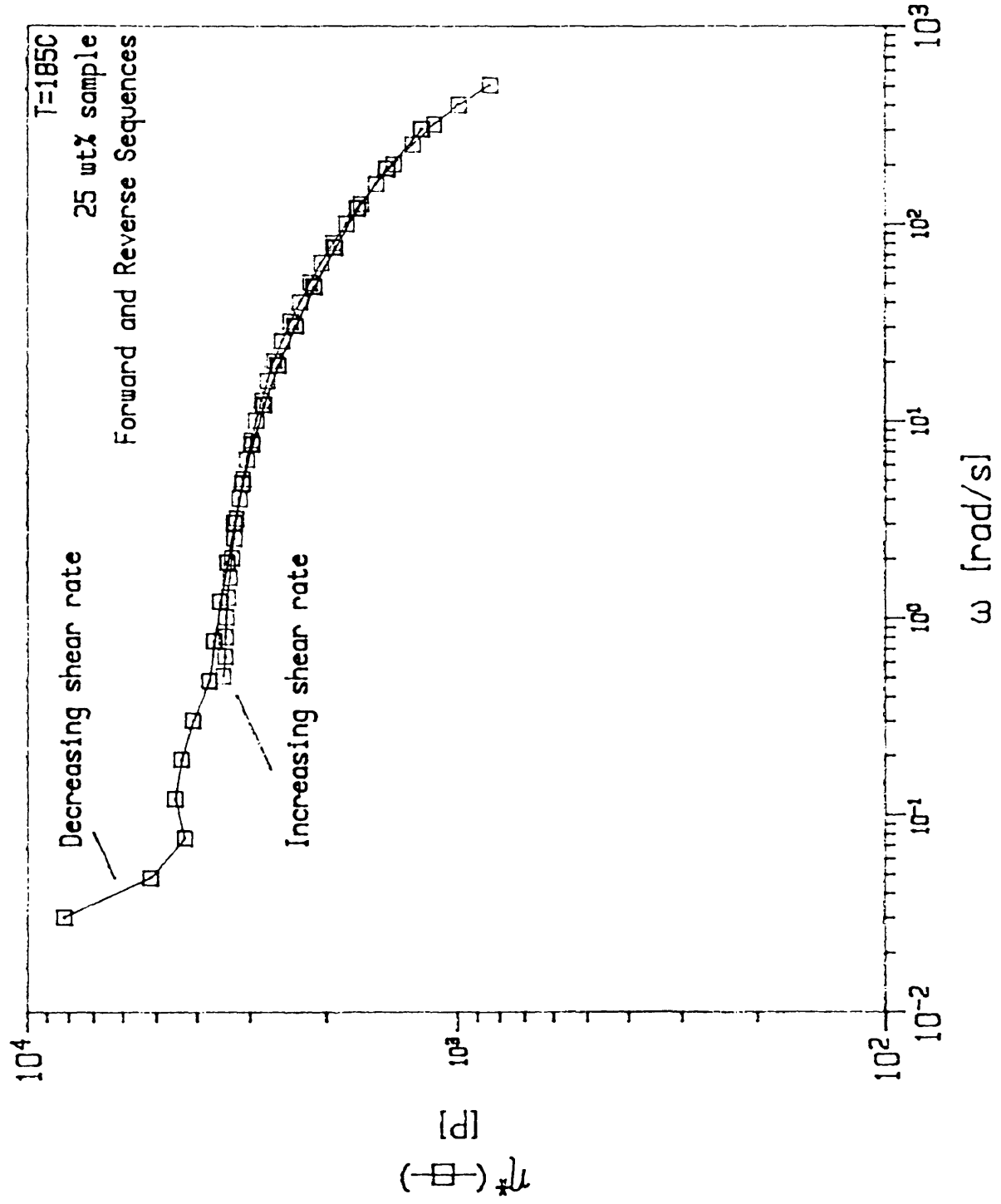

Figure 4.17: Complex viscosity (η^*) versus shear rate (ω). A hysteresis loop is not defined at this weight loading.

The onset of the hysteresis envelope occurs with the 37.5 wt% samples (see Figure 4.18). The hysteresis is more evident in the 50 wt% samples as shown in Figure 4.19. At these higher filler loading levels, the particles are sufficiently close together to promote interactions in the solid phase. This results in a network of particles which exhibits solid-like behavior evident under shear. The hysteresis envelope corresponds to the breakup of flocculates during the forward frequency sweep while in the reverse frequency sweep, the rheological response is not influenced by the presence of the solid networking structure. Hence, this disparity in viscosity measurements is due to the absence of the solid-like structure effects characteristic of the interacting solid filler.

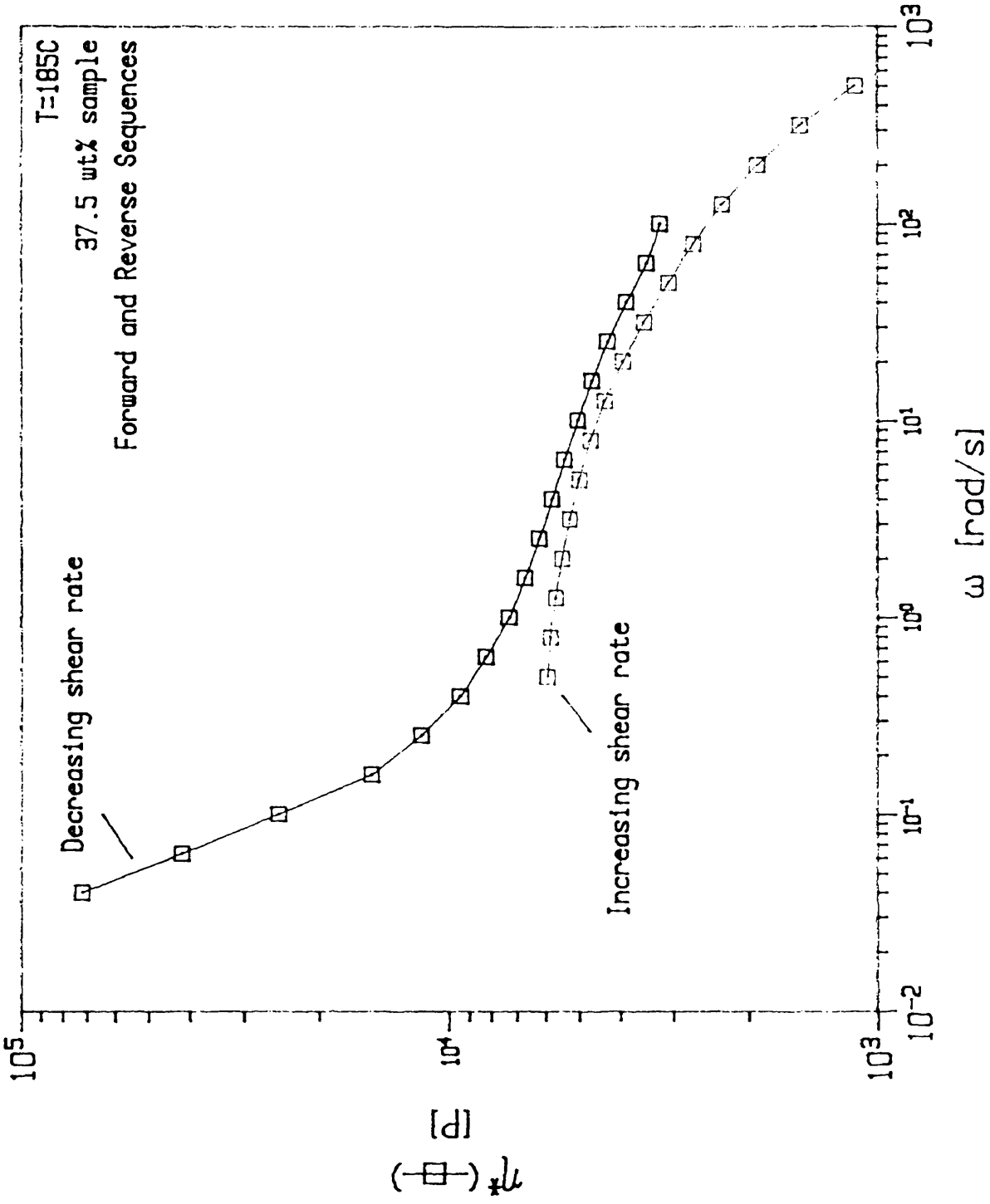

Figure 4.18: Complex viscosity (η^*) versus shear rate (ω). Initial evidence of hysteresis envelope.

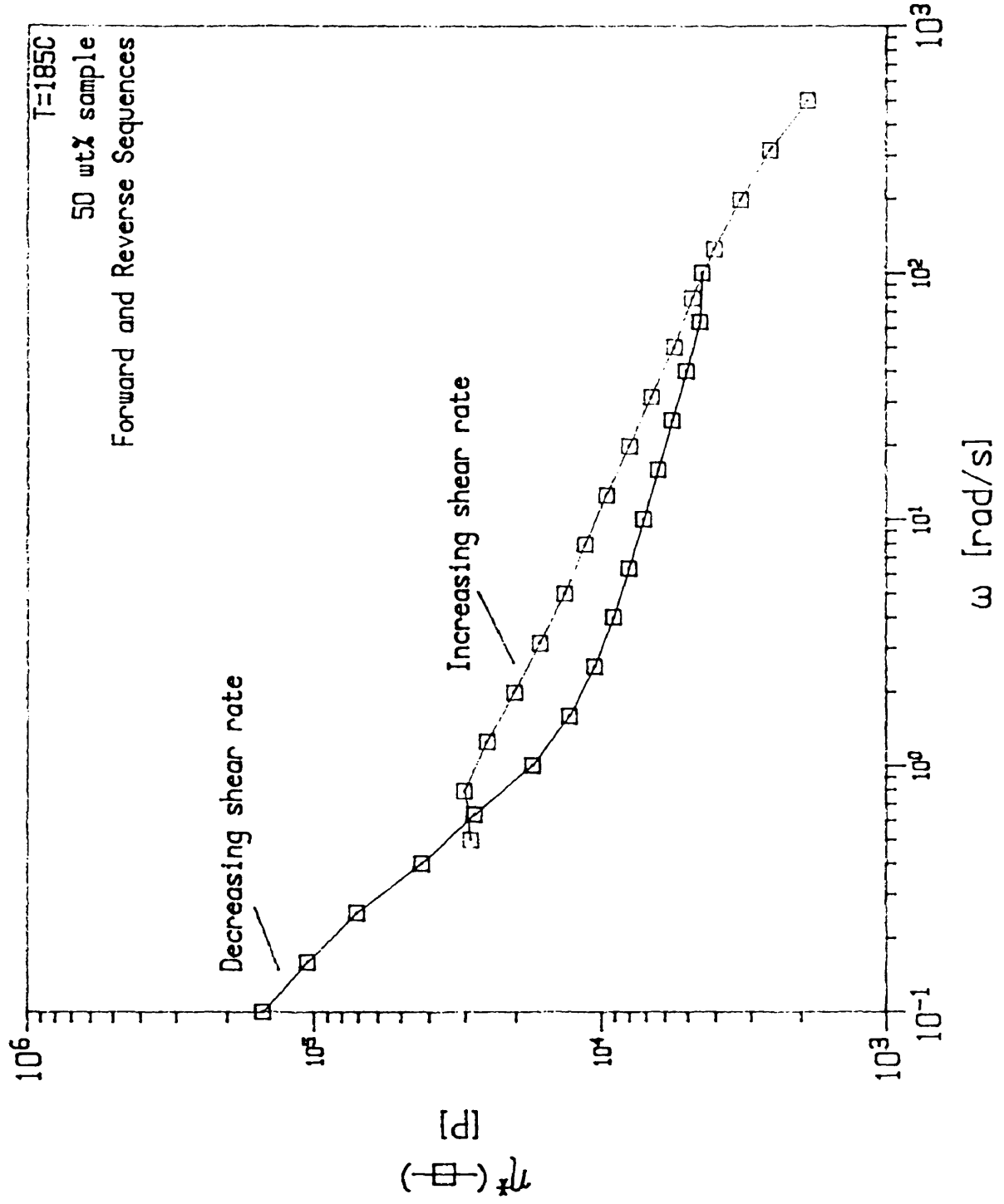

Figure 4.19: Complex viscosity (η^*) versus shear rate (ω). The hysteresis envelope is well defined in filled sample.

In a separate set of experiments, the shearing frequencies were cycled from 0.5 sec^{-1} to 500 sec^{-1} then immediately from 300 sec^{-1} to 0.1 sec^{-1}, imitating a dynamic thixotropic loop test. In this test, the rheometer was configured at 145°C to reduce the amount of sample degradation that occurs at elevated temperatures. This filled system rheological response is striking and is depicted in Figure 4.20.

Neglecting the as-molded sequence, the flow curves for both the forward (labeled 1, 3, 5) and reverse (labeled 2, 4, 6) sequences tend towards each other in the limit of low and high shear rates, respectively. The flow curves in both are reproducible after the original as-molded sequence. The response at low shear rates is accounted for by the dominant nature of the particle aggregate/flocculate structure. At high shear rates, the hydrodynamics of the polymer dominates, but the presence of the filler causes the enhanced viscosity described above. The curve separation, i.e. hysteresis envelope, arises from the formation and destruction of flocs and aggregates of the filler particles under separate sequences of reverse and forward shearing, respectively, and the subsequent irrecoverable loss of energy associated with a mechanical hysteresis.

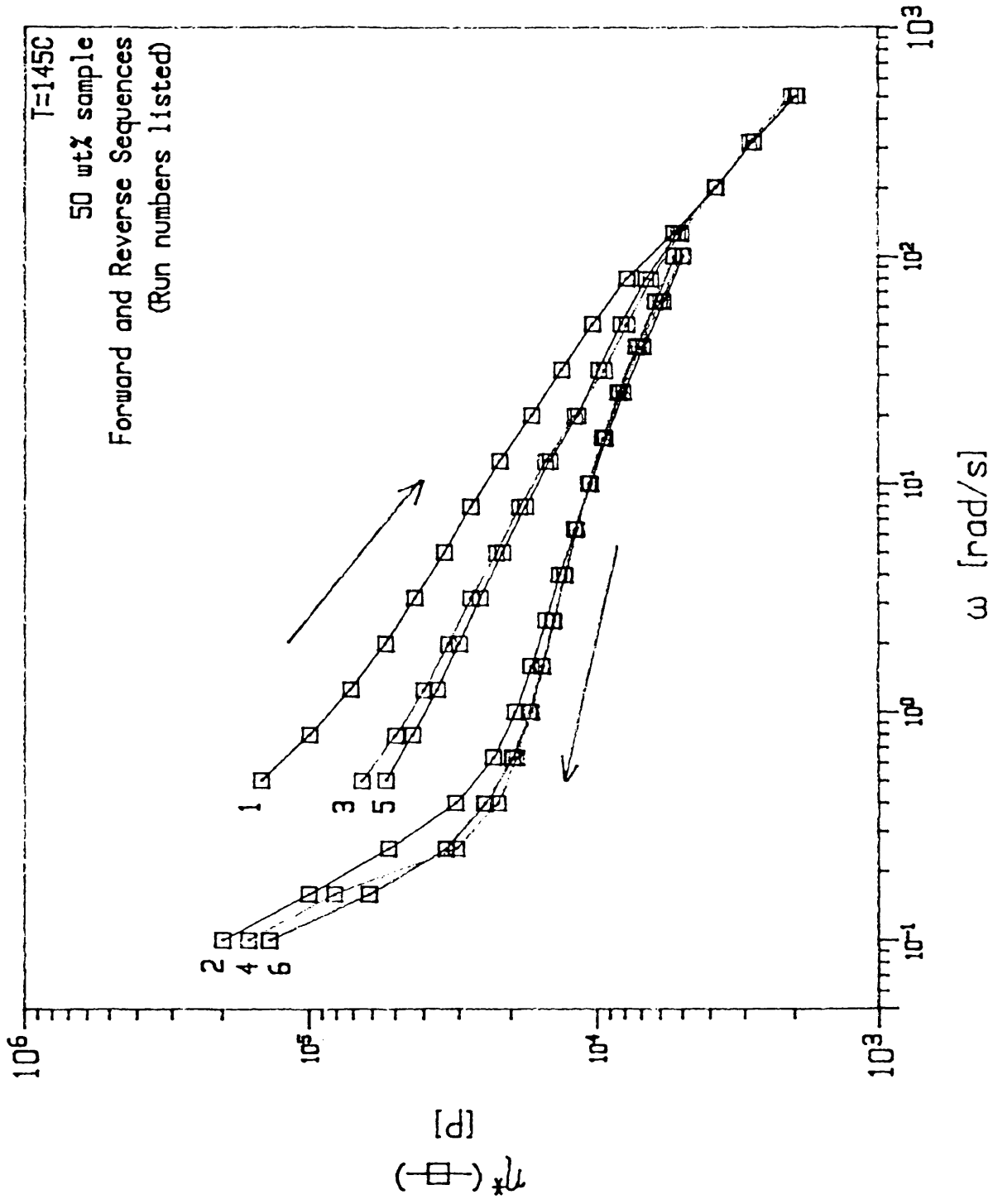

Figure 4.20: Complex viscosity (η^*) versus shear rate (ω). Experimental dynamic thixotropic loop test shows large hysteresis envelope and shear history dependence.

4.4.2 Time-Dependent Modulus

Because of the nature of hysteresis envelopes in filled systems, the shear dependent properties can also be depicted through a time dependent modulus. For sudden deformations (short times, high shear rate), viscoelastic materials behave as solids and will recoil to recover their original shape. As the time scale of the deformation process increases (long times, low shear rate), the material exhibits liquid-like behavior, progressively losing ability to return to its original shape.

The time dependent change from a liquid-like material to one that has more solid-like characteristics is exhibited as an *increase* in the storage modulus of a 50 wt% filled sample shown in Figure 4.21. In order to ensure that the sample was homogeneous and without the internal as-molded structure, the sample was pre-sheared such that the flow curves were reproducible. Immediately after the sample was pre-sheared, a constant shear rate of 0.5 sec^{-1} was applied at 50% strain. The modulus increase with time can be attributed to the formation of a network structure of particles; the network structure imparts the solid-like effect evidenced by the increase in G'.

The breakup of internal structure is depicted in Figure 4.22. The material was pre-sheared to ensure the *formation* of network structure. After pre-shearing, the material was sheared at a constant value of 500 sec^{-1} and 15% strain. This procedure was conducted to show the time dependent destruction of the internal network structure, depicted by the decrease in the storage modulus with time.

Through comparison of the structure formation and degradation in the filled sample through analysis of the storage modulus as a function of time, the time scales of formation and destruction appear very similar. At approximately $t_{expt} = 100$ seconds, the rate of formation and destruction are at their respective maximums,

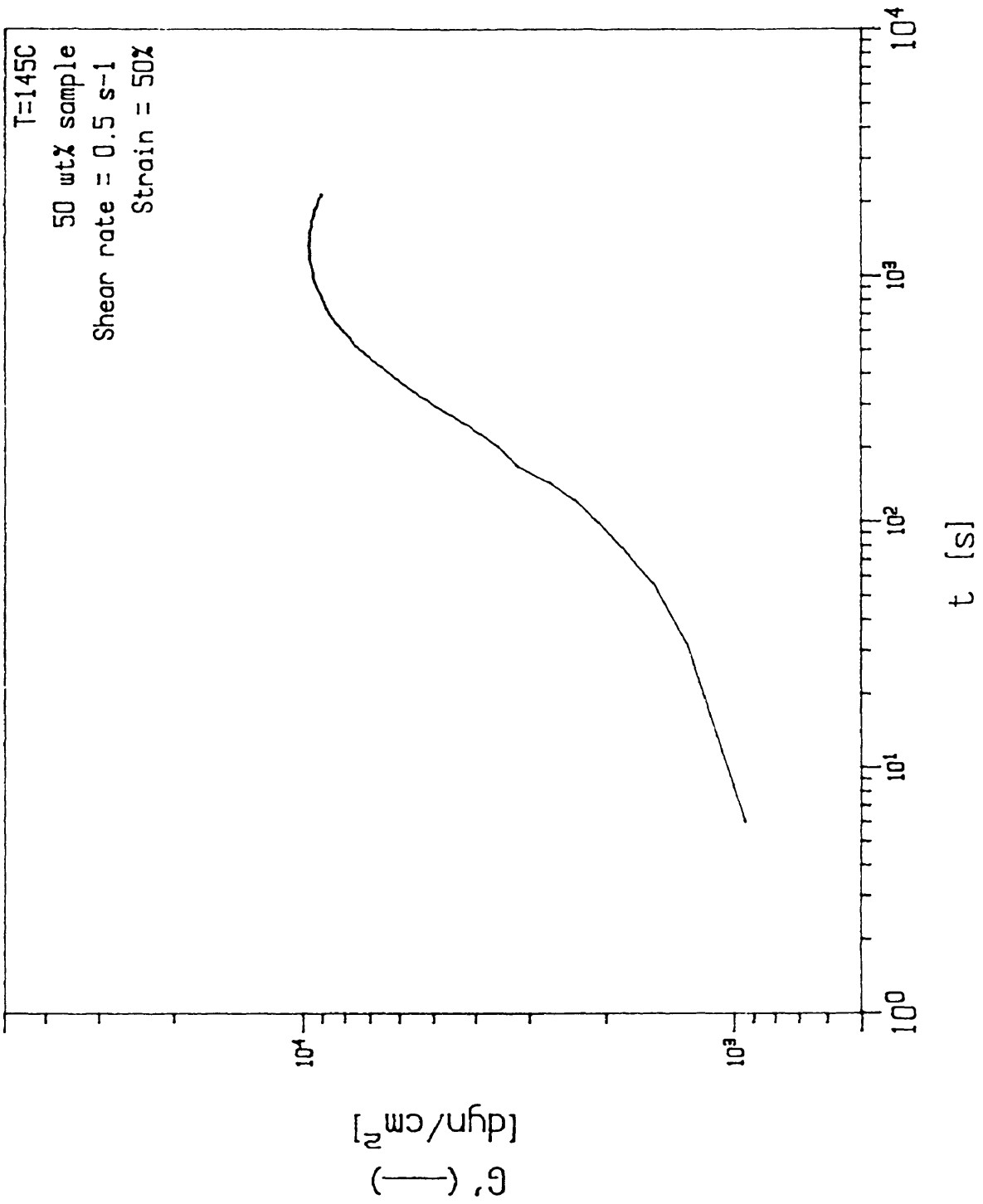

Figure 4.21: G' storage modulus versus time. Noticeable increase due to solid-like structure formation with time.

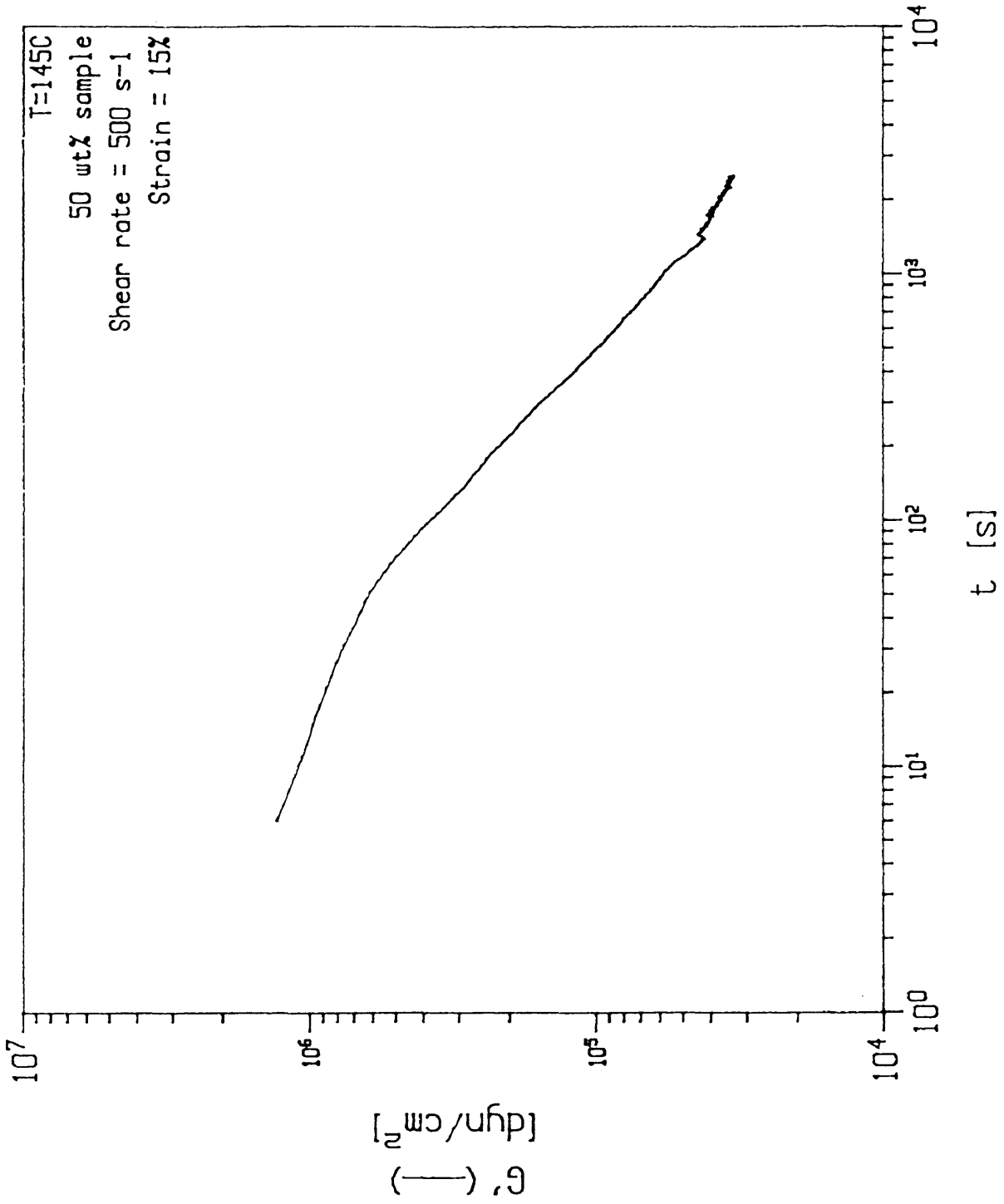

Figure 4.22: G' storage modulus versus time. Observed decrease due to solids breakup and expression of liquid-like behavior.

indicating structure history independence with respect to the particle interaction kinetics. Although not depicted in the time scale of this result, the G' curves are believed to eventually cross, as the samples attain homogeneous morphologies.

4.4.3 Low Shear Rate Moduli Plateau

As Li and Masuda (1990) found in their studies of calcium carbonate-filled polypropylene, viscoelastic behavior at high frequencies is dominated mainly by the matrix polymer. Similar responses have been observed in the present system (see Section 4.4.1).

Based on the work by Li and Masuda, further evidence that molded-in structure exists in the samples can be seen in Figure 4.23. A frequency-invariant plateau is evident in sequence # 1. As the material was repeatedly sheared (sequences 2-4), the low frequency modulus decreased to an equilibrium, reproducible value suggesting the dissipation of an internal network structure.

Data from a previous set of experiments (see discussion of dynamic thixotropic loop test in Section 4.4.1) can also be analyzed for storage modulus enhancements. In the low shear rate region of Figure 4.24, an increase in the storage modulus begins at approximately 0.3 sec^{-1}. It appears that a cascade of networking flocs forms from the low oscillatory shearing of the disrupted solids matrix. This is exhibited through an *increase* in the storage modulus G' with decreasing frequency. Assuming low shear rate data $\geq 10^{-1}$ sec^{-1} exists in the forward direction, the low shear rate modulus appears to be frequency invariant. Weak, gel-like, colloidal stabilized structures have been proposed in filled systems where the low shear rate flow properties become shear-independent (Park 1990). The constant value of the G' plateau (4×10^3 $dyne/cm^2$) remains constant until the flocs are disrupted and the polymer-filler system begins to exhibit frequency dependent modulus values at approximately 0.3 sec^{-1}. This type of response suggests the existence of an apparent yield stress in the samples as a consequence of the internal solid-like structure.

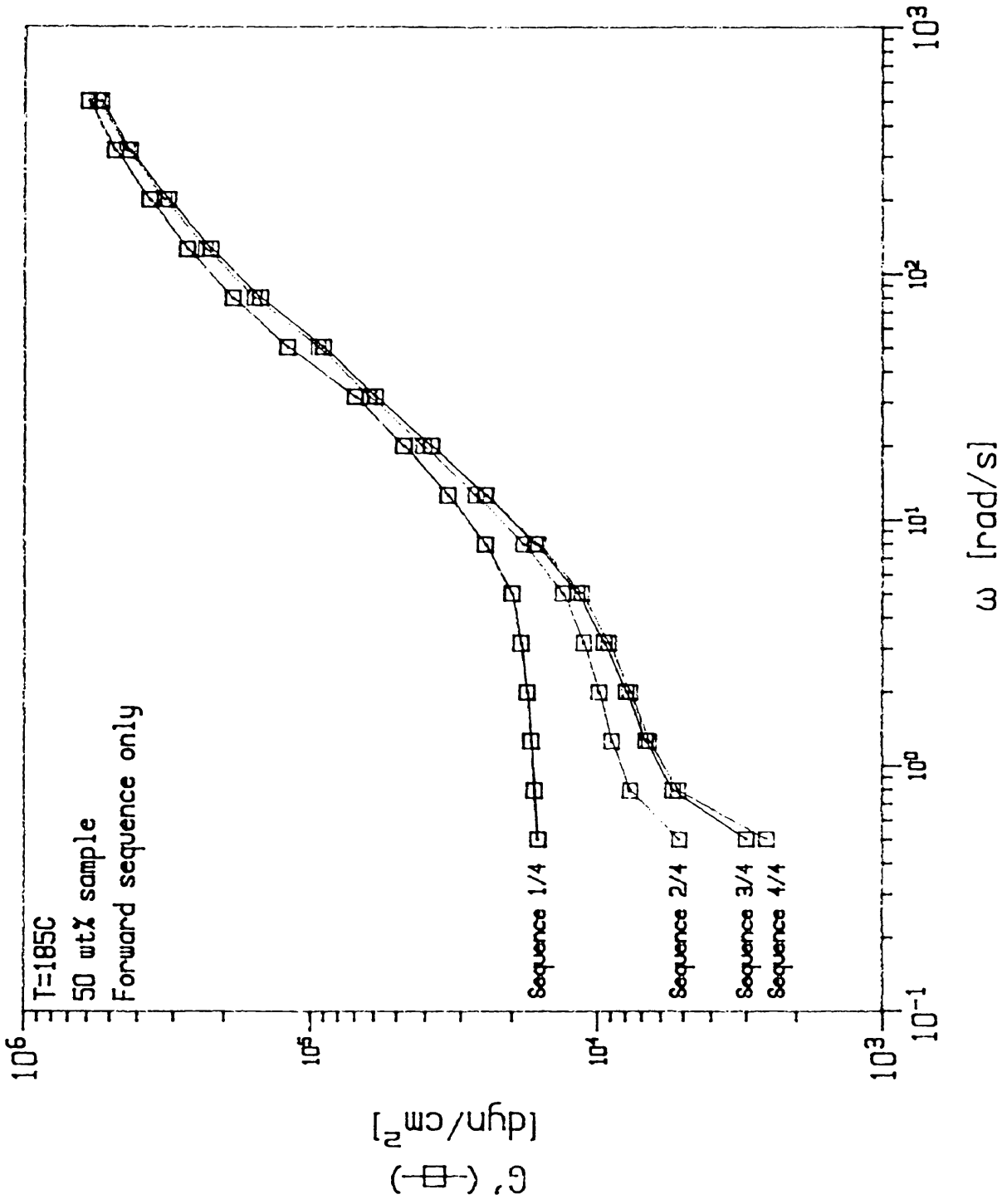

Figure 4.23: G' storage modulus versus shear rate (ω). Sequences 1/4 - 4/4 shown to illustrate molded-in structure.

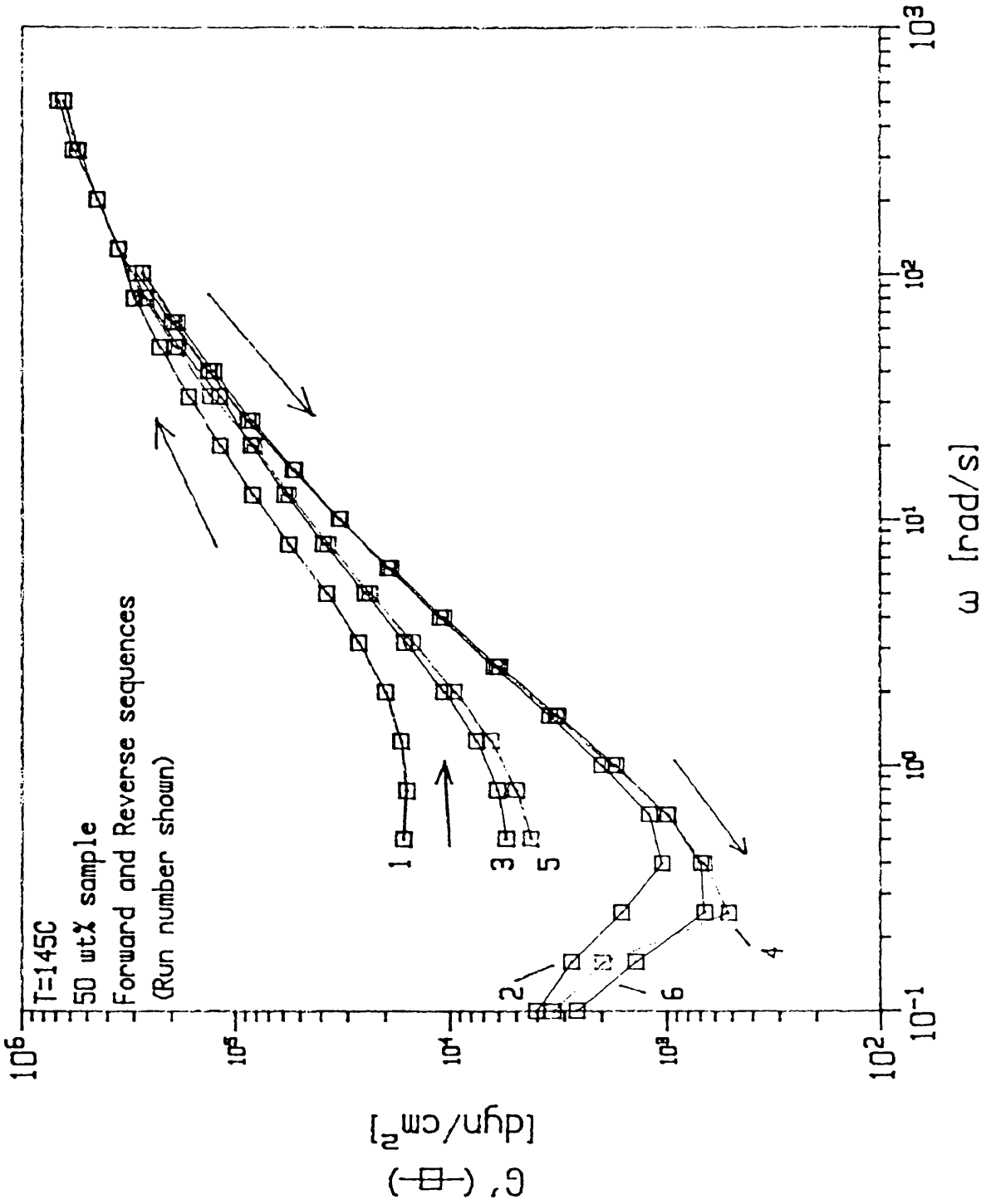

Figure 4.24: G' storage modulus versus shear rate (ω). Evidence of low shear rate modulus plateau indicative of structure.

4.4.4 Apparent Yield Stress

In Section 2.3.2 yield stresses were found where the viscosity turned toward infinity indicating the presence of a solid-like structural component in the melt. From the data in Figure 4.25, the yield stress is determined for the 50 wt% sample at 145°C as approximately 2×10^4 dyne/cm^2. Based on previous results which conclusively showed the thermal dependence of relative viscosity, yield stresses are also calculated at the higher temperature believed to be more representative of the filled system rheological behavior. At T=185°C, both the 50 and 37.5 wt% exhibit yield values as shown in Figure 4.26. The yield stress associated with the low filled samples (12.5 and 25 wt%) is assumed to be a spurious result of the low oscillating frequency and the resolution of the torque transducer. The data set collected at T=145°C is incomplete due to the lack of low strain experimentation. It is entirely possible that yield stresses exist in the 37.5 and lower wt% samples.

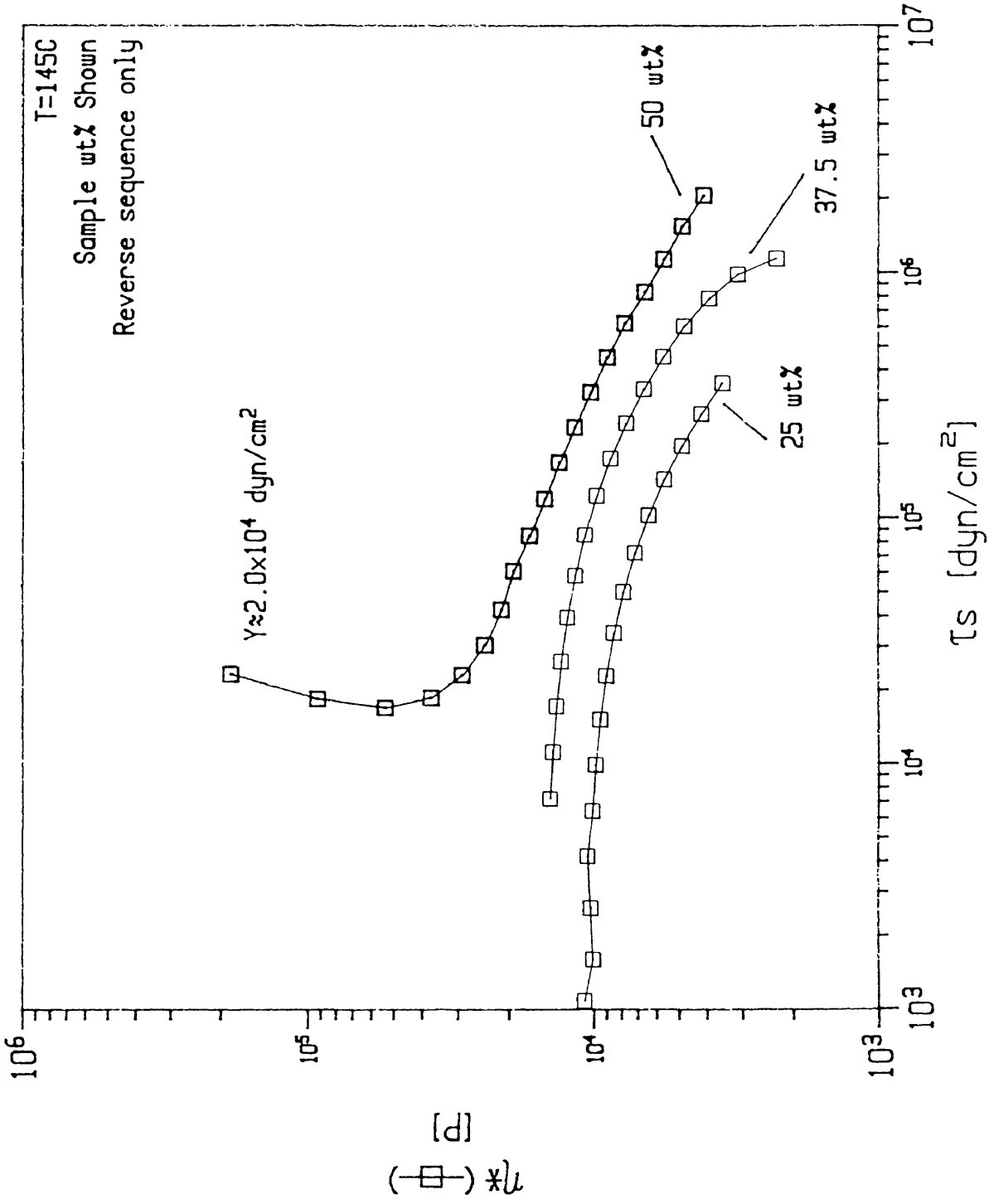

Figure 4.25: Complex viscosity (η^*) versus shear stress (τ_s). 50 wt% sample has a yield value of approximately 2.0×10^4 dyne/cm^2.

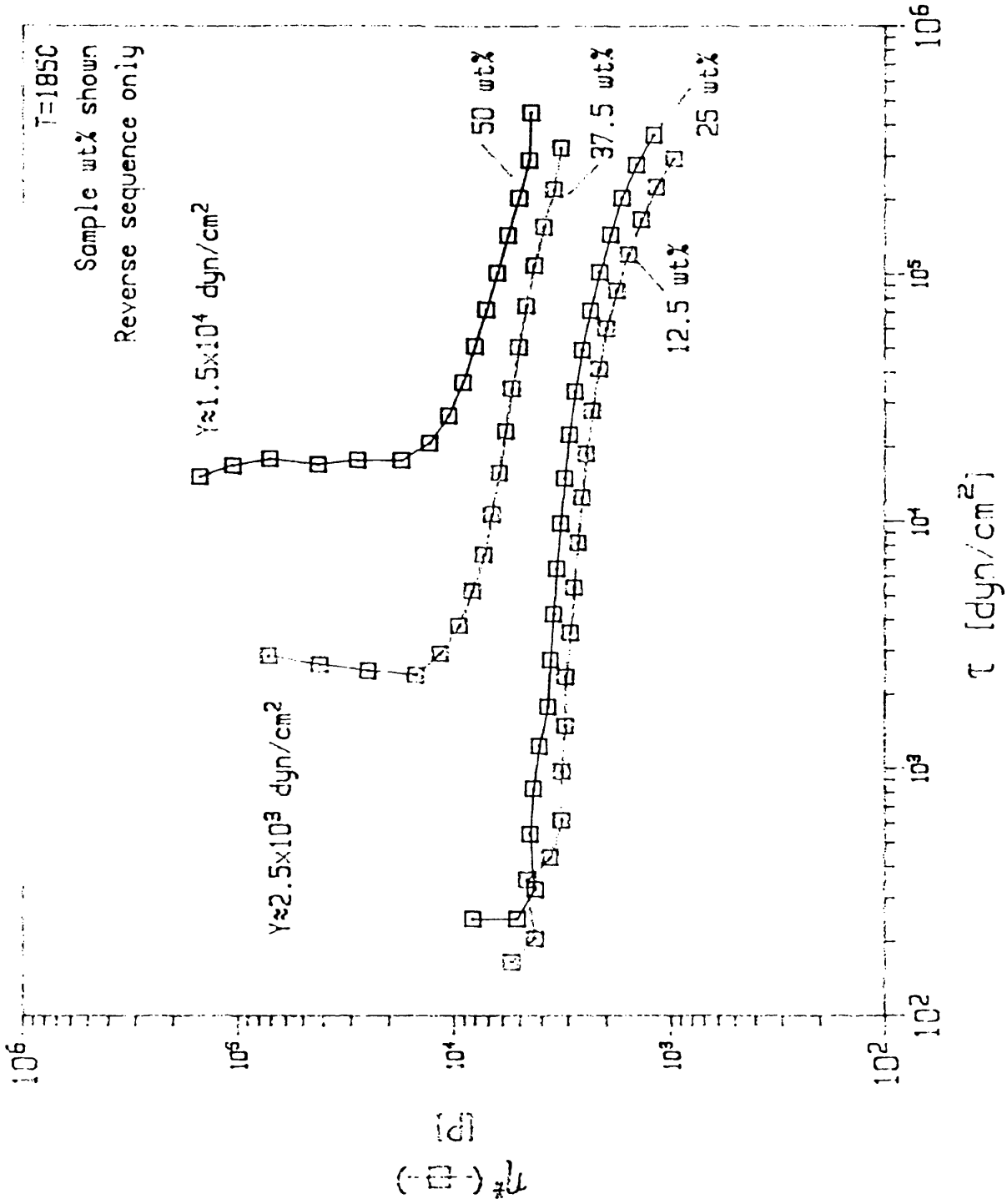

Figure 4.26: Complex viscosity (η^*) versus shear stress (τ_s). Both 50 and 37.5 wt% samples show definite yield values.

4.5 Numerical Simulation

4.5.1 Model Generation

Geometric models of the die region of the Berstorff twin screw extruder are generated with FIDAP's graphical user interface (GUI). Specific die dimensions are incorporated into the FIDAP model through equatorial measurements for two-dimensional representations. Axi-symmetric representations of the die are used for computational convenience and to produce physically realistic flow results. Quadratic elements are used in the mesh as shown in Figure 4.27. Material properties including mixture density, specific heat and conductivity are calculated as weighted averages of the two components: polyethylene polymer matrix and surrogate nitrate salt waste filler. Thermal boundary conditions are established from actual extruder practice runs. The inlet velocity profile is modelled as the steady state flow field of a Power-Law fluid at known throughput levels. The data in Figure 4.28 represent the velocity profile as a function of radial position in Poiseuille flow. Symbols represent analytical solutions of pipe flow for a Power law fluid under three volumetric flowrates. The solid curves show the polynomial fit used as input in the FIDAP CFD package. Simulation results include velocity profiles, temperature distributions, shear rate gradients and pressures (Figures 4.29a, b, c, and d).

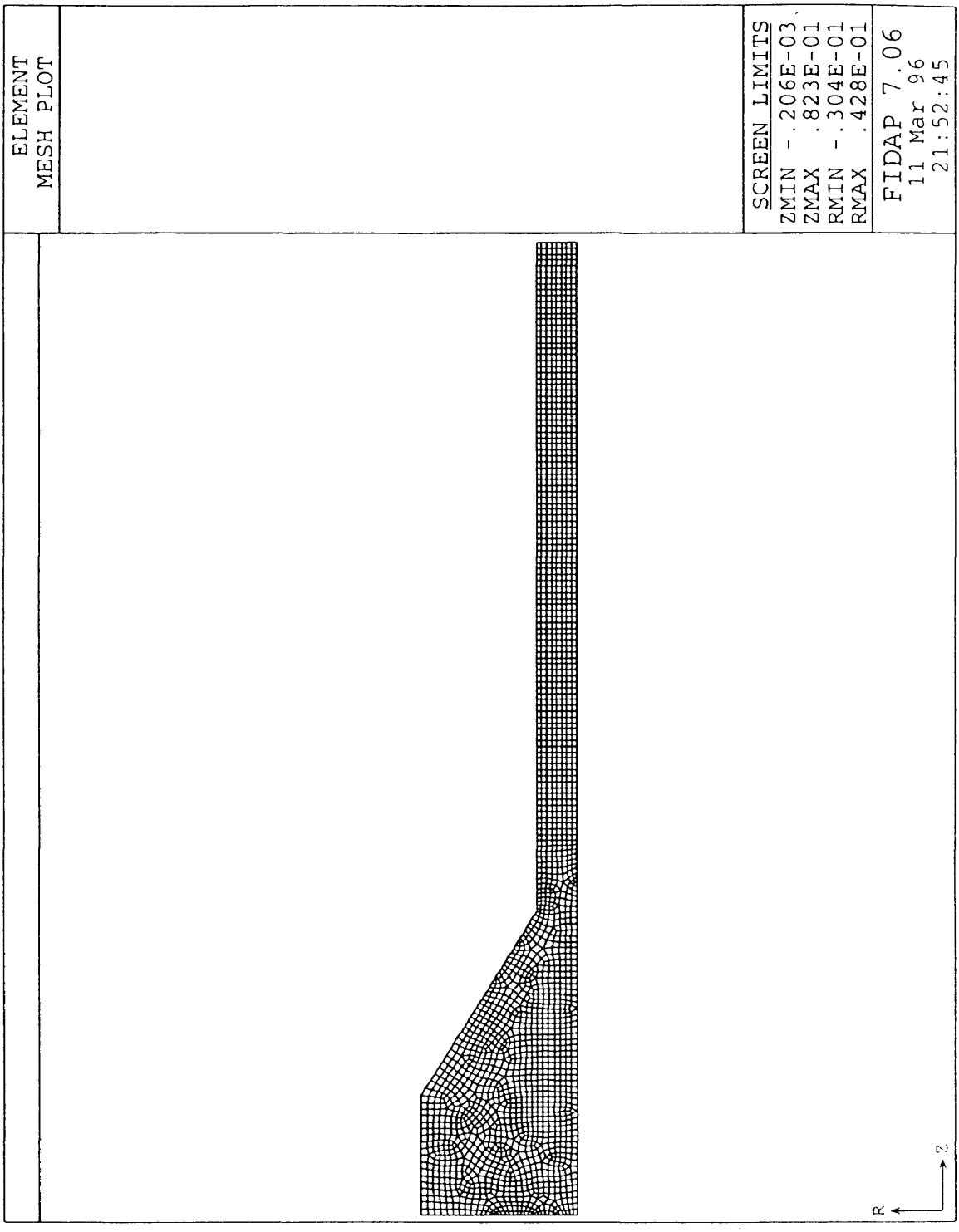

Figure 4.27: FIDAP output. This is a representative mesh plot for axi-symmetric solution domain.

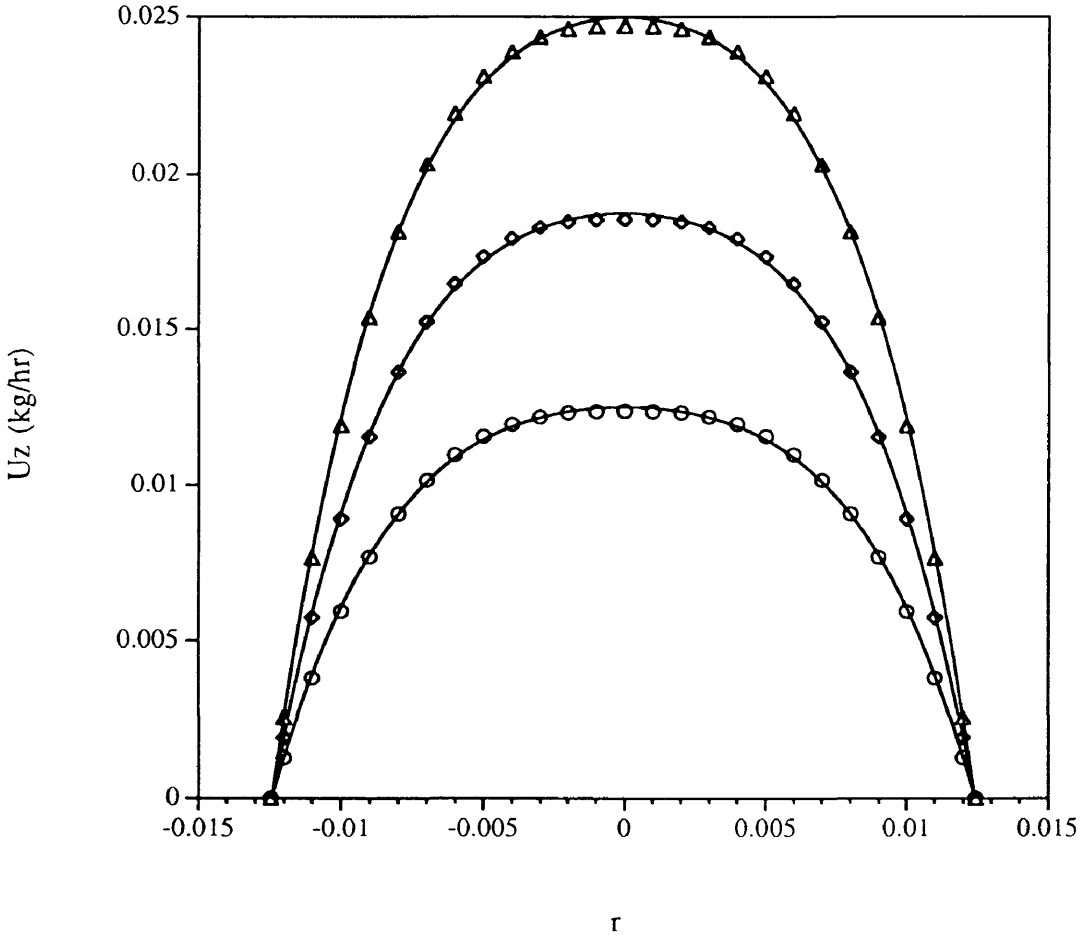

Figure 4.28: Velocity profile as a function of radial position in Poiseuille flow.

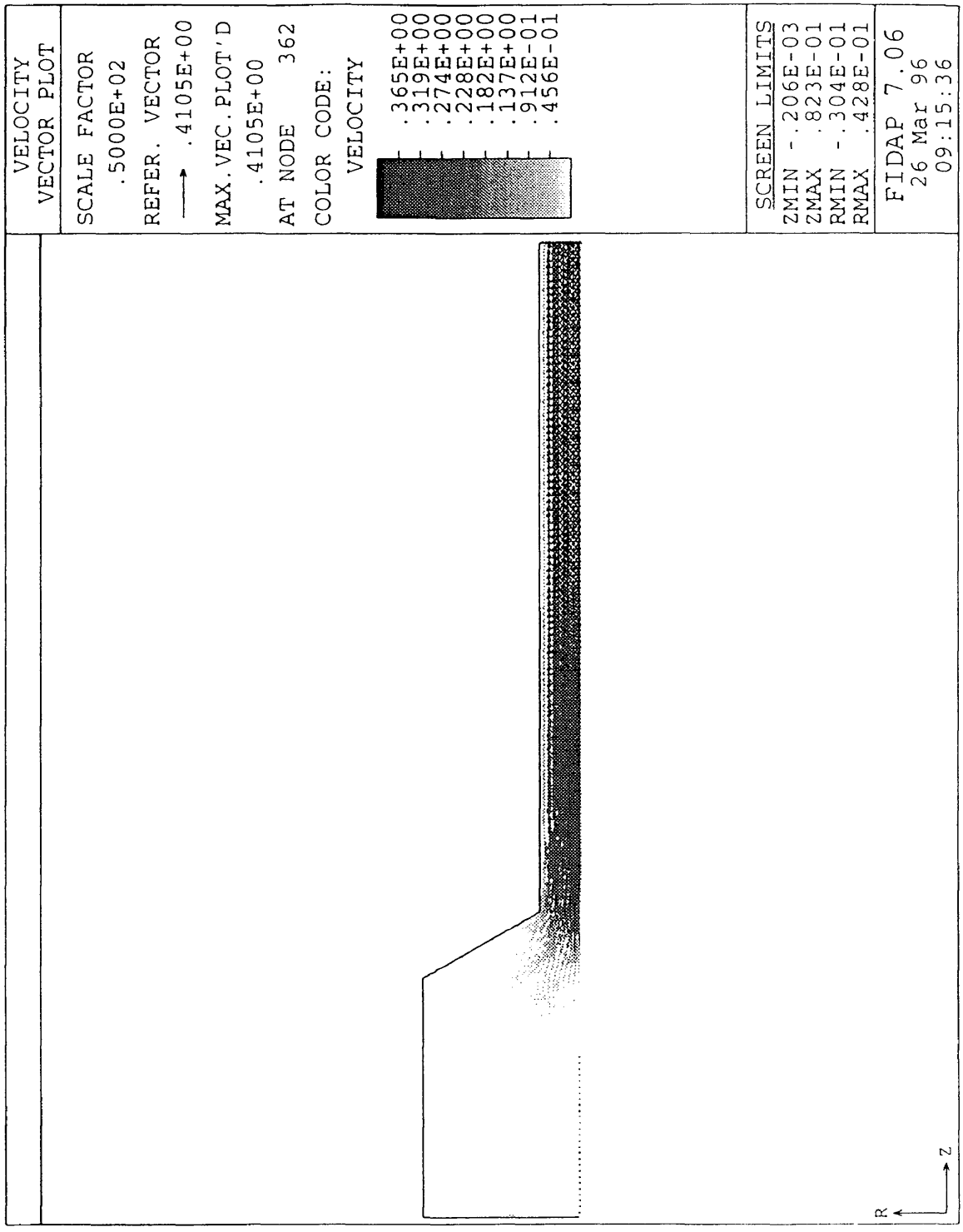

Figure 4.29: Representative FIDAP results: a) velocity profile for 60° cone angle;

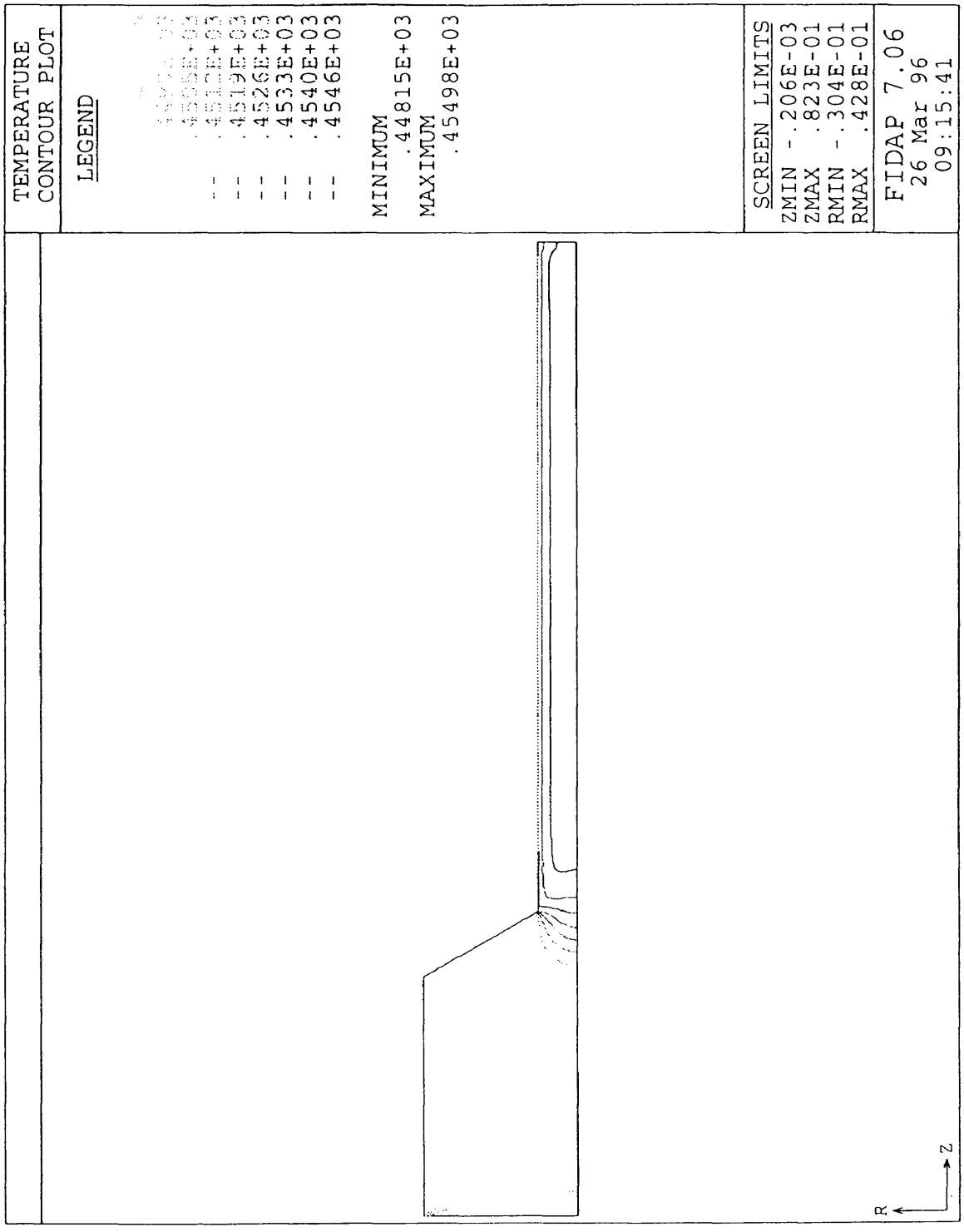

Figure 4.29: b) temperature contours,

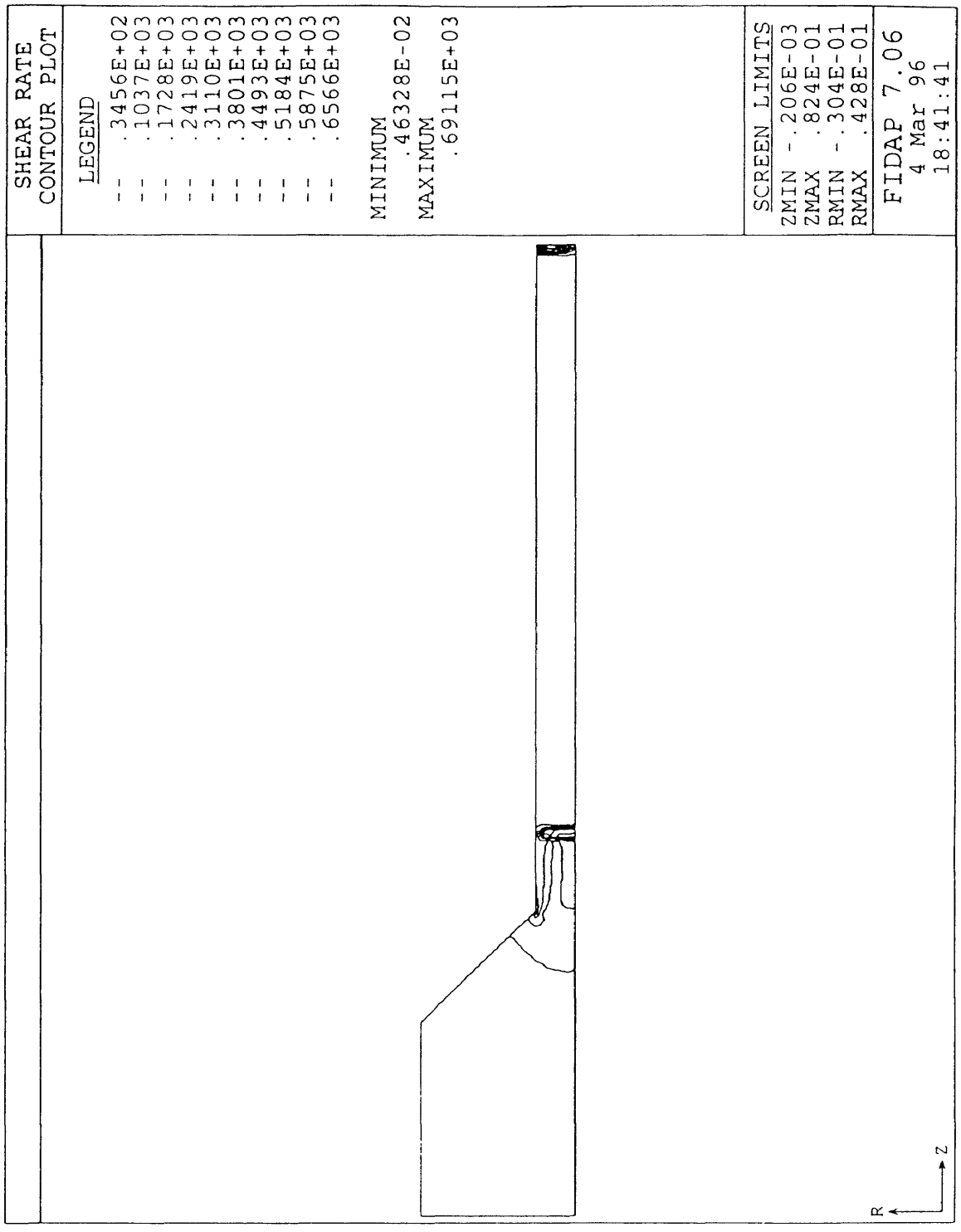

Figure 4.29: c) shear rate contours,

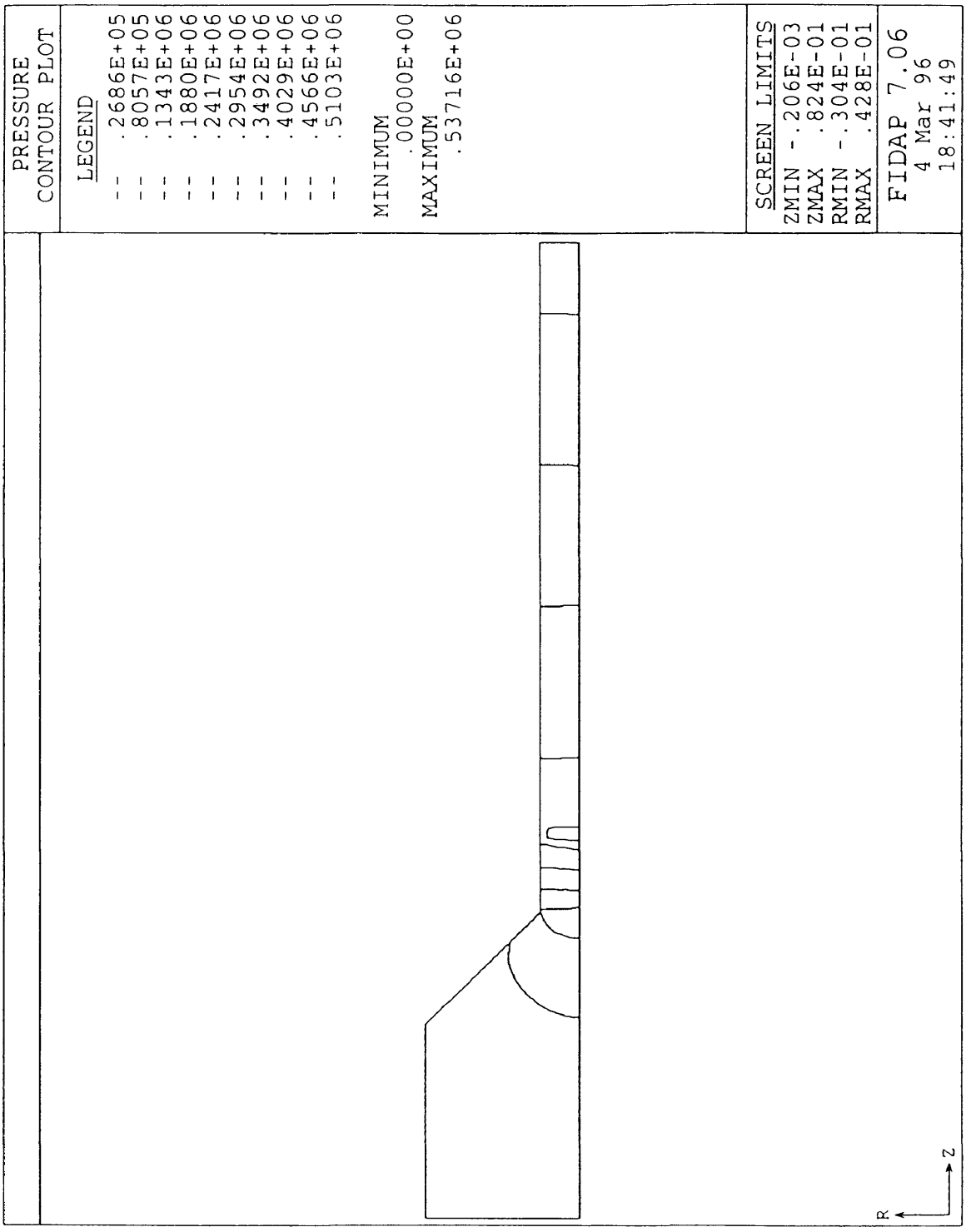

Figure 4.29: and d) pressure contours for a 30° cone angle.

4.5.2 Comparison with Extrusion Operation

The pressure drop across the die was calculated from the numerical simulation data generated from FIDAP and compared to the values collected from the pressure transducer in the die region of the extruder during the encapsulation operation. As demonstrated in Figure 4.30 the simulation results closely match those of the extruder, to within extruder pressure variability. The significance of this result lies in the ability to take rheological data, parameterize a non-Newtonian constitutive equation, implement a numerical solution of the equations of motion and energy, and produce physically realistic data which closely matches experimental results of the same type of flow.

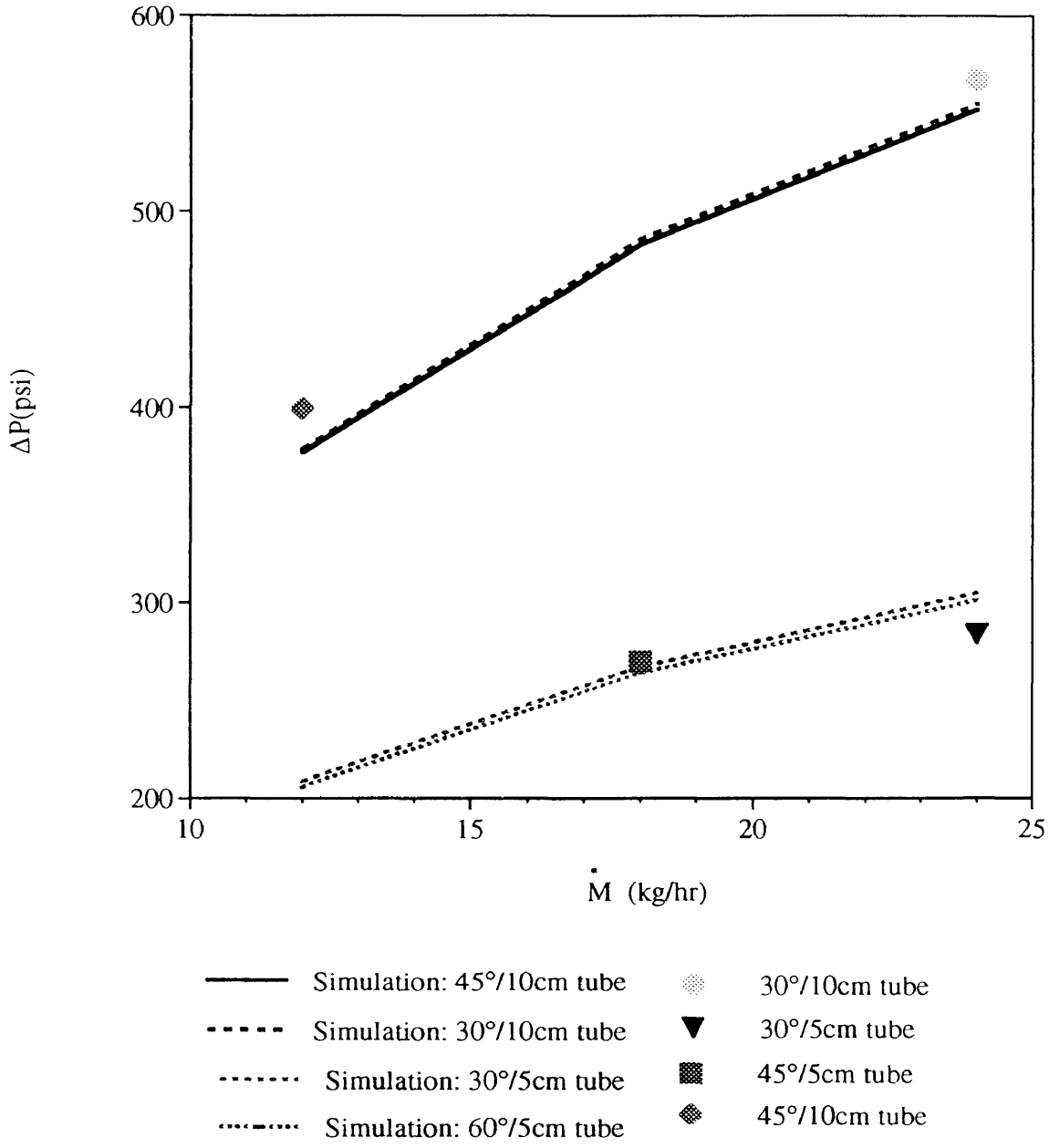

Figure 4.30: Pressure drop from extrusion operation compared to FIDAP results under same flow conditions.

Chapter 5

CONCLUSIONS

Analysis of the surrogate waste salt encapsulated in low density polyethylene provided by the RFETS included rheological characterization of the filled system and implementation of these results in a CFD flow modelling program for extrusion process optimization. The rheological results also uncovered complex interactions of the polymer matrix and salt filler. The conclusions generated from the rheological analysis and CFD flow modelling are presented below.

5.1 Rheological Measurements

Filled System Rheological Protocol Development

The successful development of a procedure for testing the flow response of the filled system has been presented. Through the coordination of series of frequency sweeps and additional time delays between sweeps, the as-molded structure present in the samples could be destroyed. In order to maintain sample linear viscoelasticity, the strain levels required dynamic adjustment. This adjustment, made during the frequency sweep experiment, resulted from strict determination of the limits of linear viscoelasticity.

The filled system was shown to exist in the same morphological state after successive shearing sequences as described by Han. Plots of $\log G'$ versus $\log G''$

showed the data to collapse to a single line. Hence, the superposition techniques used in the analysis were deemed valid. The columnating of data to a single line occurred to an appreciable extent when the samples were compared across all weight percents at constant temperature.

Filler-Dependent Calculations

Using Wildemuth's method for calculation of ϕ_m and $[\eta]$, values of filler density were determined. This was based on the premise that in the theoretical limit, both ϕ_m and $[\eta]$ would reach predicted values, known a priori to be approximately 0.68 and 2.5, respectively. Once a filler density was determined, the complex stress dependent maximum packing fraction was decoupled from thermal effects to produce a stress and thermally dependent maximum packing fraction value.

Relative Viscosity Calculations

Examination of the experimental relative viscosity data as a function of filler volume fraction normalized by the stress and thermally-dependent maximum packing fraction showed the characteristic increase predicted by theory. It is concluded that more data is necessary to complete the relative viscosity curve in the highly loaded region.

Comparison with published theory shows satisfactory agreement with both the Frankel and Acrivos equation and the Maron-Pierce-Kitano equation in the low loading region. As the volume fraction increases, the Frankel and Acrivos expression predicts a more realistic response based on the functionality of the normalized volume fraction.

Superposition of Rheological Data

The application of time-temperature superposition principles resulted in the generation of master curves of viscosity versus frequency for the filled system across all weight percentages. Generally thought to be an arduous procedure due to the unknown effects of filler interactions with the polymer matrix, the generation of master curves at constant filler loading level was completed in a straightforward manner. The ability to calculate master curves is believed to originate from the experimentally sound protocol developed to study the complex behavior of the filled system. Master curves for the neat, 12.5, and 25 wt% samples showed little scatter, even in the low frequency region. For the 50 wt% samples, the scatter is believed to be primarily due to anamolous thermal effects that were present in the system. Although all samples were found to be in the same morphological state by Han's analysis, superposition of the flow responses does not support this result in the low frequency regime. (See also the low frequency regime in Figure 4.7 on page 42).

The procedure for calculating master curves based on time-particle superposition is very similar to that used for TTS. The scatter exhibited in the master curves is thought to be due to the unknown thermal effects of the filler on the polymer matrix. Examination of the T=185°C curve shows excellent superposition of the rheological data across the entire frequency range when compared to the curves at 145 and 165°C.

5.2 Complex Filled System Rheological Phenomena

Several complex rheological behaviors were determined to be present in the filled system. All of the reported phenomena are based on the interaction of the filler with itself and/or with the polymer chains, some due to chemical effects on

the filler surface, others due to the solid-like network structure present when the particles were in contact. Particularly interesting is the effect of shear history on the samples. Separate shear history experiments were conducted which elucidated the kinetic behavior of structure formation and destruction.

Mechanical hysteresis behavior was observed in the samples through dynamic thixotropic loop tests. The hysteresis envelope was reproducible and suggested phase transitions of the filled system. The homogeneous filled system with dispersed flocculates and independent (possibly doublet or higher aggregate) filler particles coalesced into a structured network formed by the flocculating species at approximately the same value of frequency for each reverse frequency sweep. Structure growth dynamics were evaluated and shown to be similar to those of structure destruction. The time-dependent storage modulus showed an absolute maximum in slope at approximately the same elapsed time.

Yielding behavior typical of polymer systems filled with interacting particles was evident in the higher filled samples. The yield stresses were easily detected in the reverse frequency sweep mode whereas yield stress values were not determined from the forward frequency sweeps. The data set at T=145°C is incomplete, necessitating further low temperature, low strain experimentation.

5.3 Computational Fluid Dynamics Flow Modelling

A finite element solution to the equations of motion and energy with the Power Law constitutive equation in a known geometry was implemented to determine the flow behavior in the extruder die region. Because of the robust nature of the solution method, even more complicated flow geometries can be simulated such as the flow between extruder elements or the free surface flow of the extrudate

exiting the die.

From the FEM analysis using the filled system rheological data, several flow parameters were calculated including thermal contours, streamline velocities, and pressure drops. Specifically, the calculated pressure drop was found to match very well with that of the extruder during operation. Success of this type of analysis exemplifies the utility of reliable rheological data in coordination with computer modelling to predict potentially complex flow behavior in arbitrary geometries. This has economic significance, as the costs associated with die design, manufacture, and testing associated with filled system extrusion are minimized.

REFERENCES

Acrivos, A., Fan, X., and Mauri, R. (1994). On the measurement of the relative viscosity of suspensions. *Journal of Rheology*, 38(5):1285.

Chang, C. and Powell, R. L. (1994). Effect of particle size distributions on the rheology of concentrated bimodal suspensions. *Journal of Rheology*, 38(1):85.

Chang, C., Smith, P. A., and Tracey, E. M. (1996). Rheological characterization of hanford neutralized current acid waste simulant slurries. *Journal of Rheology*, 40(4):483.

Cheng, D. C. (1984). Further observations on the rheological behavior of dense suspensions. *Powder Technology*, 37:255.

Chong, J. S., Christiansen, E. B., and Baer, A. D. (1971). Rheology of concentrated suspensions. *Journal of Applied Polymer Science*, 15:2007.

Dealy, J. M. and Wissbrun, K. F. (1990). *Melt Rheology and its Role in Plastics Processing.* Van Nostran and Reinhold.

Doi, M. and Chen, D. (1989). Simulation of aggregating colloids in shear flow. *Journal of Chemical Physics*, 90(10):5271.

Dorgan, J. R., Gleiman, S. S., Quigley, S. F., et al. (1995). Investigation of polymer encapsulation as a means of mixed waste treatment. In *Environmental Restoration Proceedings.*

Einstein, A. (1956). *Investigations on the Theory of the Brownian Movement.* Dover.

Farris, R. J. (1968). Prediction of the viscosity of multimodal suspensions from unimodal viscosity data. *Transactions of the Society of Rheology*, 12(2):281.

Faulkner, D. L. and Schmidt, L. R. (1977). Glass bead-filled polypropylene part i: Rheological and mechanical properties. *Polymer Engineering and Science*, 17:657.

FIDAP (1993). *FIDAP v7.0.* Fluid Dynamics International, Evanston, Ill.

Frankel, N. A. and Acrivos, A. (1967). On the viscosity of a concentrated suspension of solid spheres. *Chemical Engineering Science*, 22:847.

Gorce, J.-N., Hellgeth, J. W., and Ward, T. C. (1993). Mechanical hysteresis of a polyether polyurethane thermoplastic elastomer. *Polymer Engineering and Science*, 33:1170.

Griffiths, D. V. and Smith, I. M. (1993). *Programming the Finite Element.* Wiley and Sons, New York, second edition.

Han, C. D. and Chuang, H.-S. (1985). Criteria for rheological compatibility of polymer blends. *Journal of Applied Polymer Science*, 30:4431.

Han, C. D. and Kim, J. K. (1993). On the use of time-temperature superposition in multicomponent/ mulitphase polymer systems. *Polymer*, 34(12):2533.

Han, C. D. and Yang, H.-H. (1987). Rheological behavior of blends of poly(methyl methacrylate) (pmma) and poly(acrylonitrile-stat-styrene)-graft-polybutadiene (abs). *Journal of Applied Polymer Science*, 33:1221.

Jarzabski, G. J. (1981). On the effective viscosity of pseudoplastic suspensions. *Rheologica Acta*, 20:280.

Kataoka, T., Kitano, T., Sasahara, M., and Nishijima, K. (1978). Viscosity of particle filled polymer melts. *Rheologica Acta*, 17:149.

Kitano, T., Kataoka, T., and Nagatsuka, Y. (1984). Dynamic flow properties of vinylon fibre and glass fiber reinforced polyethylene melts. *Rheologica Acta*, 23:408.

Kitano, T., Kataoka, T., and Shirota, T. (1981). An emperical equation of the relative viscosity of polymer melts filled with various inorganic fillers. *Rheologica Acta*, 20:207.

Li, L. and Masuda, T. (1990). Effect of dispersion of particles on viscoelasticity of caco3- filled polypropylene melts. *Polymer Engineering and Science*, 30:841.

Lobe, V. and White, J. L. (1979). An experimental study of the influence of carbon black on the rheological properties of a polystyrene melt. *Polymer Engineering and Science*, 19:617. Issue 9.

Mamunya, E. P., Shumskii, V. F., and Lebedev, E. V. (1994). Rheologial properties and electrical conductivity of carbon black-filled polyethylene and polypropylene. *Polymer Science, Section B*, 36:835. Issue 6.

Matsumoto, T., Takashima, A., Masuda, T., and Onogi, S. (1970). A modified casson equation for dispersions. *Transactions of the Society of Rheology*, 14(4):617.

Metzner, A. B. (1985). Rheology of suspensions in polymeric liquids. *Journal of Rheology*, 29(6):739.

Mewis, J. and Spaull, A. J. B. (1976). Rheology of concentrated dispersions. *Advances in Colloid and Interface Science*, 6:173.

Mills, N. J. (1971). The rheology of filled polymers. *Journal of Applied Polymer Science*, 15:2791.

Nicodemo, L. and Nicolais, L. (1974). Viscosity of bead suspensions in polymeric solutions. *Journal of Applied Polymer Science*, 18:2809.

Nielsen, L. E. and Landel, R. F. (1994). *Mechanical Properties of Polymers and Composites.* Marcel Decker, second edition.

Ottani, S., Valenza, A., and Mantia, F. P. L. (1988). Shear characterization of caco3-filled linear low density polyethylene. *Rheologica Acta*, 27:172.

Park, M., Gandhi, K., Sun, L., Salovey, R., and Aklonis, J. J. (1990). Model-filled polymers. iii: Rheological behavior of polystyrene containing cross-linked polystyrene beads. *Polymer Engineering and Science*, 30(18):1158.

Phillips, R. J., Armstrong, R. C., Brown, R. A., Graham, A. L., and Abbott, J. R. (1992). A constitutive equation for concentrated suspensions that accounts for shear induced particle migration. *Physics of Fluids A*, 4(1):30.

Poslinski, A. J., Ryan, M. E., Gupta, R. K., Seshadri, S. G., and Frechette, F. J. (1988). Rheological behavior of filled polymeric systems i. yield stress and shear thinning effects. *Journal of Rheology*, 32(7):703.

Raghavan, S. R. and Kahn, S. A. (1995). Shear induced microstructural changes in flocculated suspensions of fumed silica. *Journal of Rheology*, 39(6):1311.

Reddy, J. N. (1993). *An Inroduction to the Finite Element Method.* McGraw-Hill, New York, second edition.

Rheometrics (1990). Understanding thermoplastics testing of thermoplastics.

Sastrohartono, T., Esseghir, M., Kwon, T. H., and Ernas, V. (1990). Numerical and experimental studies of the flow in the nip region of a partially intermeshing co-rotating twin-screw extruder. *Polymer Engineering and Science*, 30(12):1382.

Sastrohartono, T., Jaluria, Y., and Karwe, M. V. (1994). Numerical coupling of multiple-region simulations to study transport in a twin-screw extruder. *Numerical Heat Transfer, Part A*, 25:541.

Sastrohartono, T. and Kwon, T. H. (1990). Finite element analysis of mixing phenomena in tangential twin-screw extruders for non-newtonian fluids. *International Journal for Numerical Methods in Engineering*, 30:1369.

Sergé, G. and Silberberg, A. (1962). Behavior of macroscopic rigid spheres in poiseuille flow. *Journal of Fluid Mechanics*, 14:115.

Suetsugu, Y. and White, J. L. (1983). The influence of particle size and surface coating of calcium carbonate on the rheological properties of its suspensions in molten polystyrene. *Journal of Applied Polymer Science*, 28:1481.

Sundstrom, D. W. (1983). Viscosity of suspensions in polymeric solutions. *Rheologica Acta*, 22:420.

Tanaka, H. and White, J. L. (1980a). A cell model theory of the shear viscosity of a concentrated suspension on interacting spheres in a non-newtonain fluid. *Journal of Non-Newtonian Fluid Mechanics*, 7:333.

Tanaka, H. and White, J. L. (1980b). Experimental investigations of shear and elongational flow properties of polystyrene melts reinforced with calcium carbonate, titanium dioxide, and carbon black. *Polymer Engineering and Science*, 20:949. Issue 14.

Tsai, S. C., Botts, D., and Plouff, J. (1992). effects of particle properties on the rheology of concentrated noncolloidal suspensions. *Journal of Rheology*, 36:1291. Issue 7.

Tsiprin, M. G., Irgen, L. A., and Lappo, V. A. (1992). Rheological and technological characteristics of polyethylene melts filled with chalk and ground limestone. *Translated from Mekhanika Kompozitnykh Materialov*, 6:829.

Tsutsumi, A., Yoshida, K., Yui, M., Kanamori, S., and Shibata, K. (1994). Shear viscosity behavior of flocculated suspensions. *Powder Technology*, 78:165.

Wildemuth, C. R. and Williams, M. C. (1984). Viscosity of suspensions modeled with a shear-dependent maximum packing fraction. *Rheologica Acta*, 23:627.

Appendix A

ERROR ANALYSIS

This appendix outlines the procedure for calculating errors in the stress dependent maximum packing fraction.

The total error can be calculated as the variance in $\left(\frac{\eta_r^{1/2}-1}{\phi}\right)$, taken as the total derivative of $\left(\frac{\eta_r^{1/2}-1}{\phi}\right)$ with respect to the variables η_r and ϕ.

$$\delta\left(\frac{\eta_r^{1/2}-1}{\phi}\right) = \frac{\partial}{\partial\eta_r}\left(\frac{\eta_r^{1/2}-1}{\phi}\right)\delta\eta_r + \frac{\partial}{\partial\phi}\left(\frac{\eta_r^{1/2}-1}{\phi}\right)\delta\phi \tag{A.1}$$

$$= \left(\frac{1}{2\phi\eta_r^{1/2}}\right)\delta\eta_r + \left(\frac{\eta_r^{1/2}-1}{\phi^2}\right)\delta\phi \tag{A.2}$$

To calculate the variance in relative viscosity $\delta\eta_r$, the total derivative is taken with respect to the variables defined in Equation A.3.

$$\eta_r = \frac{\eta_s}{\eta_m} \tag{A.3}$$

$$\delta\eta_r = \frac{\partial}{\partial\eta_m}\left(\frac{\eta_s}{\eta_m}\right)\delta\eta_m + \frac{\partial}{\partial\eta_s}\left(\frac{\eta_s}{\eta_m}\right)\delta\eta_s \tag{A.4}$$

$$= \left(\frac{\eta_s}{\eta_m^2}\right)\delta\eta_m + \left(\frac{1}{\eta_m}\right)\delta\eta_s \tag{A.5}$$

The filler volume fraction also has error associated with it. This can be calculated via the definition in Equation A.6.

$$\phi = \frac{m_{filler}\left(\frac{\rho_{polymer}}{\rho_{filler}}\right)}{m_{filler}\left(\frac{\rho_{polymer}}{\rho_{filler}}\right) + m_{polymer}} \tag{A.6}$$

$$\delta\phi = \frac{\partial}{\partial m_{filler}}\left(\frac{m_{filler}\left(\frac{\rho_{polymer}}{\rho_{filler}}\right)}{m_{filler}\left(\frac{\rho_{polymer}}{\rho_{filler}}\right)+m_{polymer}}\right)\delta m_{filler} + \frac{\partial}{\partial m_{polymer}}\left(\frac{m_{filler}\left(\frac{\rho_{polymer}}{\rho_{filler}}\right)}{m_{filler}\left(\frac{\rho_{polymer}}{\rho_{filler}}\right)+m_{polymer}}\right)\delta m_{polymer} \quad \text{(A.7)}$$

$$\delta\phi = \left[-\frac{m_{filler}\left(\frac{\rho_{polymer}}{\rho_{filler}}\right)}{\left(m_{filler}\left(\frac{\rho_{polymer}}{\rho_{filler}}\right)+m_{polymer}\right)^2}+\frac{\left(\frac{\rho_{polymer}}{\rho_{filler}}\right)}{\left(m_{filler}\left(\frac{\rho_{polymer}}{\rho_{filler}}\right)+m_{polymer}\right)}\right]\delta m_{filler} + \left[\frac{m_{filler}\left(\frac{\rho_{polymer}}{\rho_{filler}}\right)}{\left(m_{filler}\left(\frac{\rho_{polymer}}{\rho_{filler}}\right)+m_{polymer}\right)^2}\right]\delta m_{polymer} \quad \text{(A.8)}$$

An order of magnitude analysis of rheometer precision gives a loading level-dependent value of $\delta\eta_r$ shown in Table A.

A similar order of magnitude analysis is used to calculate $\delta\phi$. In this, values of δm_{filler} and $\delta m_{polymer}$, the variances in the amount of filler and polymer in the samples, respectively, need to be known. These variables take into account surges in the loss-in-weight feeders associated with the extrusion process. It is assumed that the filler weight variance is at least an order of magnitude larger than the polymer weight variance. This is because of difficulties in filler feeding including clumping, bridging, and caking. From this approximation, $\delta\phi \approx$ 1.254E-03. Calculation of the total error, and hence the slope and intercept errors, can now be completed.

Filler Loading (wt%)	$\delta\eta_r$ (-)
50	6.75E-03
37.5	2.00E-03
25	1.33E-03
12.5	1.18E-03

Table A.1: Calculated values of filler loading-dependent relative viscosity variance.

The following data in Figures A.1-A.20 was used to calculate the filler density, and hence the correct stress and thermal dependent maximum packing fraction. The data is compiled in Table 4.3 on page 47. The data in Figures A.21-A.34 represent calculation of ϕ_m at ρ_{filler}=1.75 g/cm^3. This data allows reduction based on stress level and temperature such that $\phi_m = \phi_m(\tau, \mathrm{T})$.

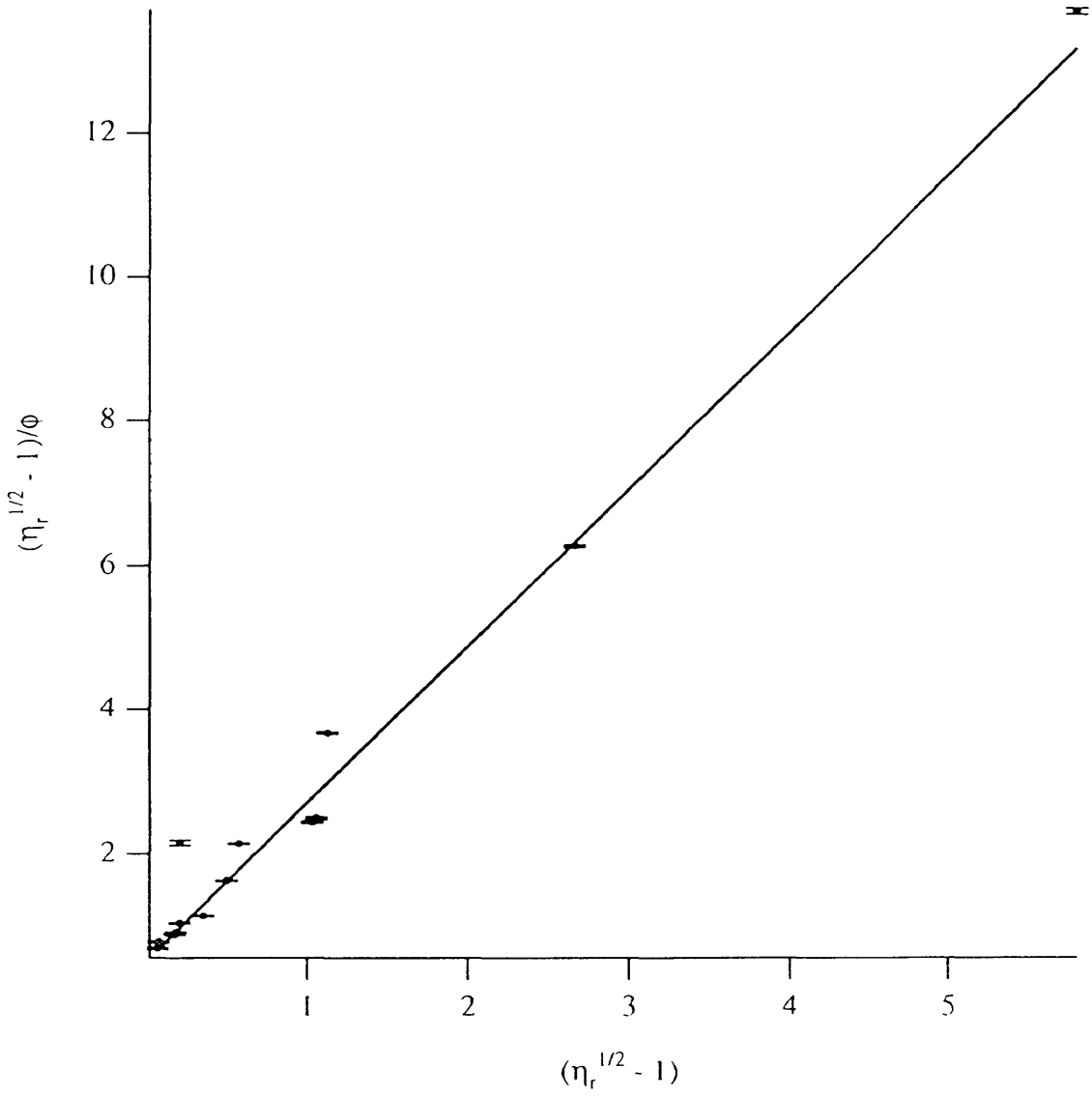

Figure A.1: $(\eta_r^{1/2} - 1)/\phi$ versus $(\eta_r^{1/2} - 1)$. ρ_{filler} = 1.25 g/cm^3; τ = 1.60E+04 dyne/cm^2. ϕ_m=0.460±0.001, [η]=1.051±7.88E-03.

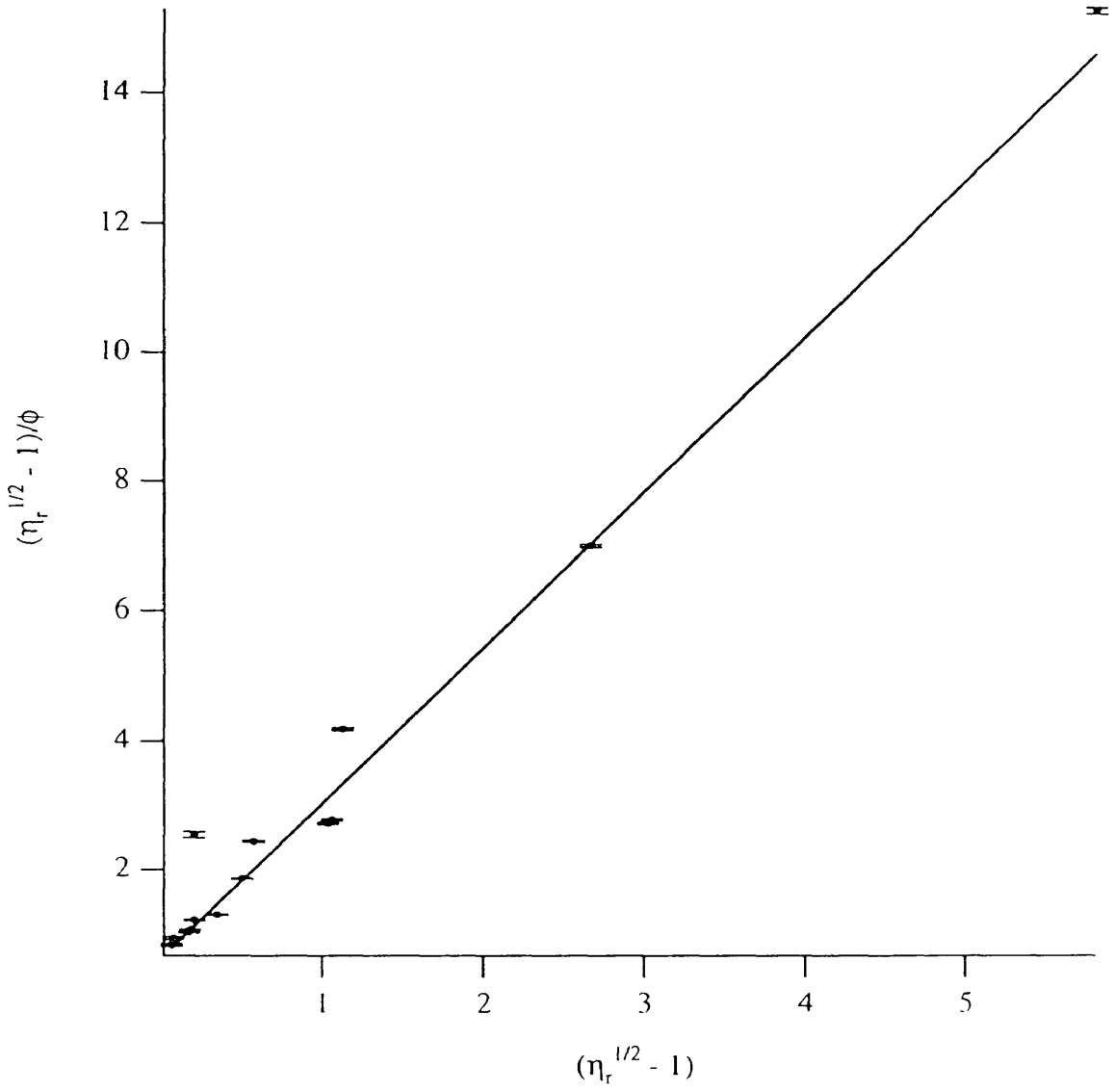

Figure A.2: $(\eta_r^{1/2} - 1)/\phi$ versus $(\eta_r^{1/2} - 1)$. ρ_{filler} = 1.50 g/cm^3; τ = 1.60E+04 dyne/cm^2. ϕ_m=0.471±0.001, $[\eta]$=1.243±0.010.

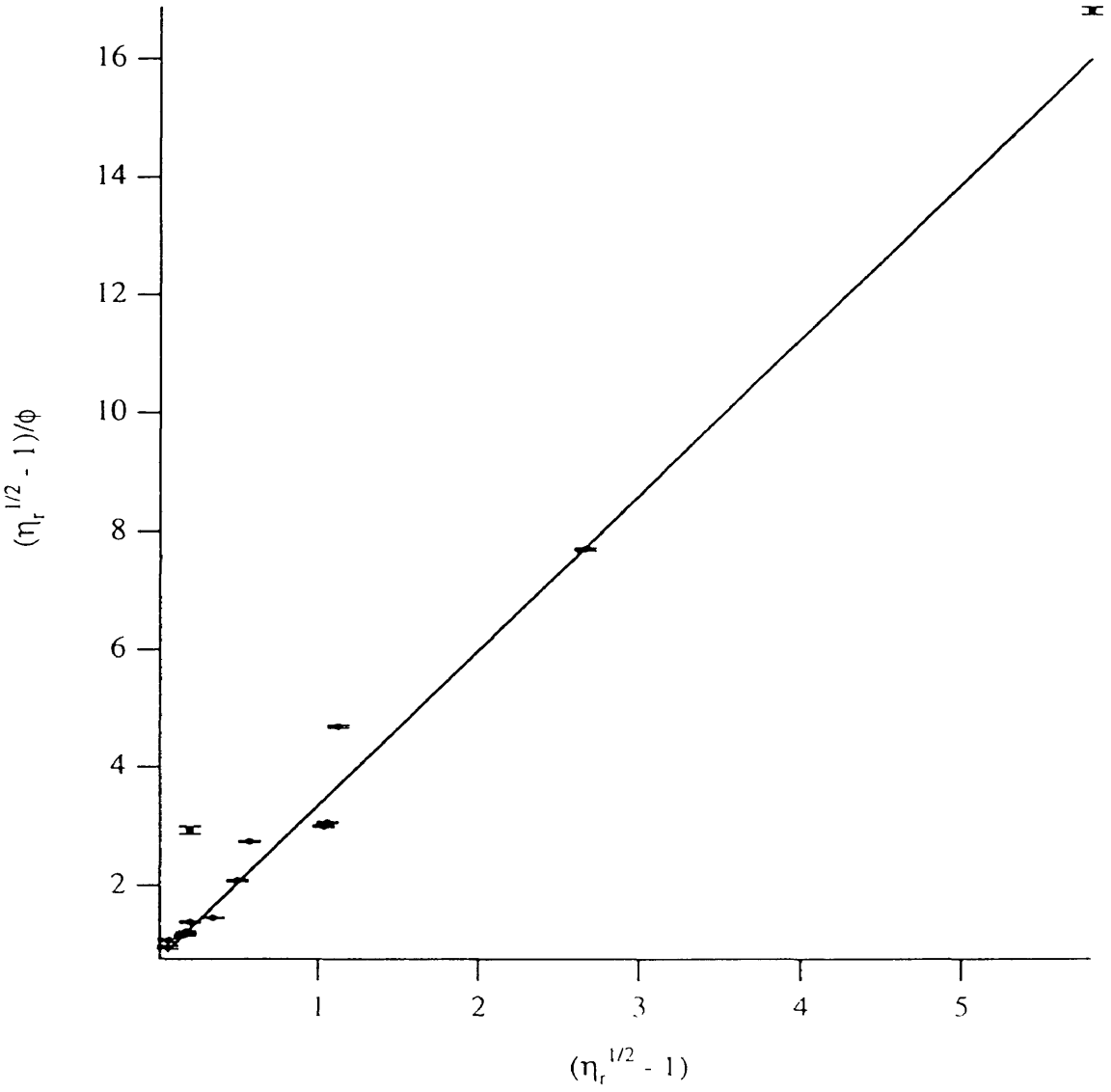

Figure A.3: $(\eta_r^{1/2} - 1)/\phi$ versus $(\eta_r^{1/2} - 1)$. ρ_{filler} = 1.75 g/cm^3; τ = 1.60E+04 dyne/cm^2. ϕ_m=0.381±0.001, $[\eta]$=1.434±0.012.

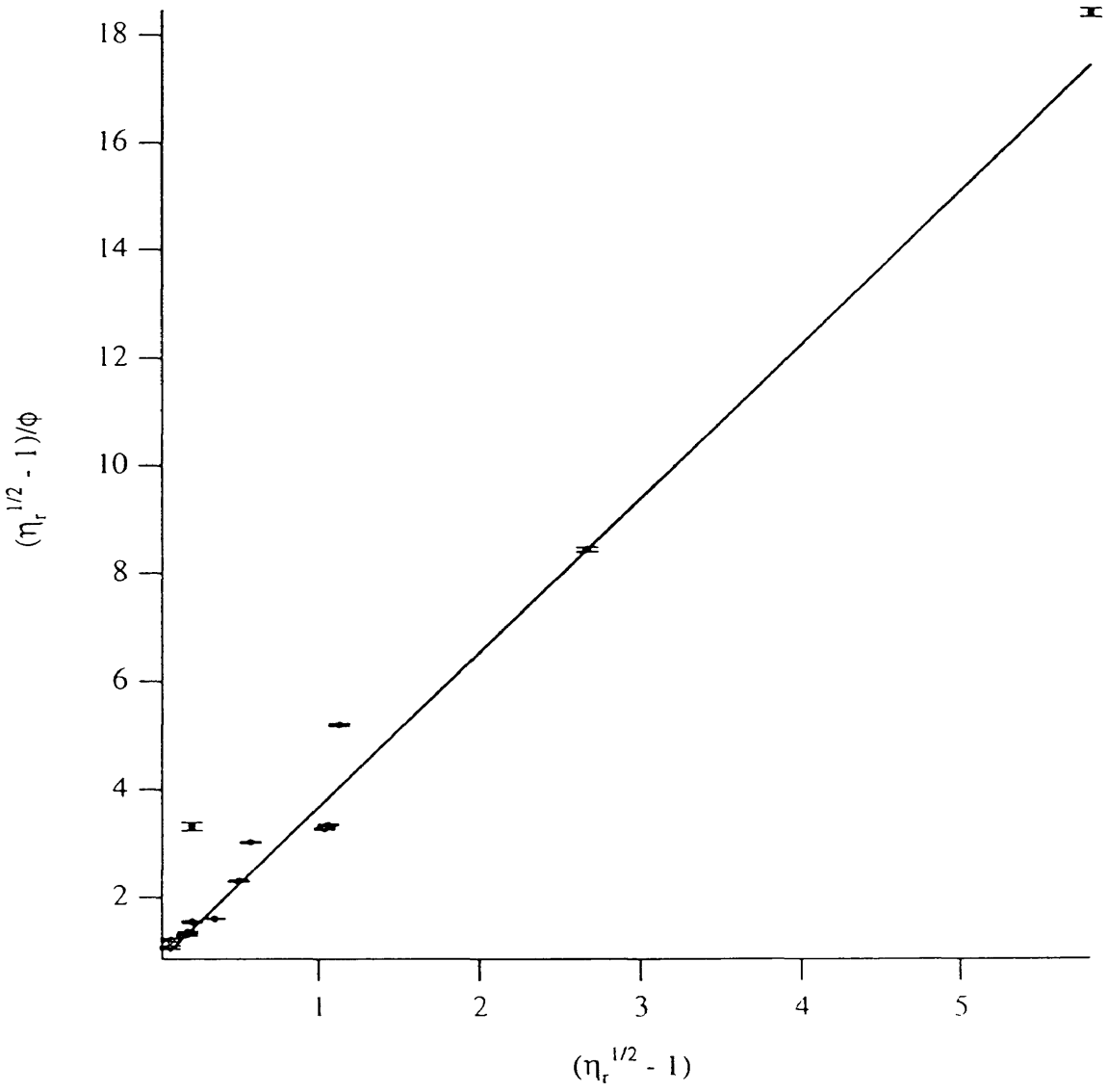

Figure A.4: $(\eta_r^{1/2} - 1)/\phi$ versus $(\eta_r^{1/2} - 1)$. ρ_{filler} = 2.00 g/cm^3; τ = 1.60E+04 dyne/cm^2. ϕ_m=0.350±0.001, $[\eta]$=1.623±0.015.

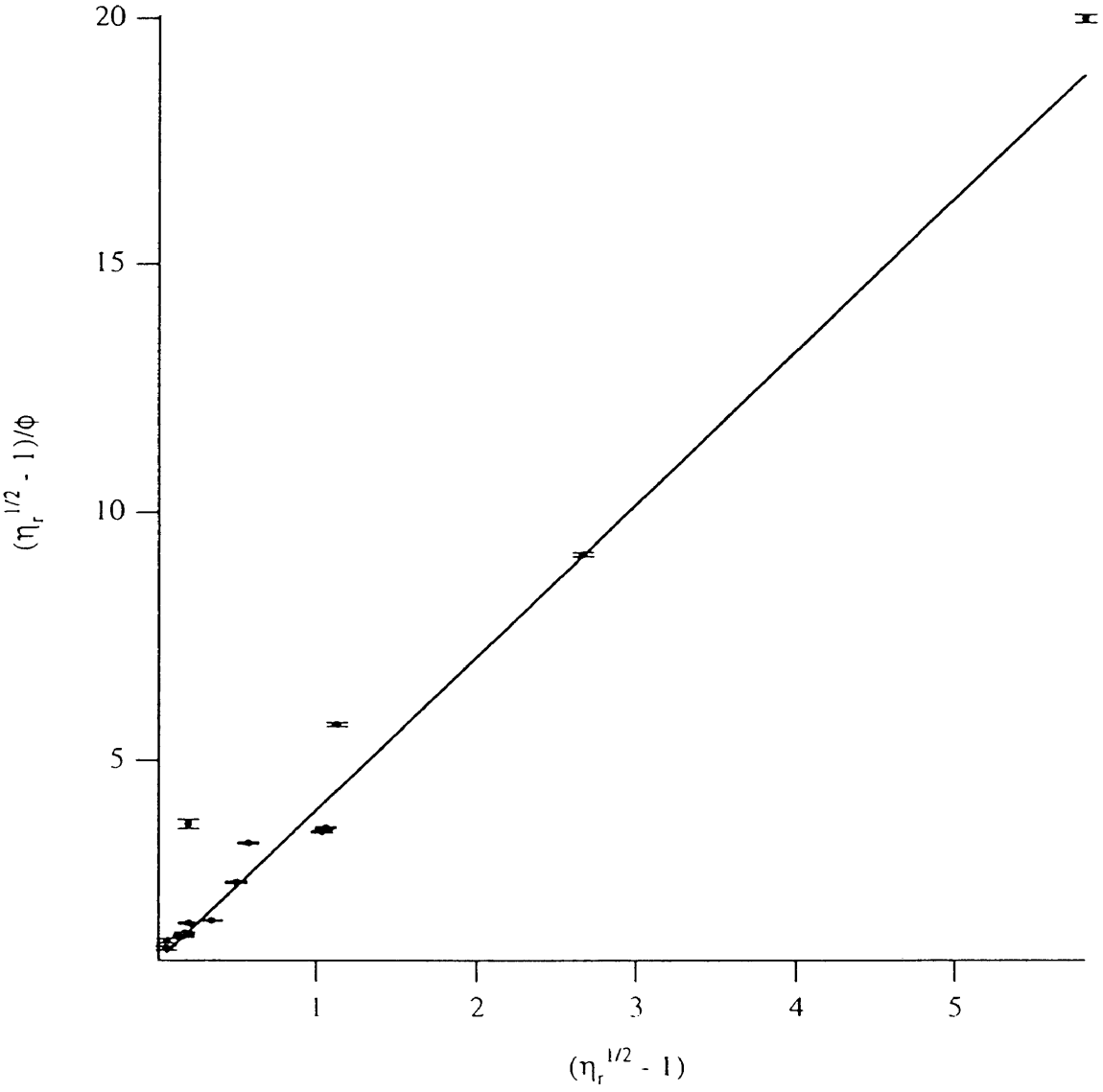

Figure A.5: $(\eta_r^{1/2} - 1)/\phi$ versus $(\eta_r^{1/2} - 1)$. ρ_{filler} = 2.25 g/cm^3; τ = 1.60E+04 dyne/cm^2. ϕ_m=0.325±0.001, $[\eta]$=1.817±0.018.

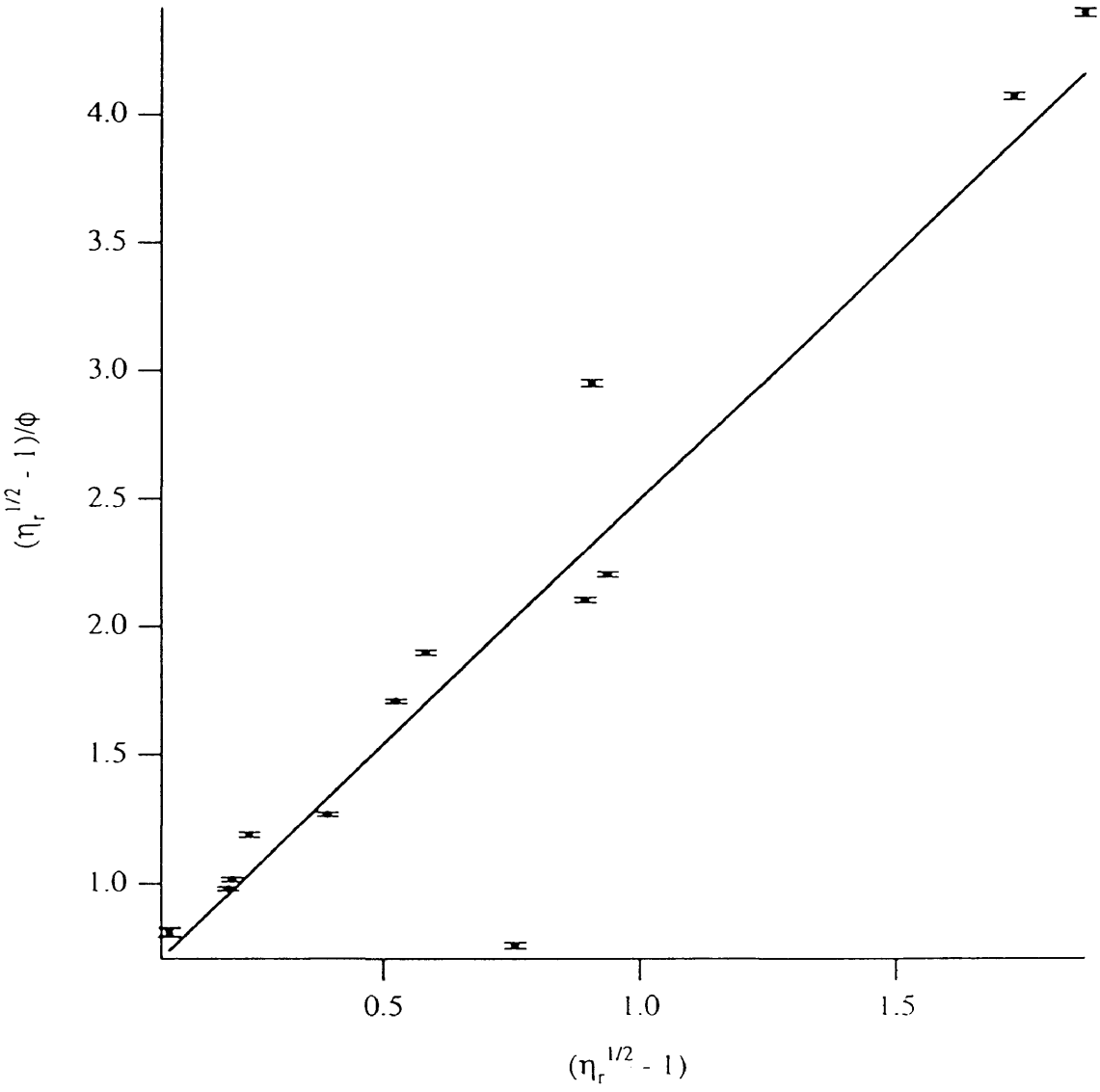

Figure A.6: $(\eta_r^{1/2} - 1)/\phi$ versus $(\eta_r^{1/2} - 1)$. $\rho_{filler} = 1.25$ g/cm^3; $\tau = 1.00$E+05 dyne/cm^2. ϕ_m=0.524±0.002, $[\eta]$=1.174±9.50E-03.

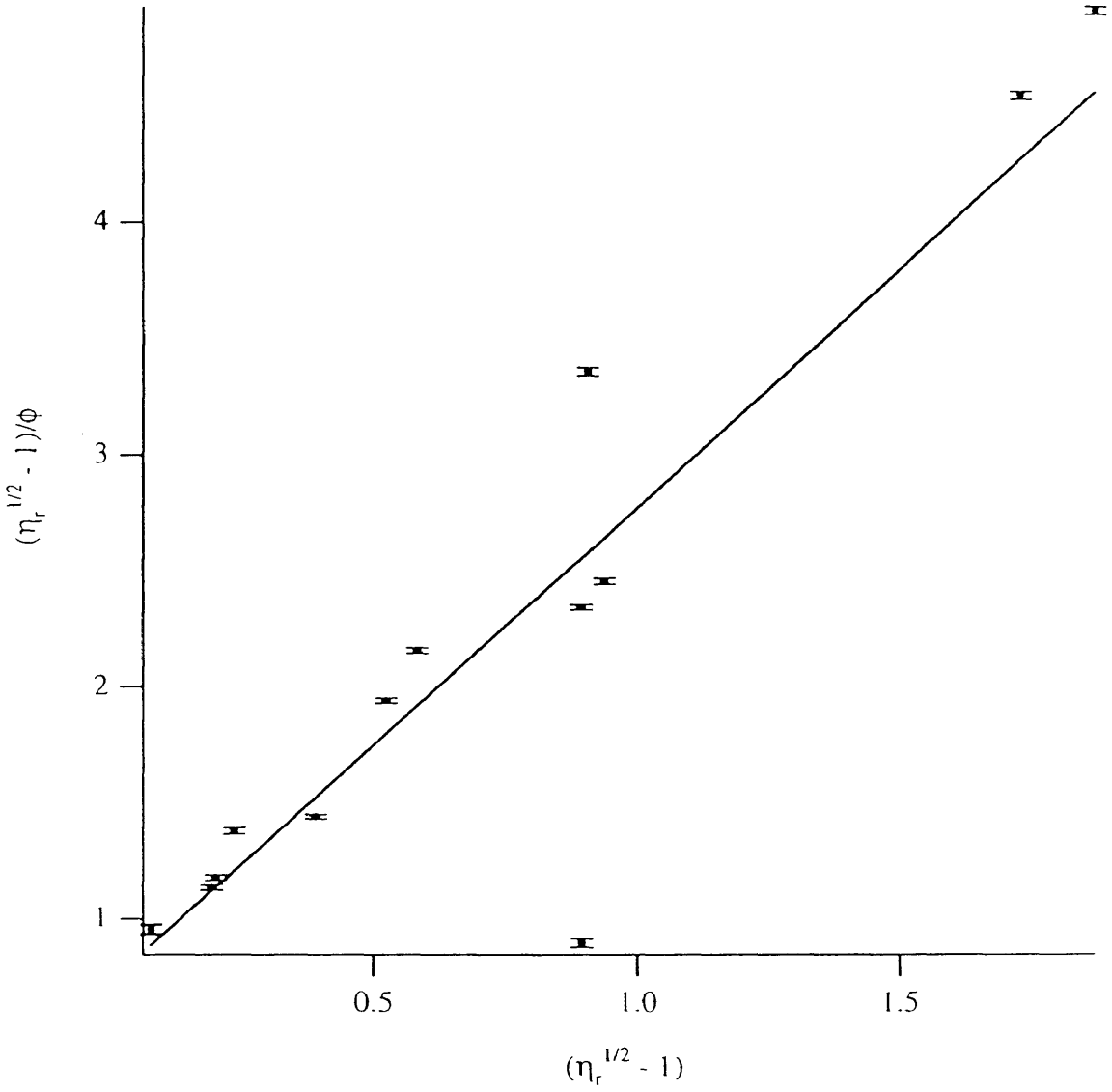

Figure A.7: $(\eta_r^{1/2} - 1)/\phi$ versus $(\eta_r^{1/2} - 1)$. ρ_{filler} = 1.50 g/cm^3; τ = 1.00E+05 dyne/cm^2. ϕ_m=0.489±0.002, $[\eta]$=1.452±0.012.

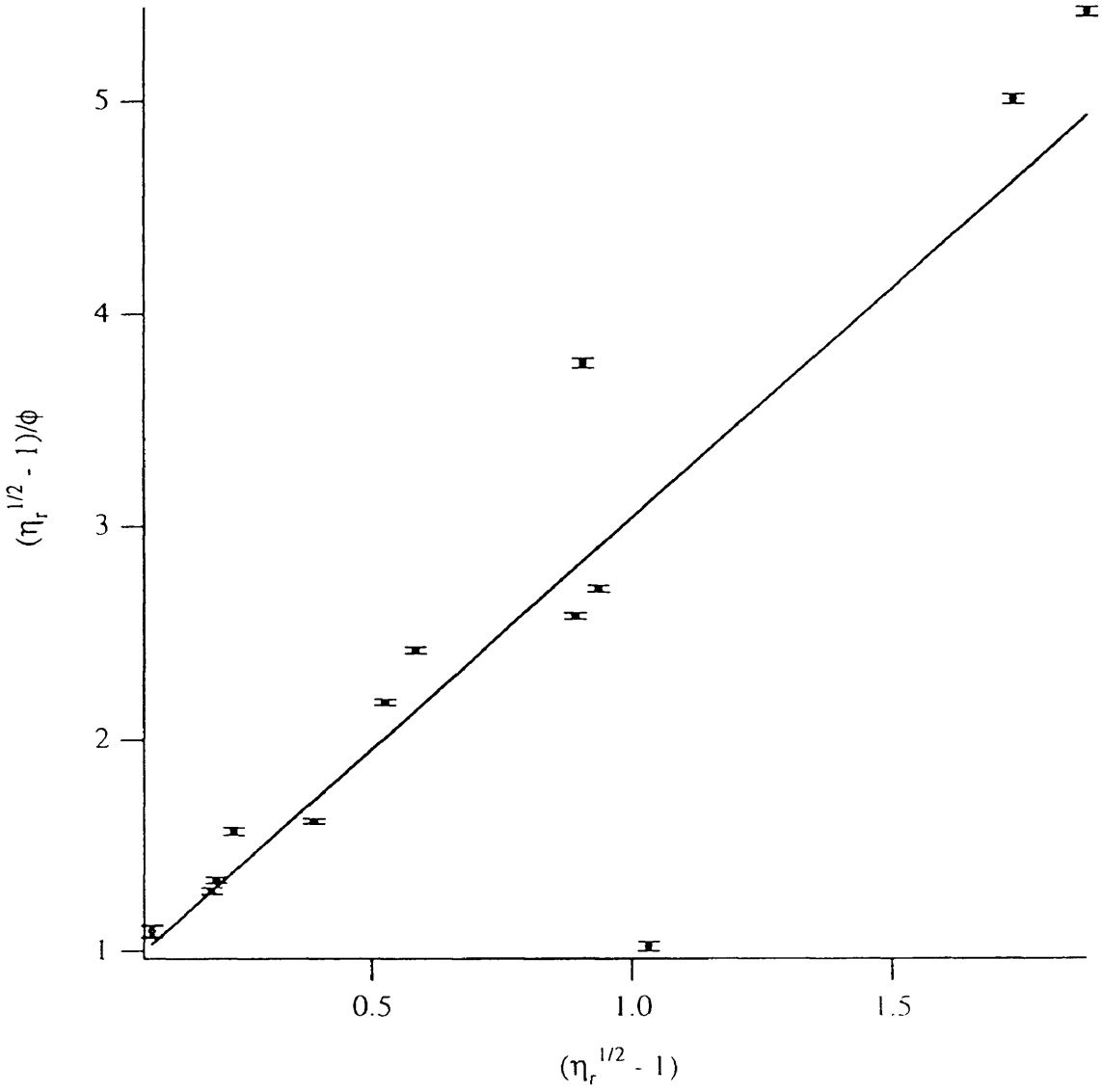

Figure A.8: $(\eta_r^{1/2} - 1)/\phi$ versus $(\eta_r^{1/2} - 1)$. $\rho_{filler} = 1.75$ g/cm^3; $\tau = 1.00$E+05 dyne/cm^2. ϕ_m=0.461±0.002, $[\eta]$=1.745±0.015.

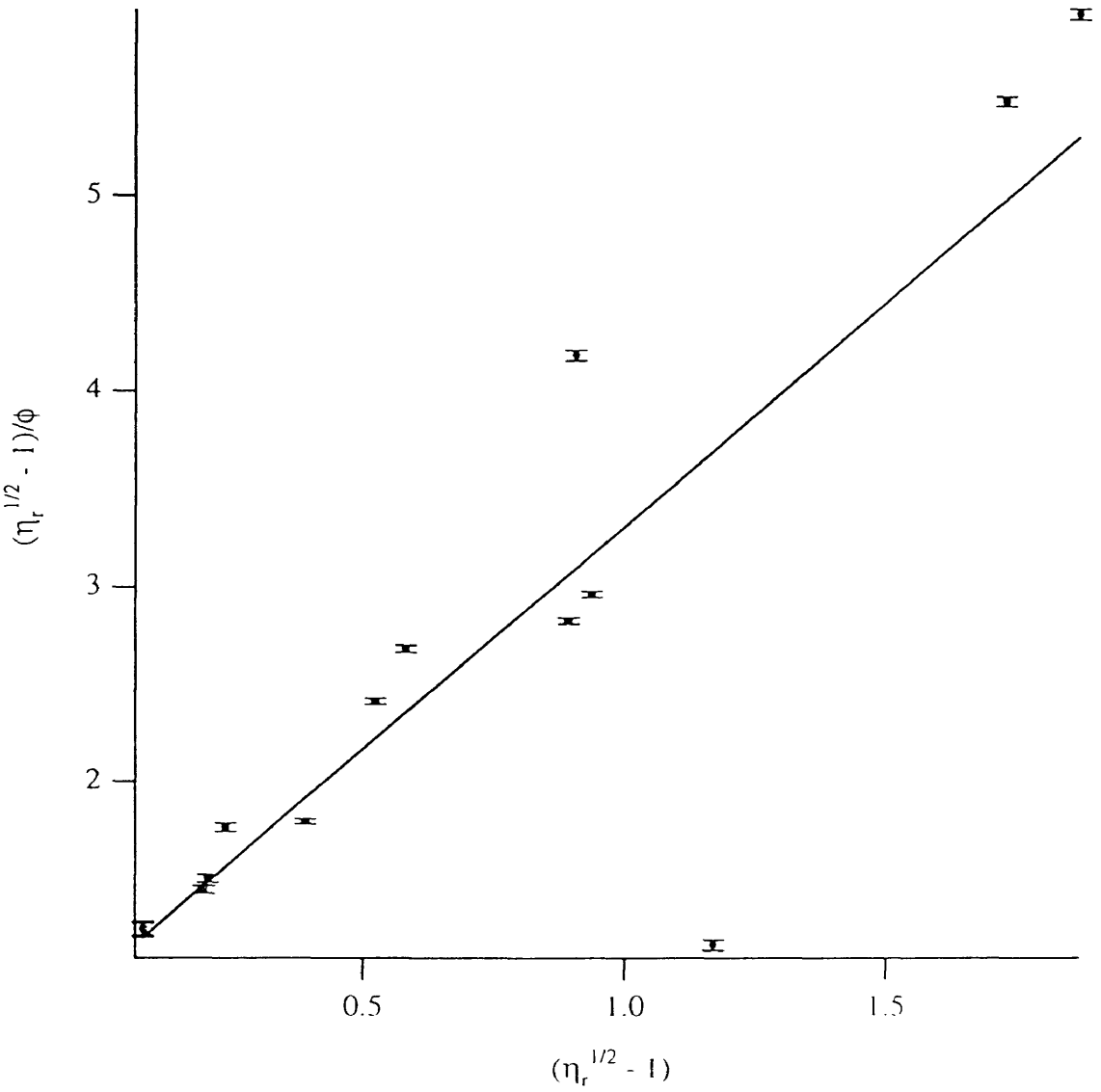

Figure A.9: $(\eta_r^{1/2} - 1)/\phi$ versus $(\eta_r^{1/2} - 1)$. ρ_{filler} = 2.00 g/cm^3; τ = 1.00E+05 dyne/cm^2. ϕ_m=0.439±0.002, $[\eta]$=2.056±0.018.

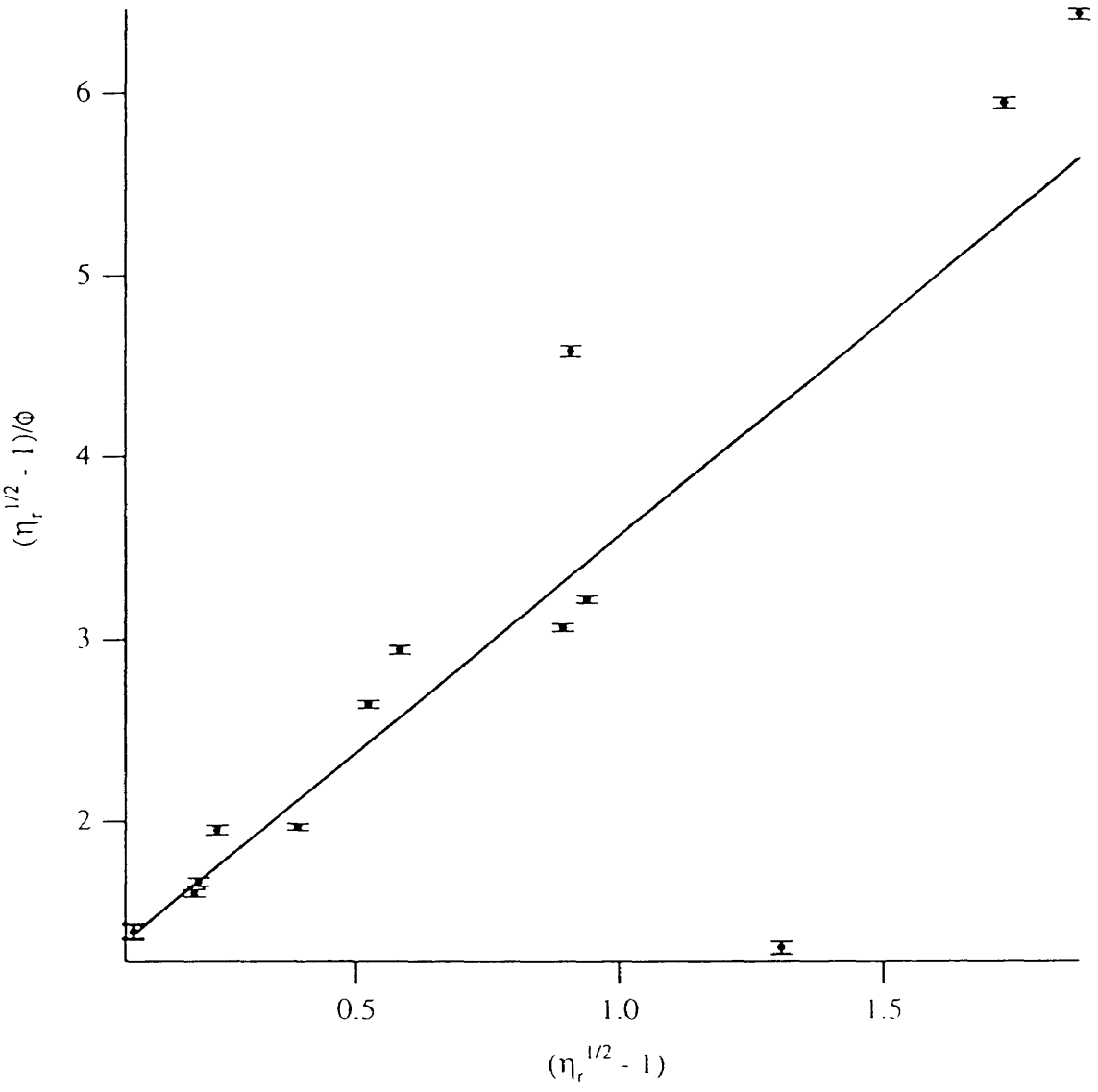

Figure A.10: $(\eta_r^{1/2} - 1)/\phi$ versus $(\eta_r^{1/2} - 1)$. $\rho_{filler} = 2.25$ g/cm^3; $\tau = 1.00$E+05 dyne/cm^2. ϕ_m=0.421±0.002, $[\eta]$=2.384±0.022.

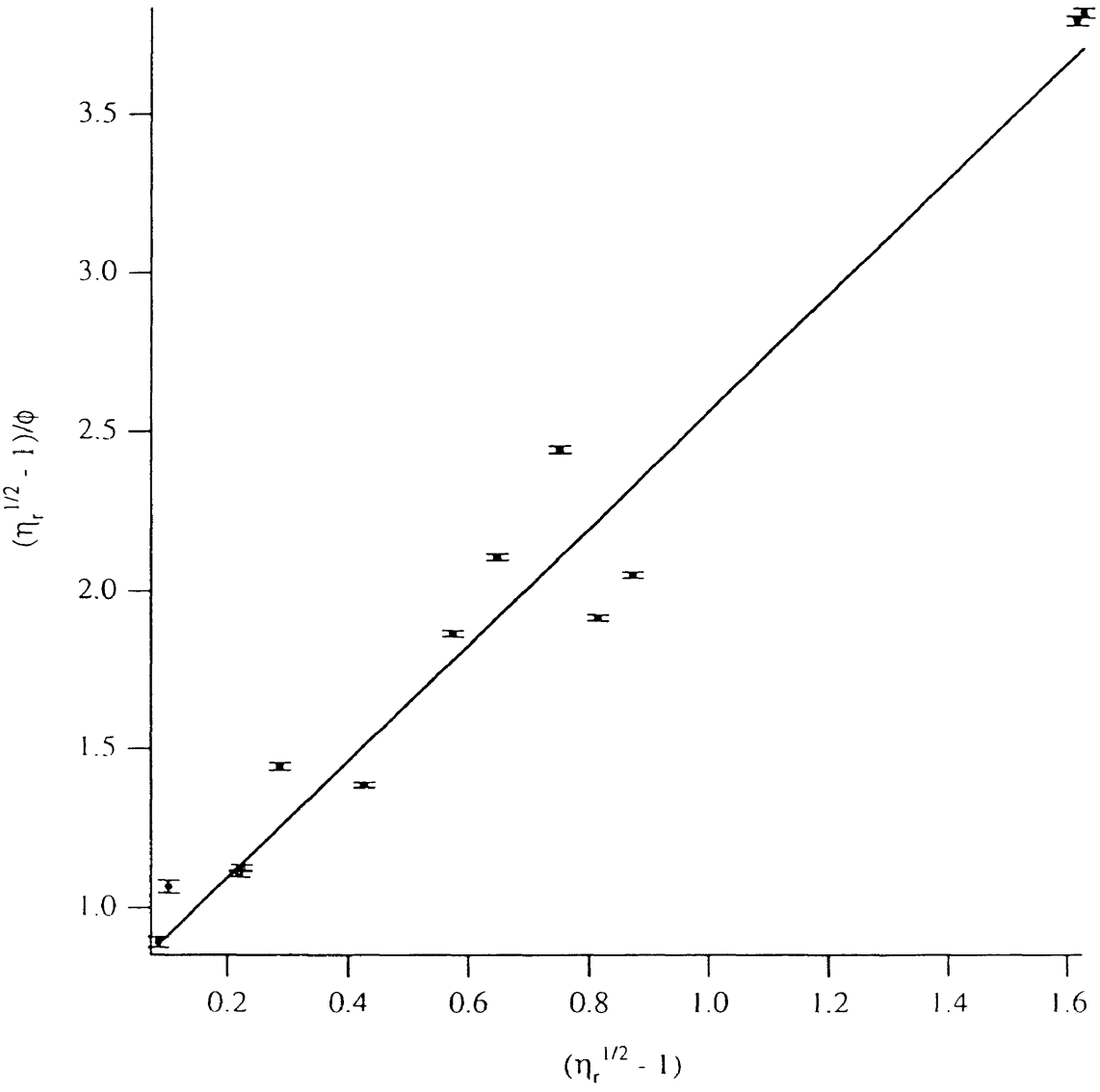

Figure A.11: $(\eta_r^{1/2} - 1)/\phi$ versus $(\eta_r^{1/2} - 1)$. ρ_{filler} = 1.25 g/cm^3; τ = 2.00E+05 dyne/cm^2. ϕ_m=0.545±0.002, $[\eta]$=1.455±0.011.

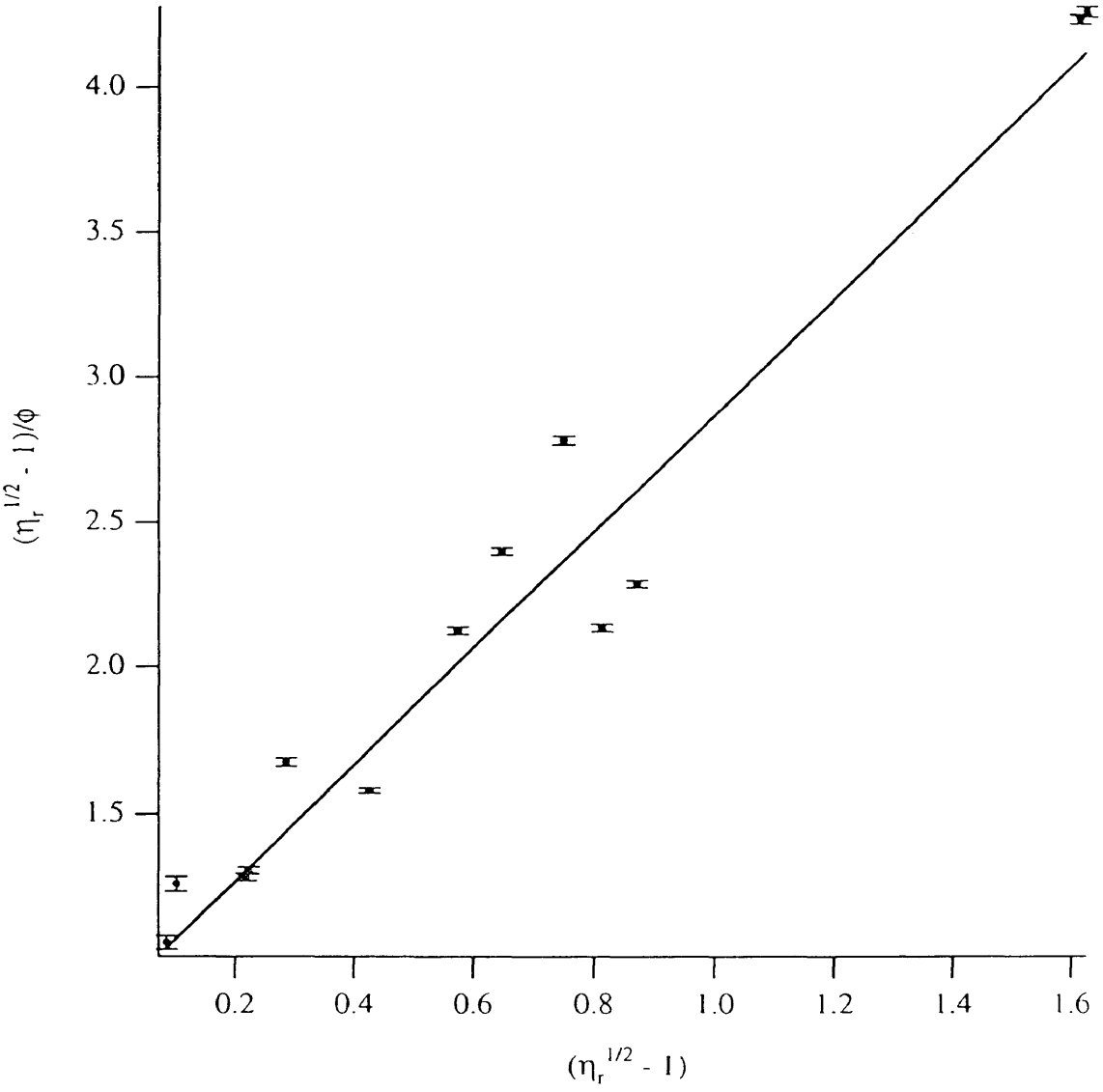

Figure A.12: $(\eta_r^{1/2} - 1)/\phi$ versus $(\eta_r^{1/2} - 1)$. $\rho_{filler} = 1.50$ g/cm^3; $\tau = 2.00$E+05 dyne/cm^2. ϕ_m=0.500±0.002, $[\eta]$=1.730±0.014.

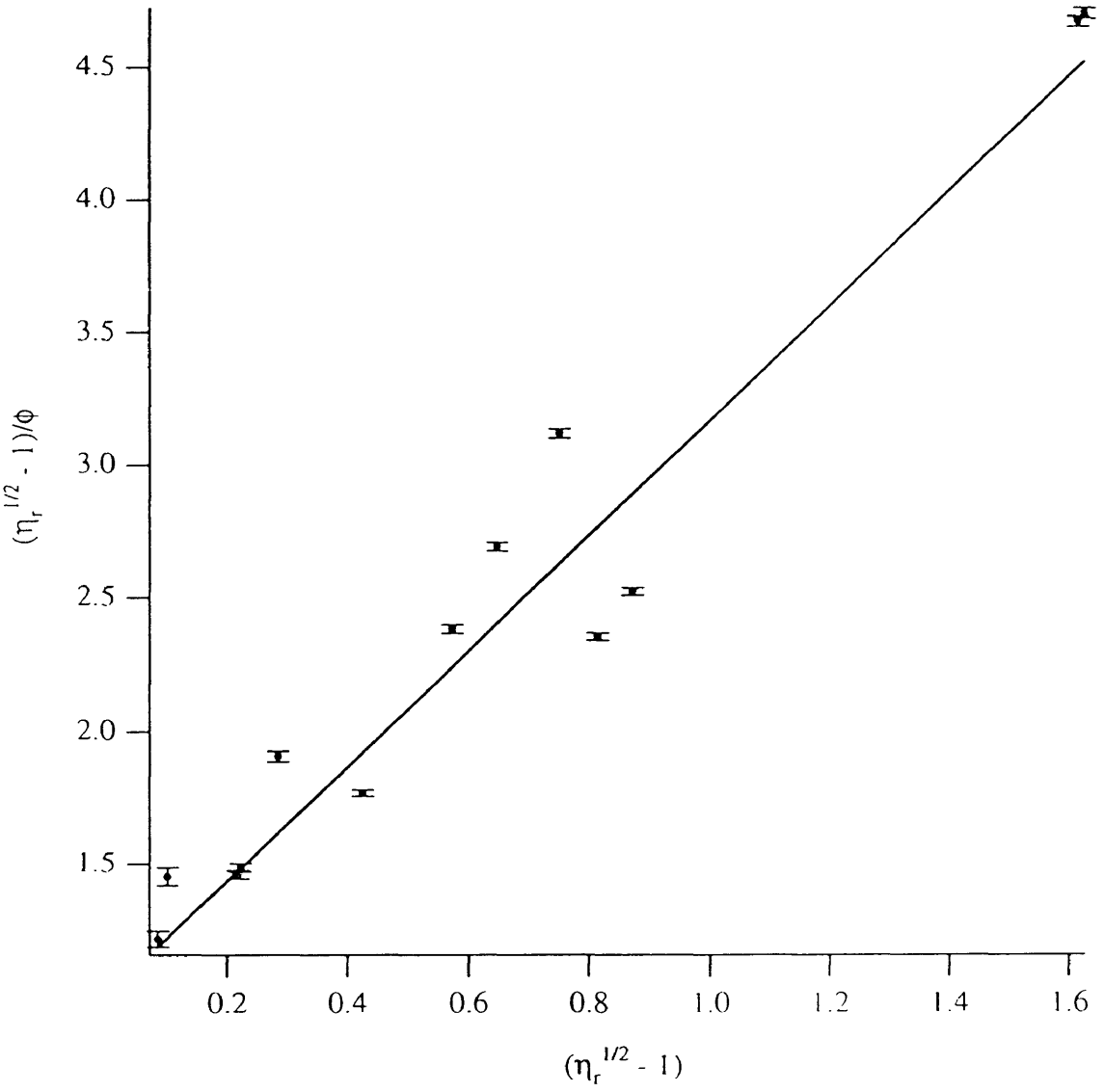

Figure A.13: $(\eta_r^{1/2} - 1)/\phi$ versus $(\eta_r^{1/2} - 1)$. ρ_{filler} = 1.75 g/cm^3; τ = 2.00E+05 dyne/cm^2. ϕ_m=0.462±0.002, $[\eta]$=2.000±0.017.

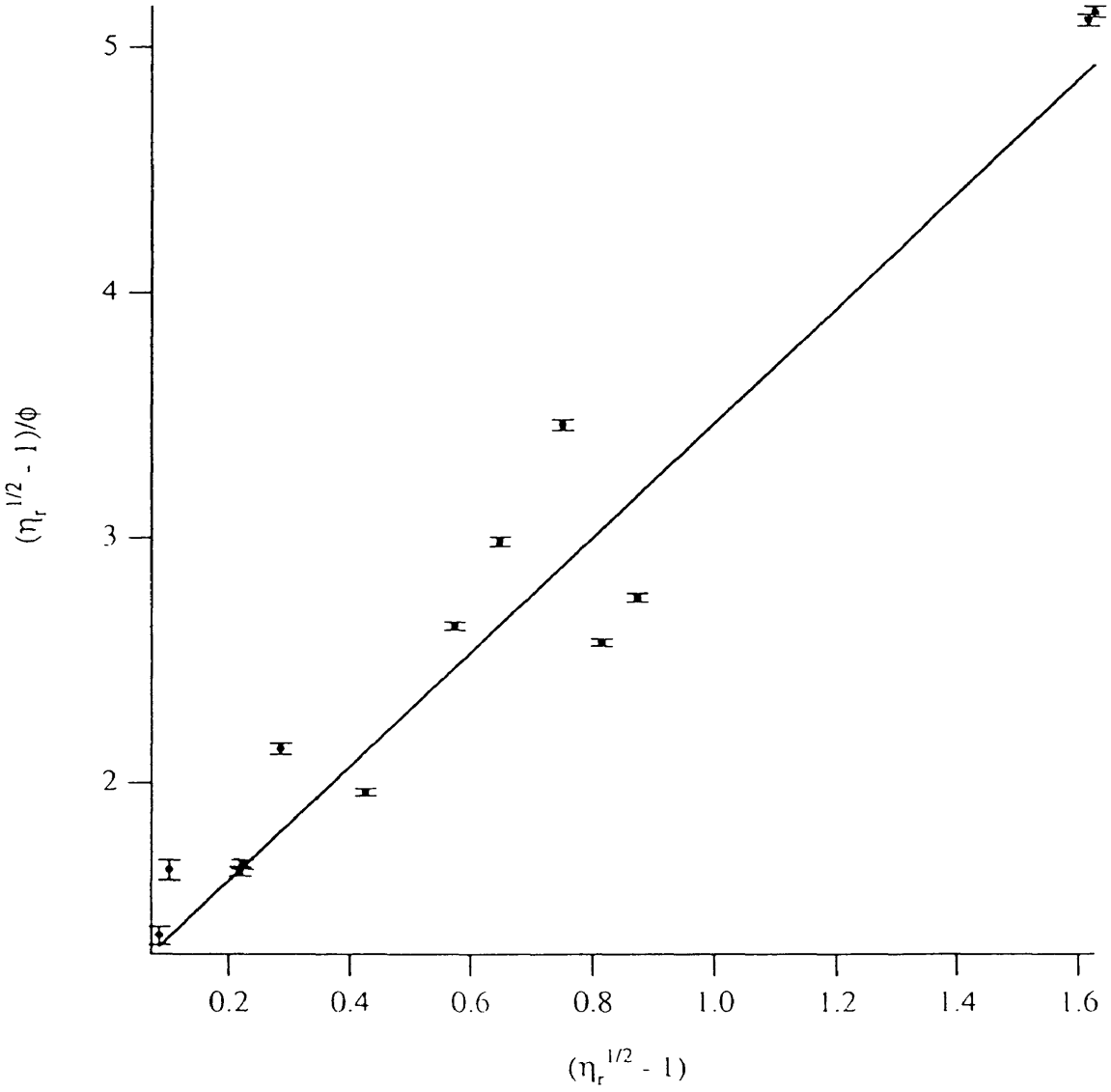

Figure A.14: $(\eta_r^{1/2} - 1)/\phi$ versus $(\eta_r^{1/2} - 1)$. ρ_{filler} = 2.00 g/cm^3; τ = 2.00E+05 dyne/cm^2. ϕ_m=0.429±0.003, $[\eta]$=2.267±0.021.

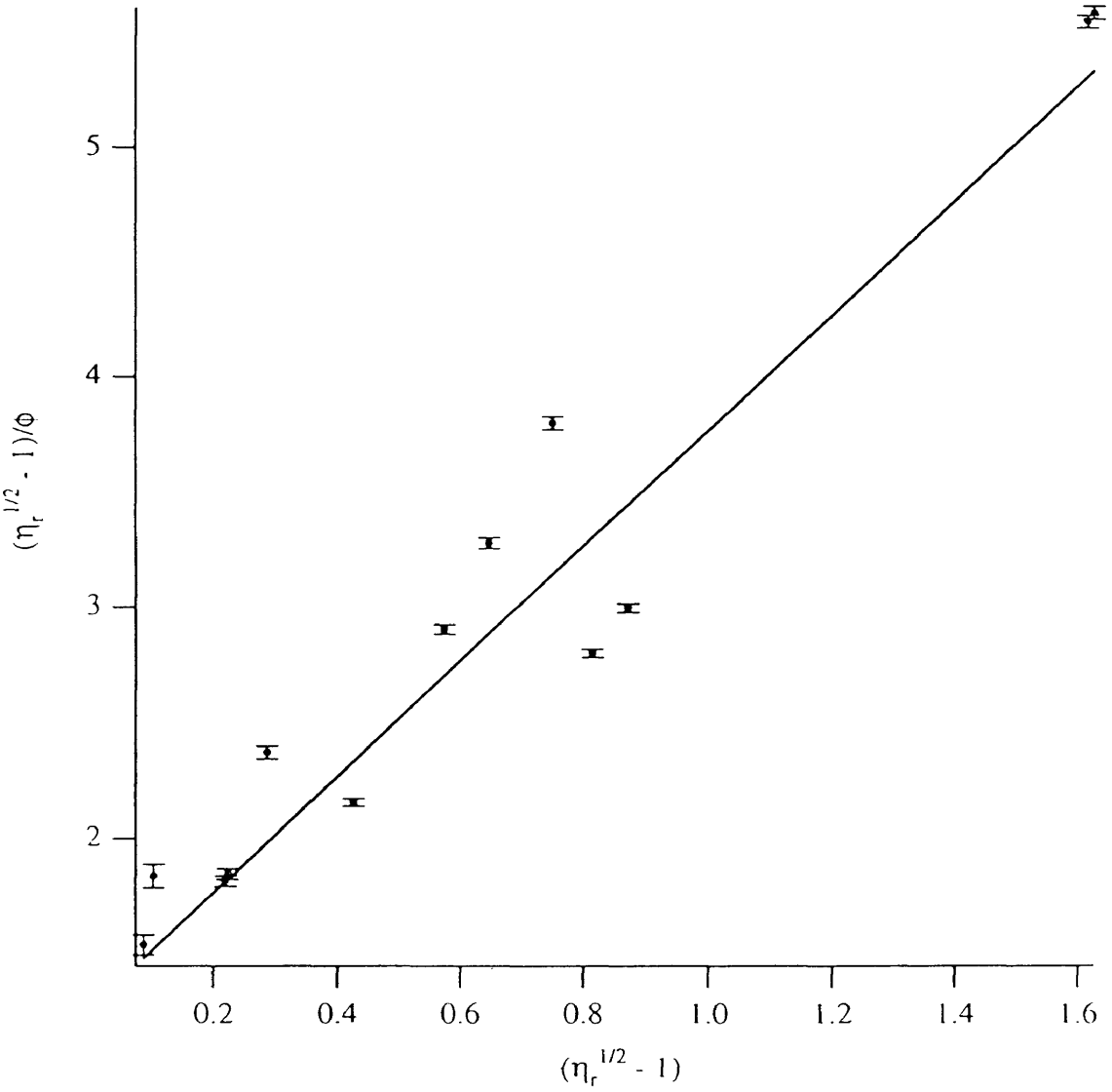

Figure A.15: $(\eta_r^{1/2} - 1)/\phi$ versus $(\eta_r^{1/2} - 1)$. ρ_{filler} = 2.25 g/cm^3; τ = 2.00E+05 dyne/cm^2. ϕ_m=0.400±0.003, $[\eta]$=2.531±0.025.

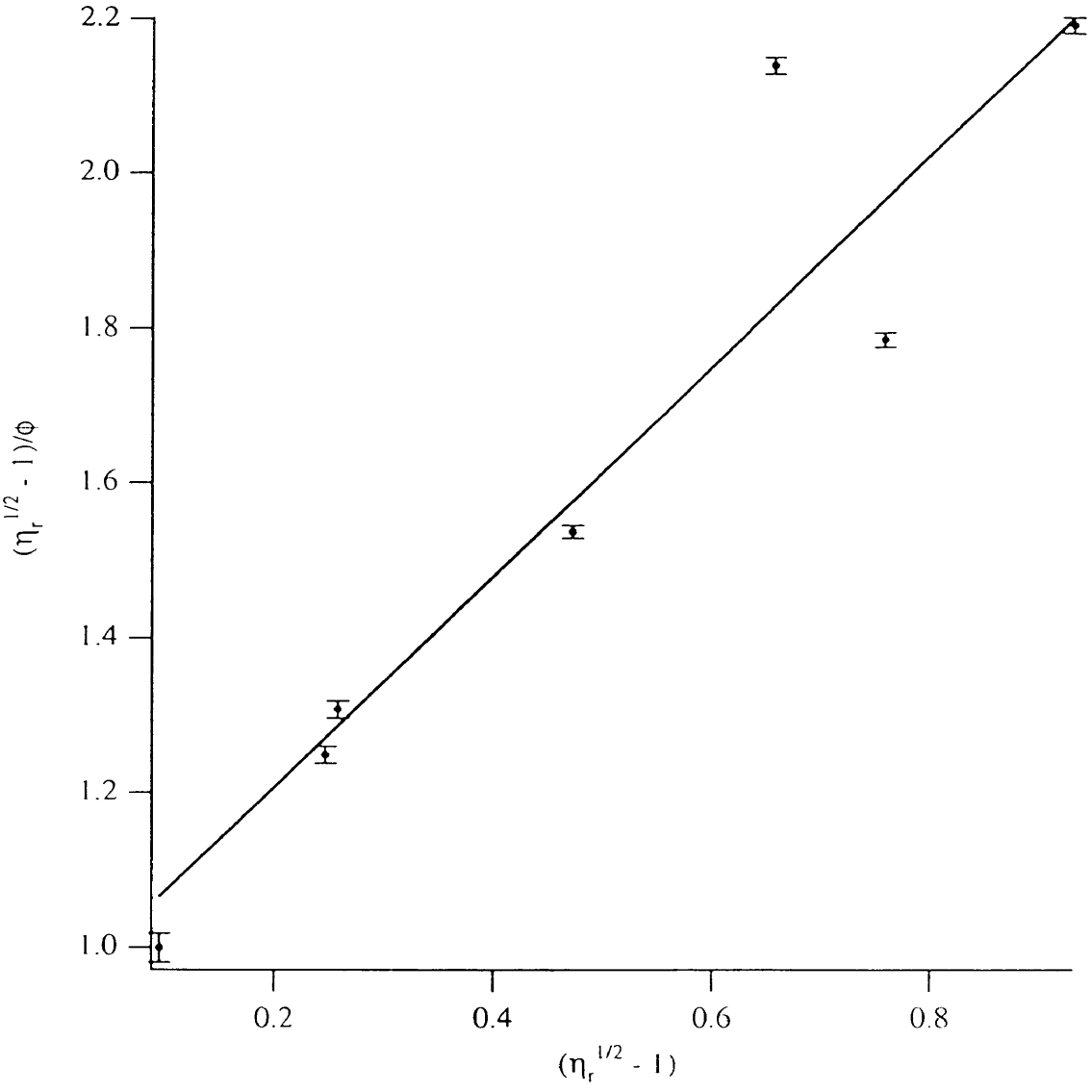

Figure A.16: $(\eta_r^{1/2} - 1)/\phi$ versus $(\eta_r^{1/2} - 1)$. ρ_{filler} = 1.25 g/cm^3; τ = 3.00E+05 dyne/cm^2. ϕ_m=0.736±0.009, $[\eta]$=1.870±0.019.

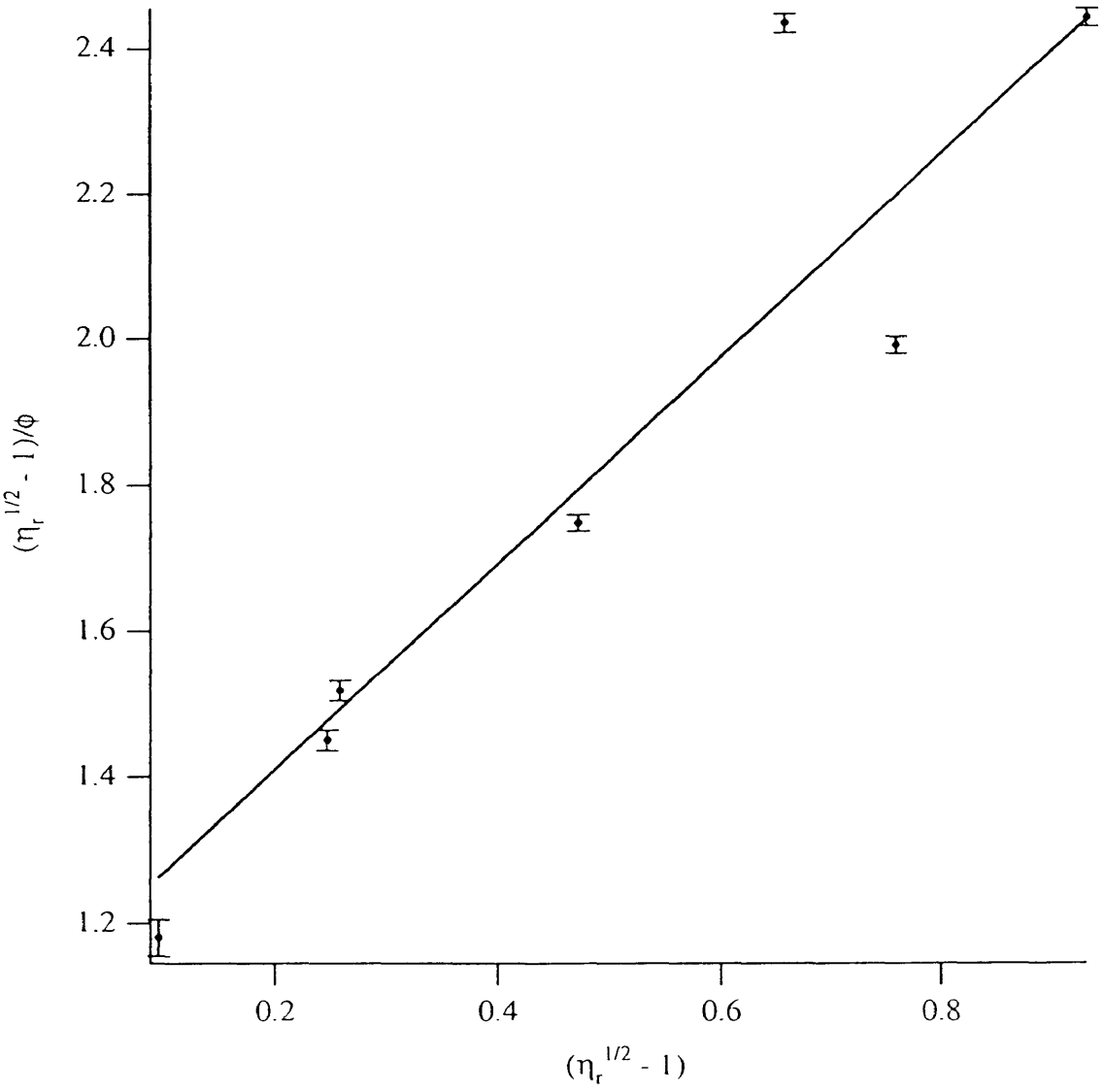

Figure A.17: $(\eta_r^{1/2} - 1)/\phi$ versus $(\eta_r^{1/2} - 1)$. ρ_{filler} = 1.50 g/cm^3; τ = 3.00E+05 dyne/cm^2. ϕ_m=0.709±0.010, $[\eta]$=2.255±0.024.

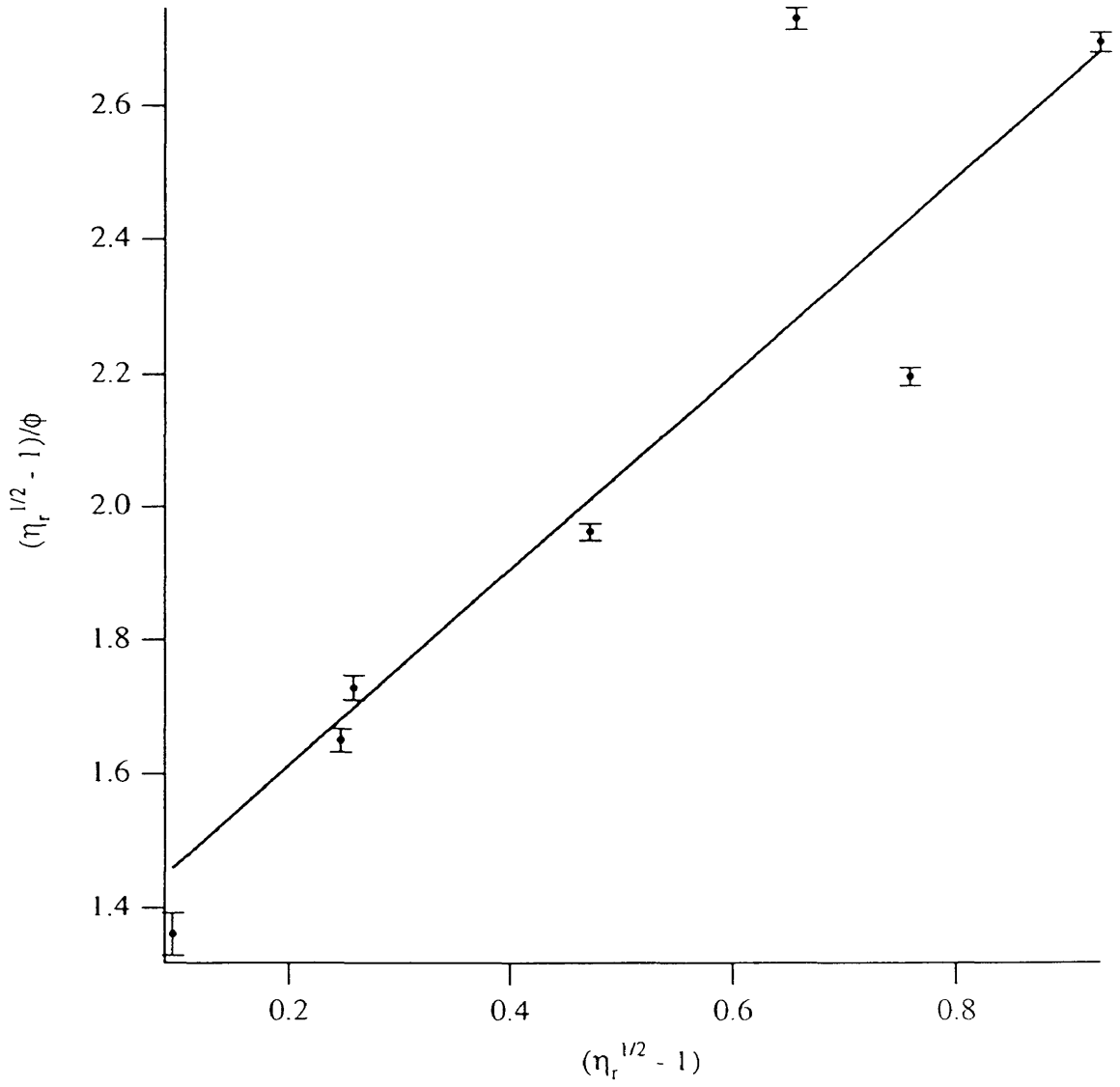

Figure A.18: $(\eta_r^{1/2} - 1)/\phi$ versus $(\eta_r^{1/2} - 1)$. ρ_{filler} = 1.75 g/cm^3; τ = 3.00E+05 dyne/cm^2. ϕ_m=0.684±0.011, $[\eta]$=2.640±0.030.

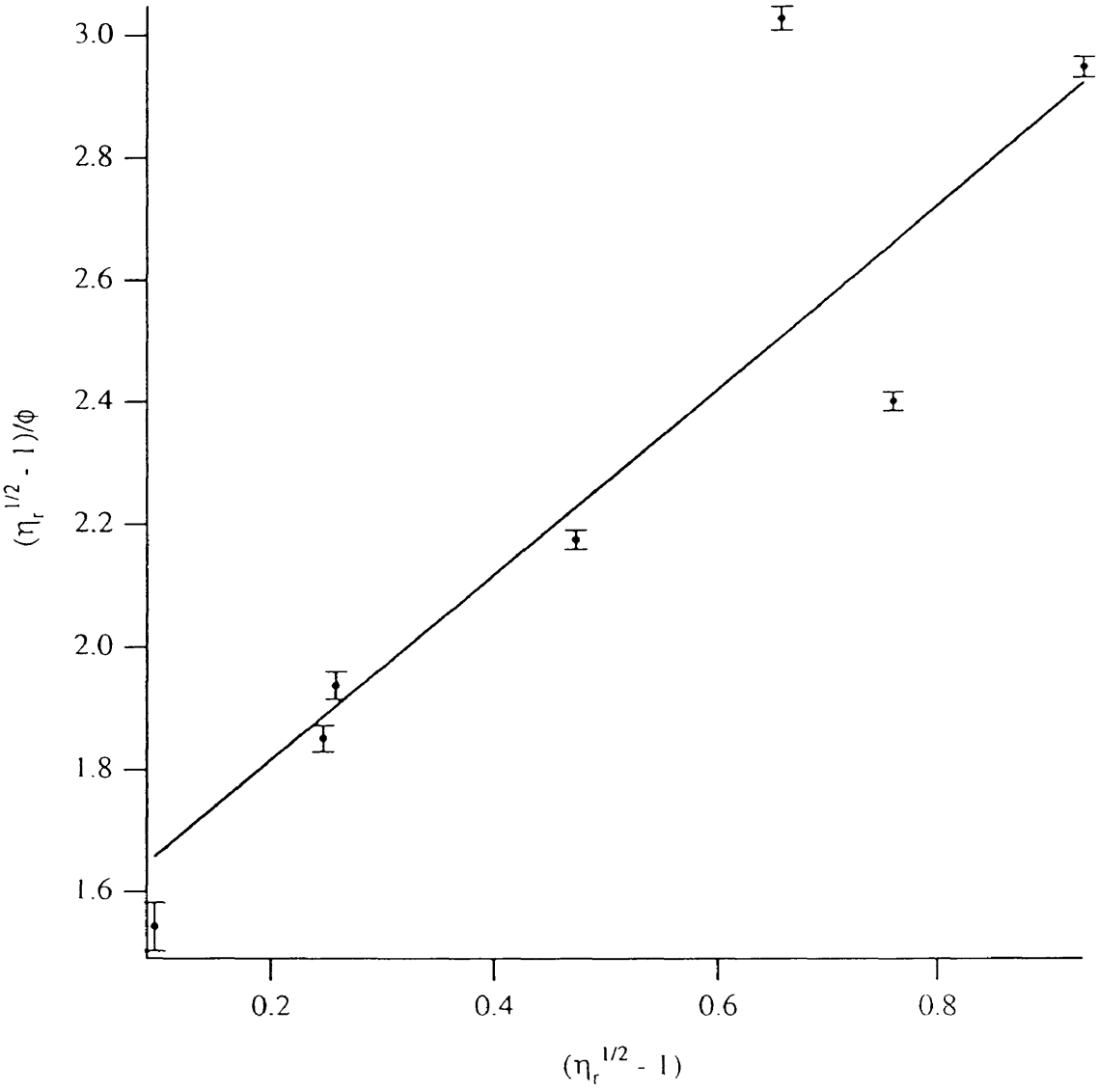

Figure A.19: $(\eta_r^{1/2} - 1)/\phi$ versus $(\eta_r^{1/2} - 1)$. ρ_{filler} = 2.00 g/cm^3; τ = 3.00E+04 dyne/cm^2. ϕ_m=0.661±0.013, $[\eta]$=3.025±0.036.

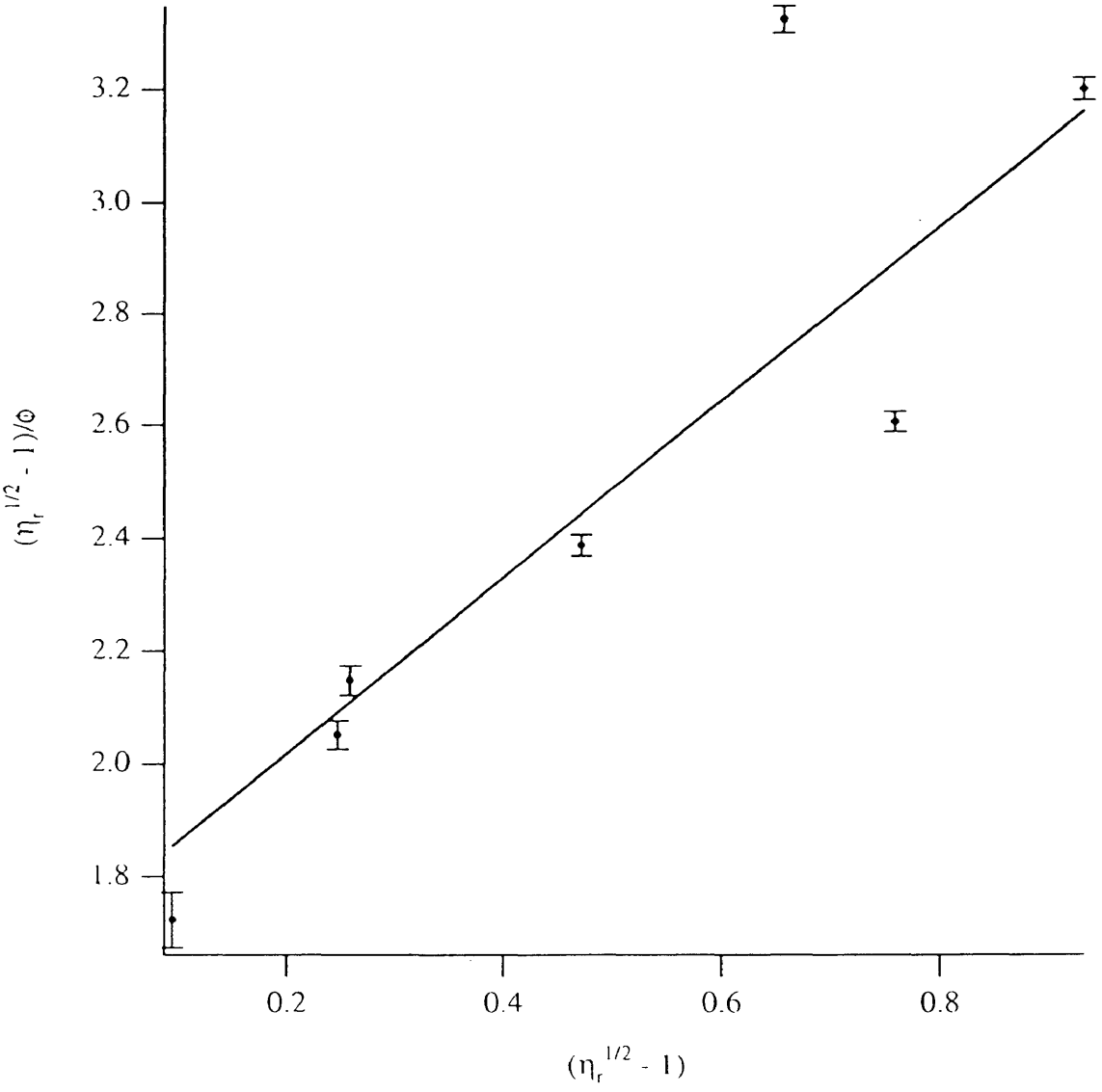

Figure A.20: $(\eta_r^{1/2} - 1)/\phi$ versus $(\eta_r^{1/2} - 1)$. ρ_{filler} = 2.25 g/cm^3; τ = 3.00E+04 dyne/cm^2. ϕ_m=0.639±0.014, $[\eta]$=3.409±0.043.

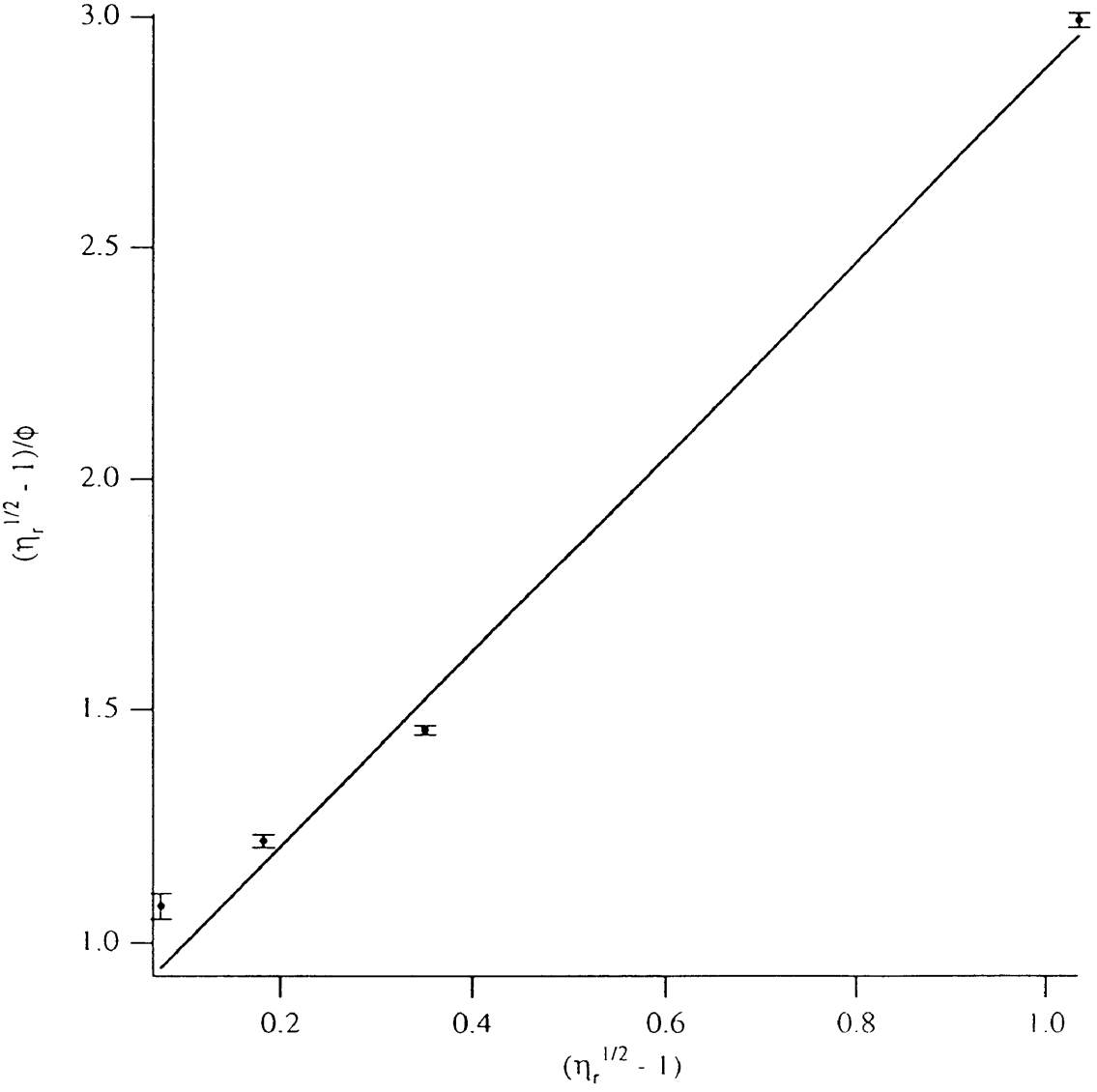

Figure A.21: $(\eta_r^{1/2} - 1)/\phi$ versus $(\eta_r^{1/2} - 1)$. ρ_{filler} = 1.75 g/cm^3; τ = 1.60E+04 dyne/cm^2, T=165^{o}C. ϕ_m=0.471$\pm$5.24E-03.

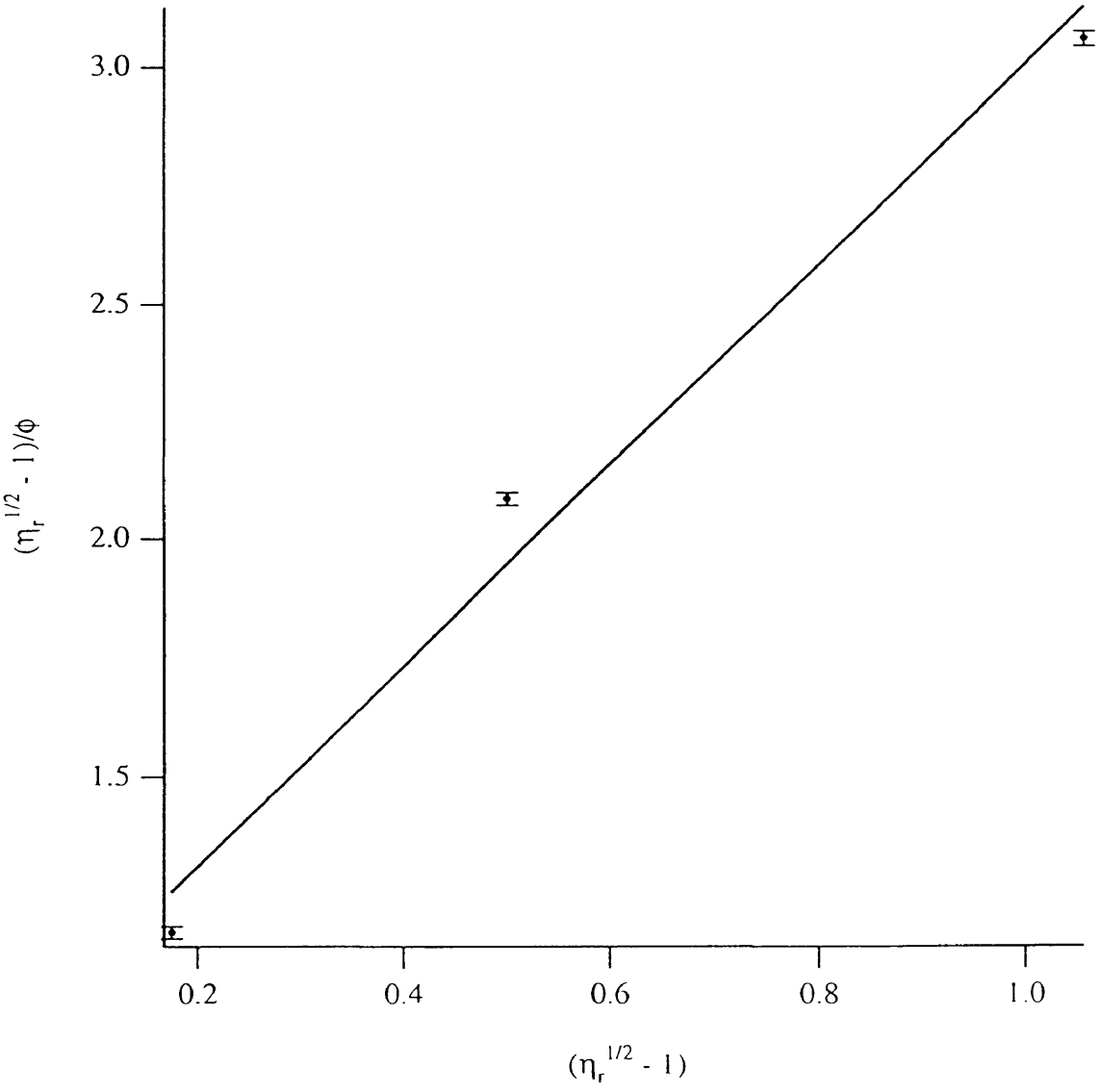

Figure A.22: $(\eta_r^{1/2} - 1)/\phi$ versus $(\eta_r^{1/2} - 1)$. ρ_{filler} = 1.75 g/cm^3; τ = 1.60E+04 dyne/cm^2, T=145°C. ϕ_m=0.476±5.02E-03.

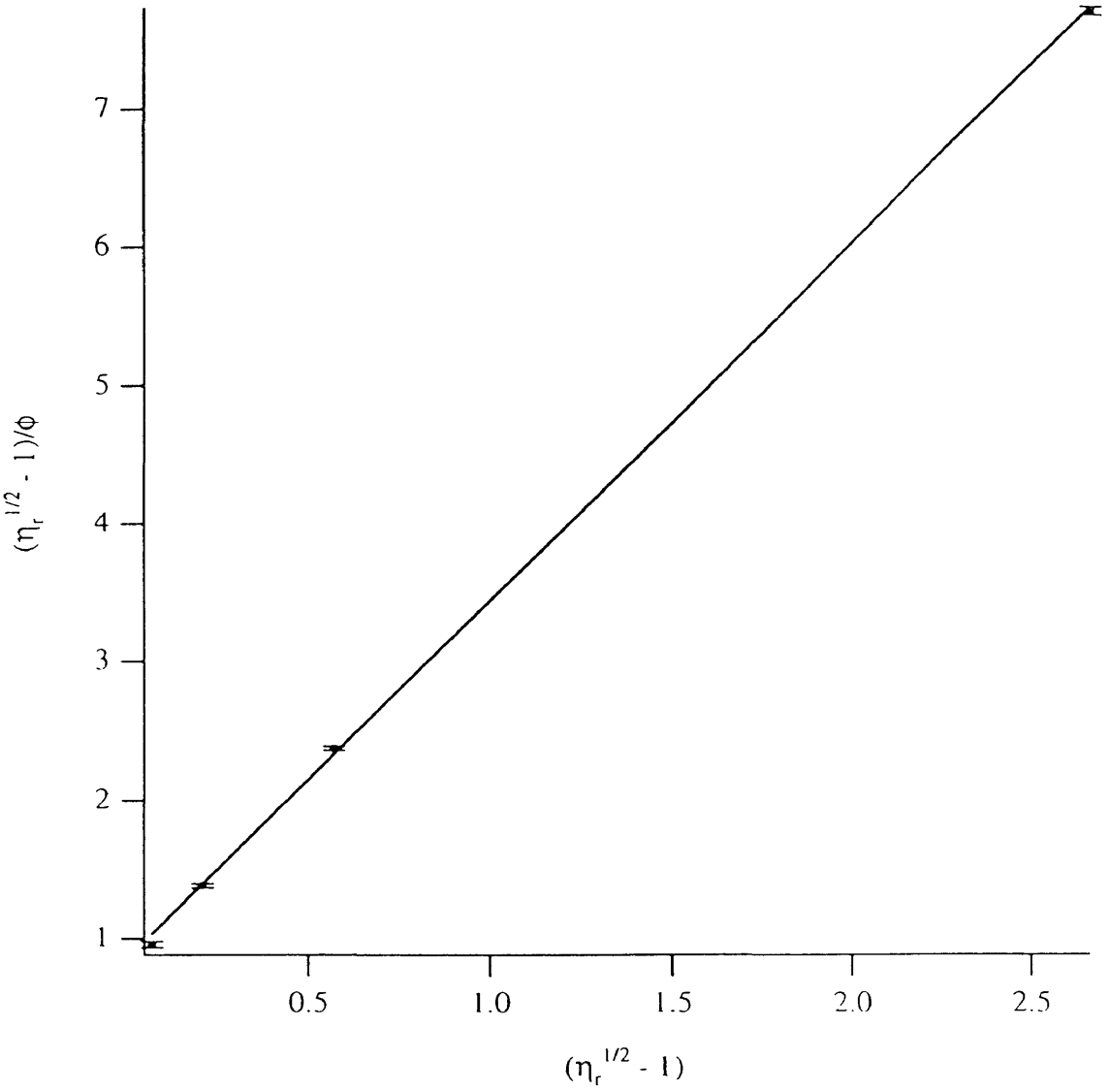

Figure A.23: $(\eta_r^{1/2} - 1)/\phi$ versus $(\eta_r^{1/2} - 1)$. ρ_{filler} = 1.75 g/cm^3; τ = 1.60E+04 dyne/cm^2, T=185°C. ϕ_m=0.367±1.99E-03.

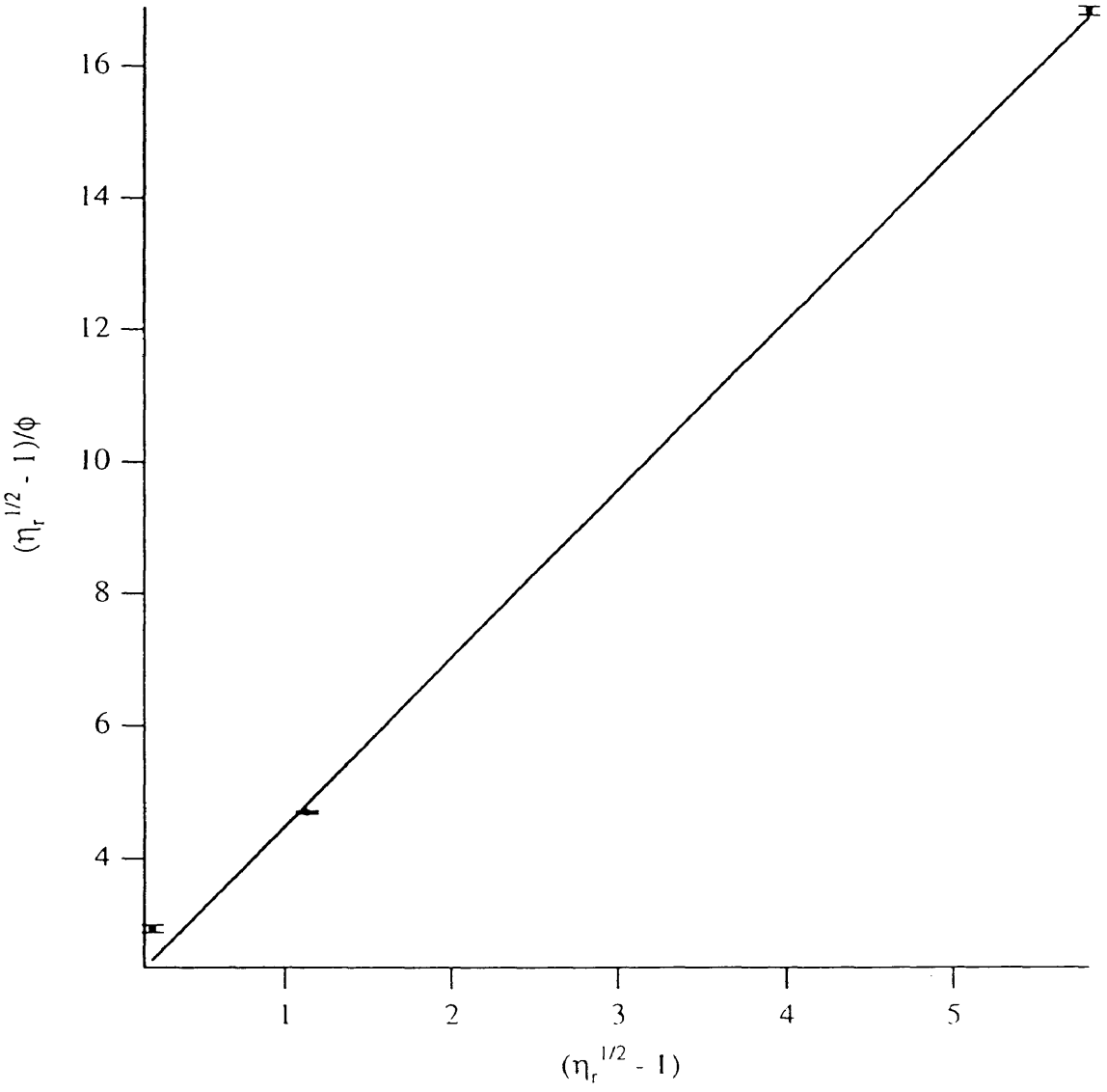

Figure A.24: $(\eta_r^{1/2} - 1)/\phi$ versus $(\eta_r^{1/2} - 1)$. ρ_{filler} = 1.75 g/cm^3; τ = 1.60E+04 dyne/cm^2, T=195°C. ϕ_m=0.393±2.15E-03.

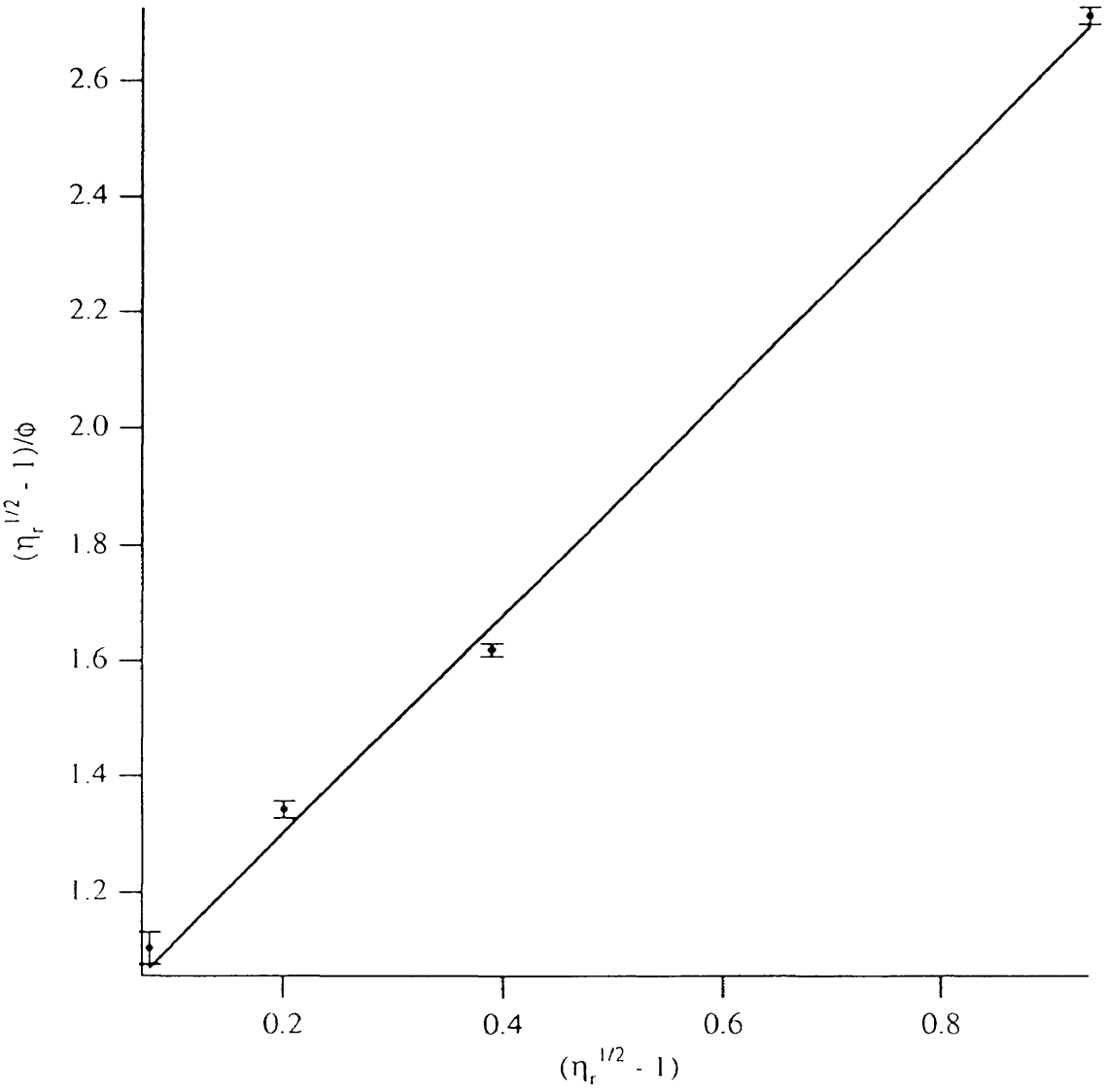

Figure A.25: $(\eta_r^{1/2} - 1)/\phi$ versus $(\eta_r^{1/2} - 1)$. ρ_{filler} = 1.75 g/cm^3; τ = 1.00E+05 dyne/cm^2, T=145°C. ϕ_m=0.530±7.11E-03.

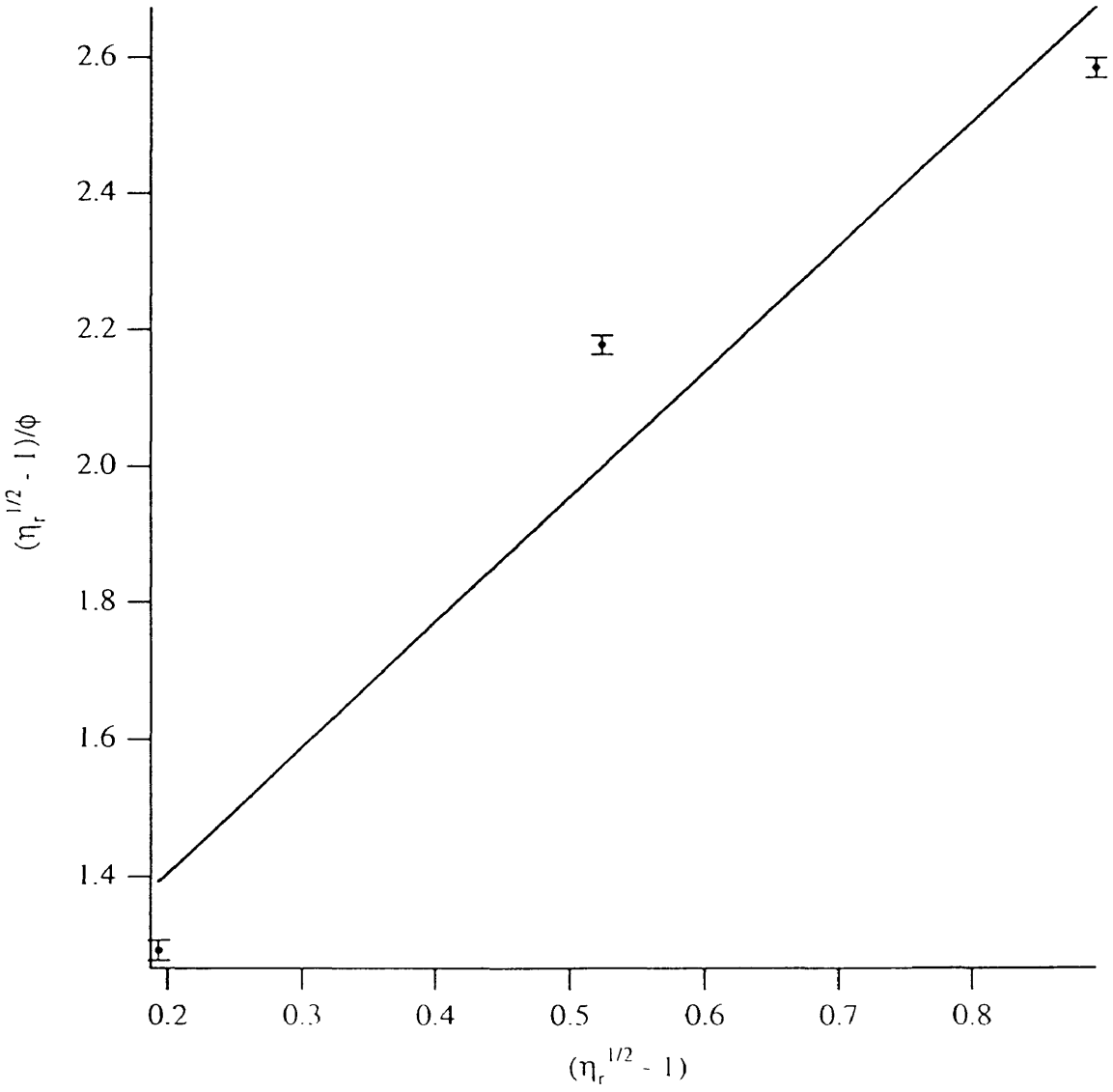

Figure A.26: $(\eta_r^{1/2} - 1)/\phi$ versus $(\eta_r^{1/2} - 1)$. ρ_{filler} = 1.75 g/cm^3; τ = 1.00E+05 dyne/cm^2, T=165°C. ϕ_m=0.546±8.75E-03.

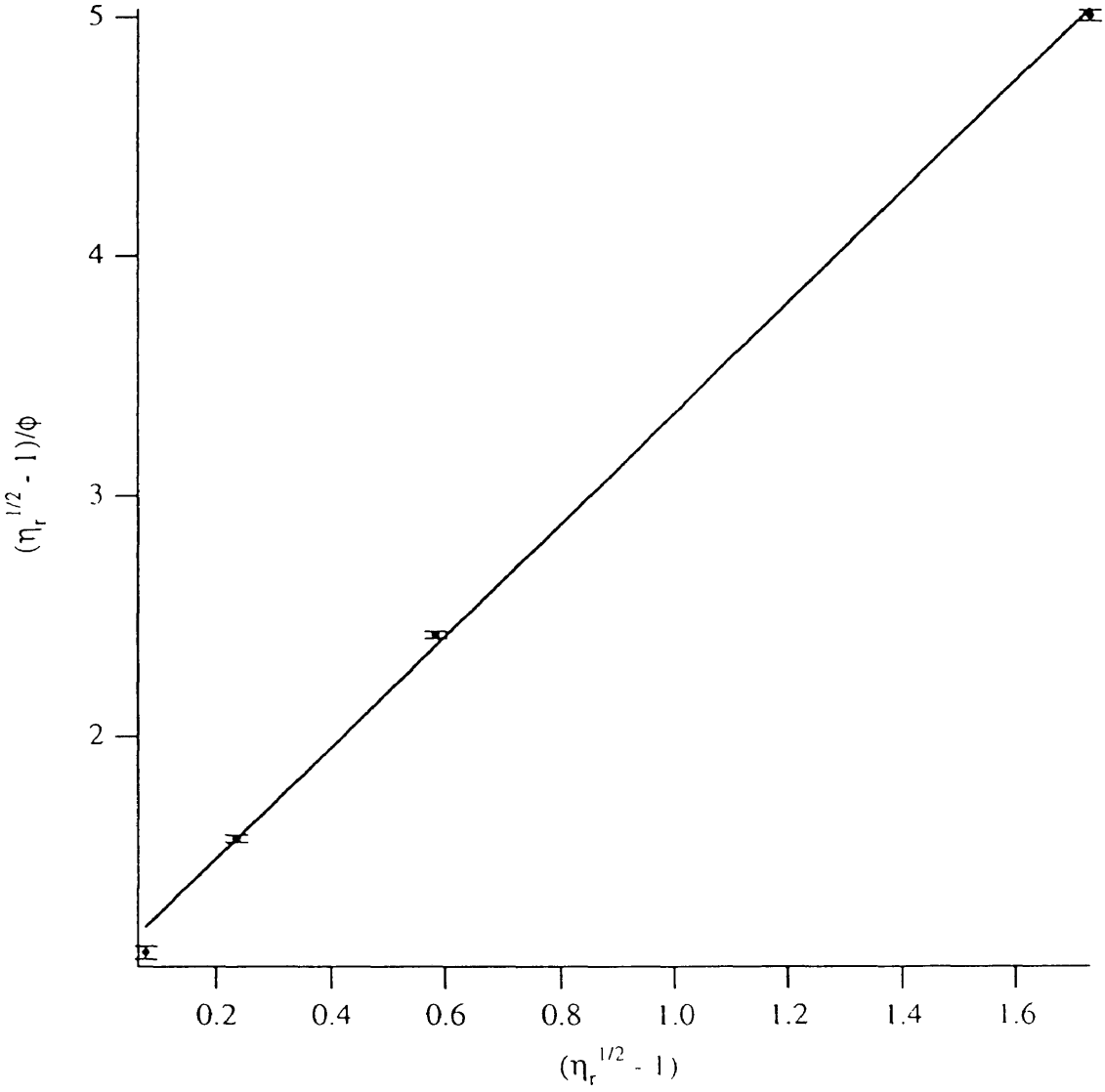

Figure A.27: $(\eta_r^{1/2} - 1)/\phi$ versus $(\eta_r^{1/2} - 1)$. ρ_{filler} = 1.75 g/cm^3; τ = 1.00E+05 dyne/cm^2, T=185°C. ϕ_m=0.431±3.13E-03.

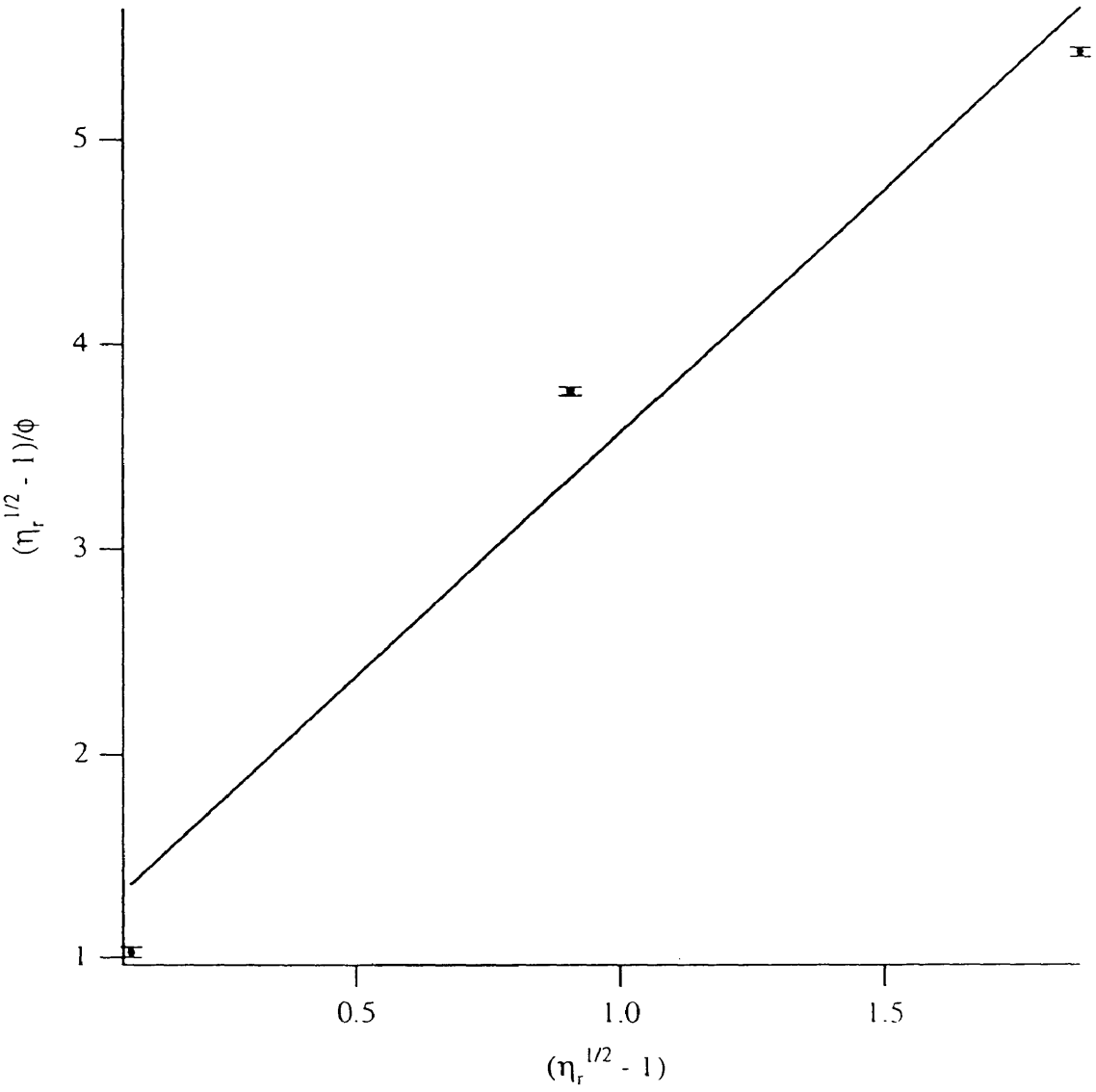

Figure A.28: $(\eta_r^{1/2} - 1)/\phi$ versus $(\eta_r^{1/2} - 1)$. ρ_{filler} = 1.75 g/cm^3; τ = 1.00E+05 dyne/cm^2, T=195°C. ϕ_m=0.421±3.42E-03.

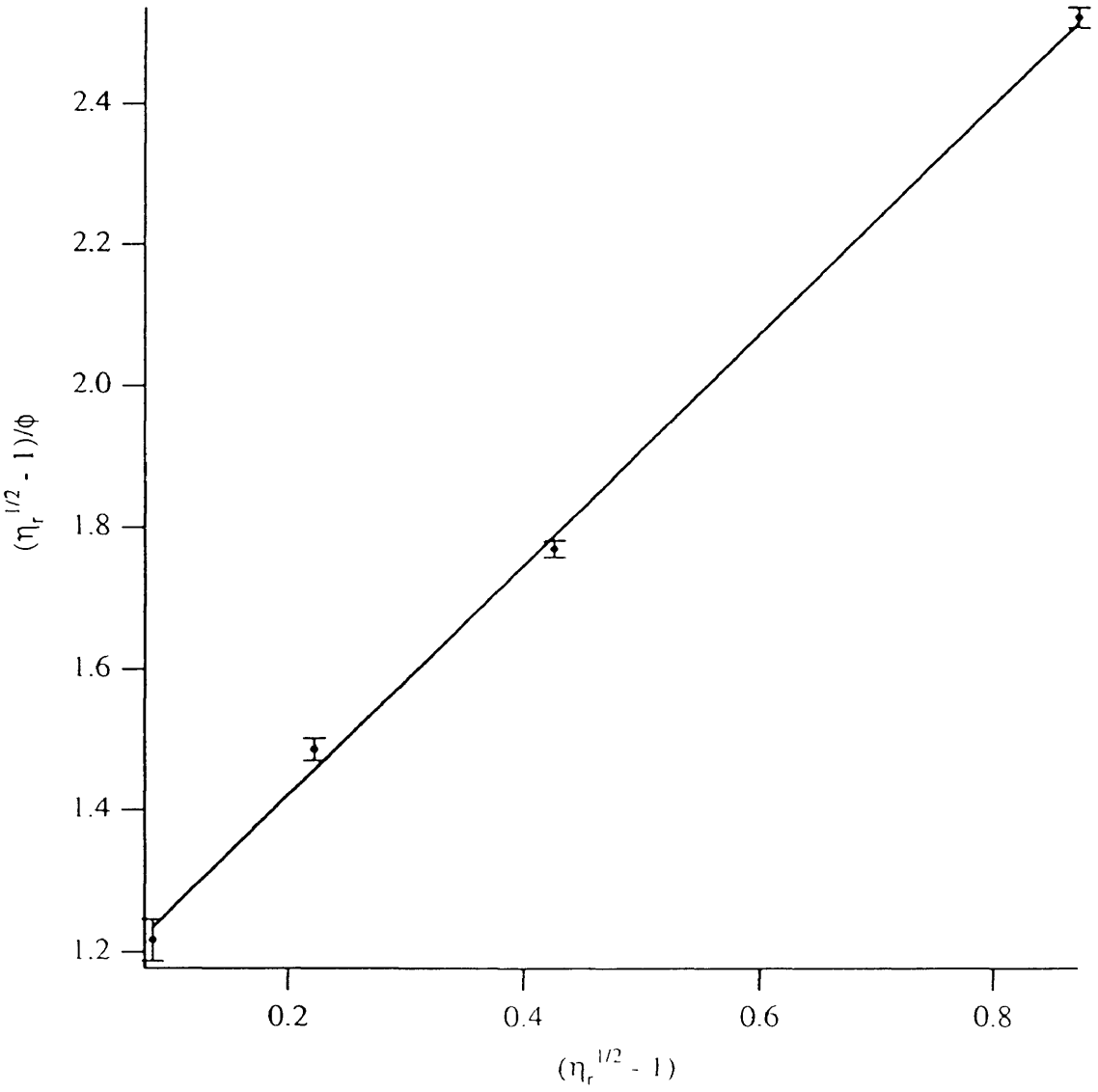

Figure A.29: $(\eta_r^{1/2} - 1)/\phi$ versus $(\eta_r^{1/2} - 1)$. ρ_{filler} = 1.75 g/cm^3; τ = 2.00E+05 dyne/cm^2, T=145°C. ϕ_m=0.613±0.011.

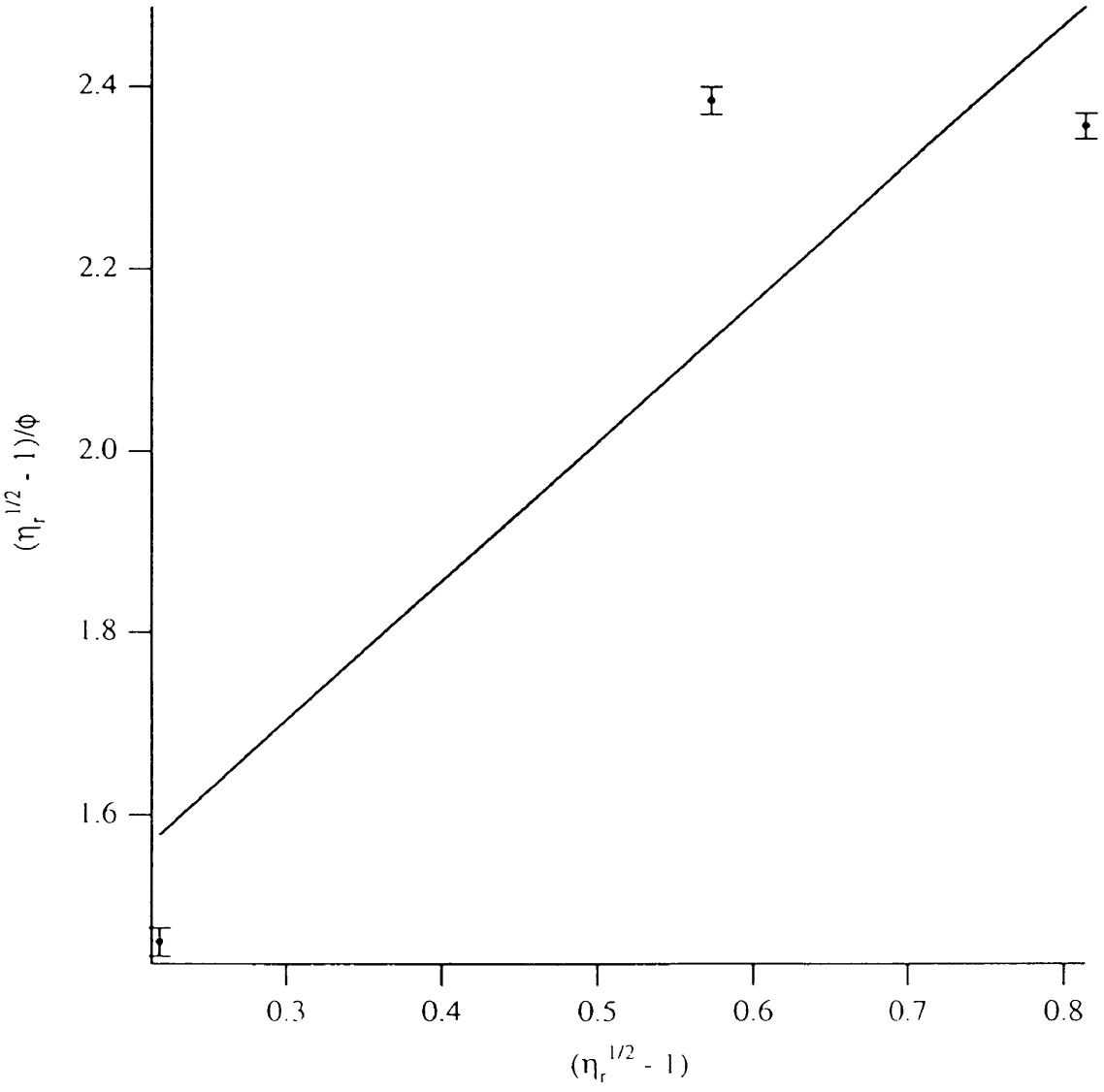

Figure A.30: $(\eta_r^{1/2} - 1)/\phi$ versus $(\eta_r^{1/2} - 1)$. $\rho_{filler} = 1.75$ g/cm^3; $\tau = 2.000$E+05 dyne/cm^2, T=165°C. ϕ_m=0.653±0.015.

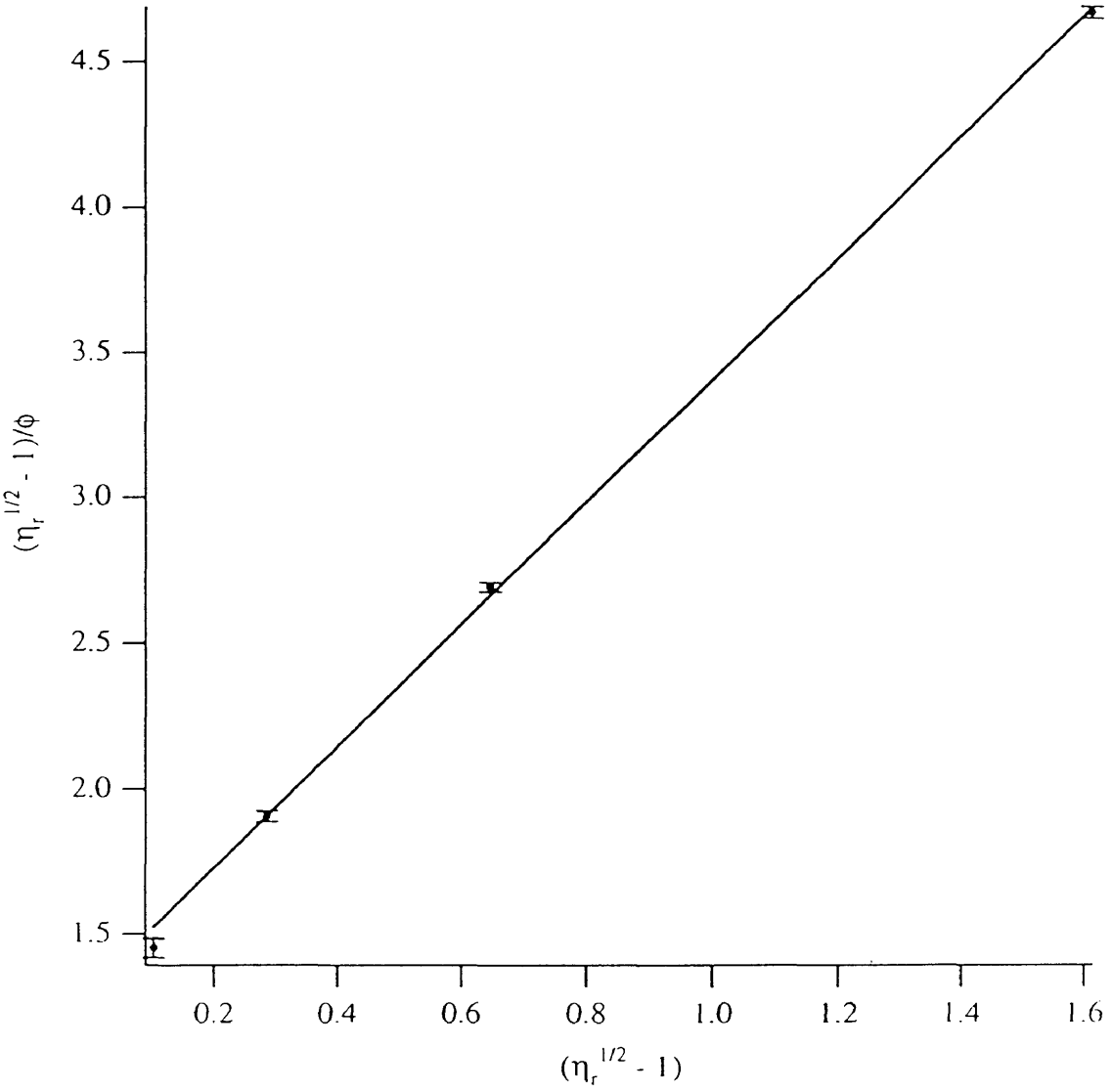

Figure A.31: $(\eta_r^{1/2} - 1)/\phi$ versus $(\eta_r^{1/2} - 1)$. ρ_{filler} = 1.75 g/cm^3; τ = 2.00E+05 dyne/cm^2, T=185^{o}C. ϕ_m=0.478±4.36E-03.

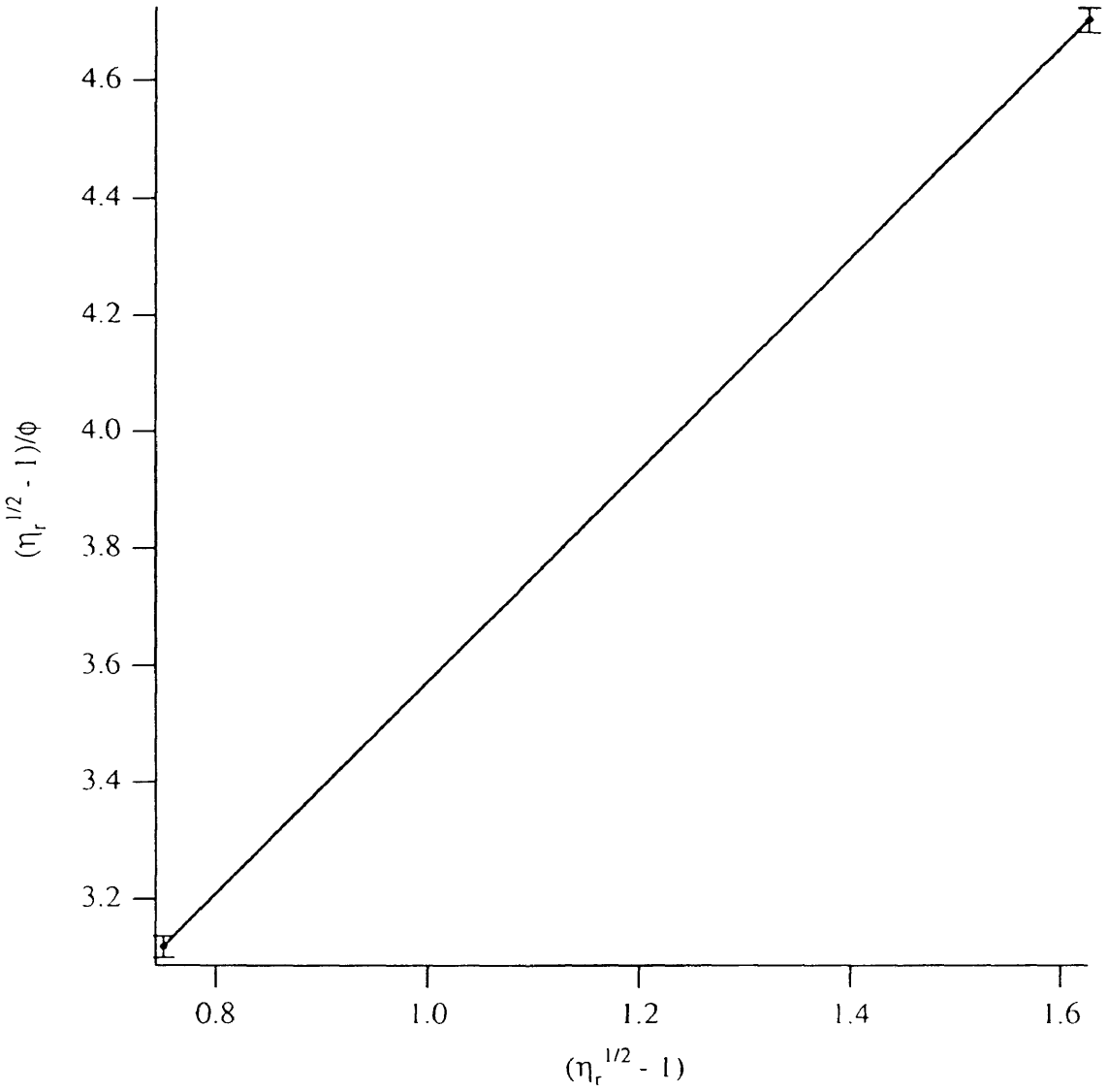

Figure A.32: $(\eta_r^{1/2} - 1)/\phi$ versus $(\eta_r^{1/2} - 1)$. ρ_{filler} = 1.75 g/cm^3; τ = 2.00E+05 dyne/cm^2, T=195°C. ϕ_m=0.552±9.72E-03.

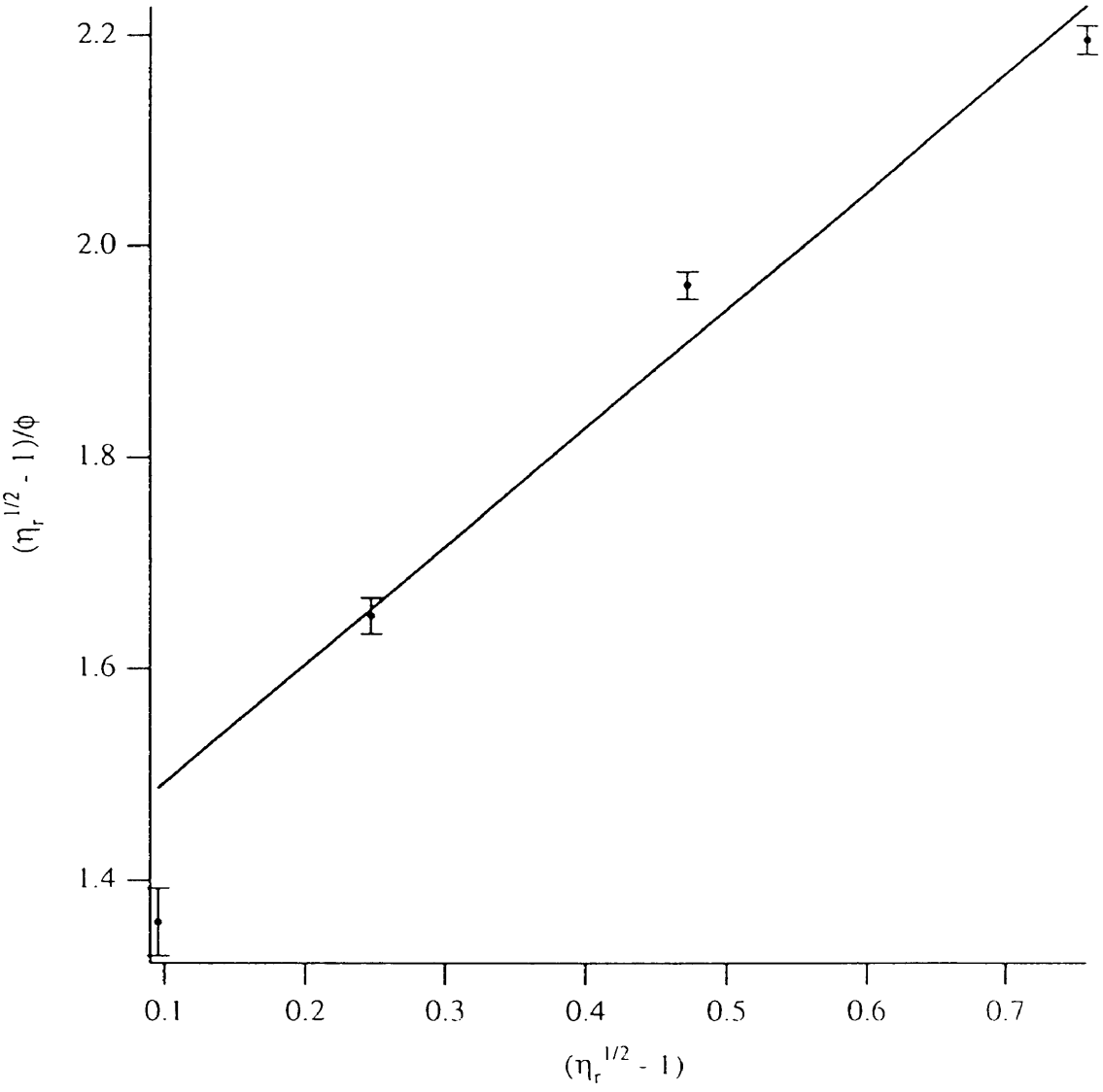

Figure A.33: $(\eta_r^{1/2} - 1)/\phi$ versus $(\eta_r^{1/2} - 1)$. ρ_{filler} = 1.75 g/cm^3; τ = 3.00E+05 dyne/cm^2, T=145°C. ϕ_m=0.895±0.029.

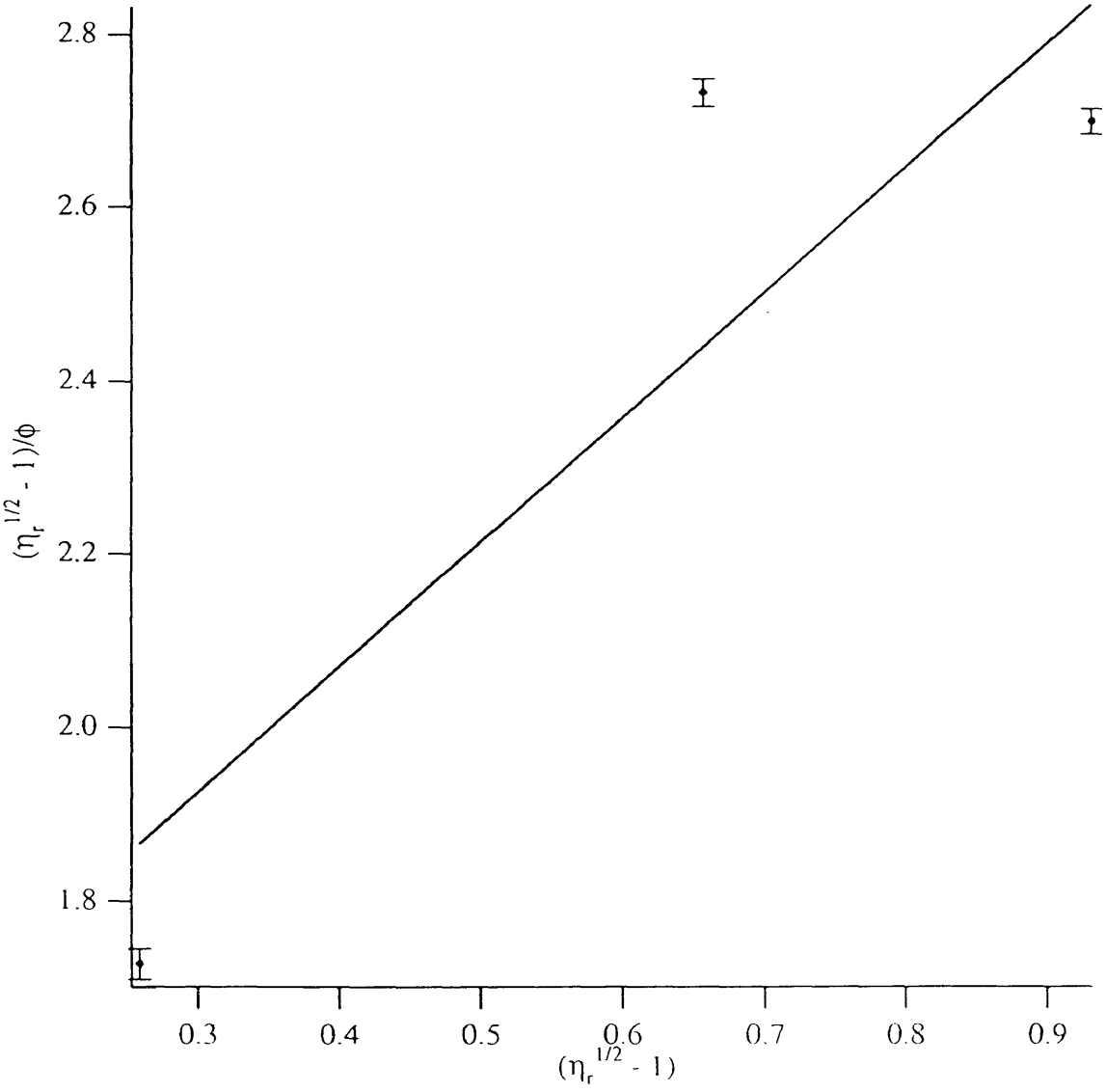

Figure A.34: $(\eta_r^{1/2} - 1)/\phi$ versus $(\eta_r^{1/2} - 1)$. ρ_{filler} = 1.75 g/cm^3; τ = 3.00E+05 dyne/cm^2, T=165°C. ϕ_m=0.696±0.017.

Appendix B

SUPPLEMENTARY MATERIALS ANALYSIS

This appendix contains the particulate analysis completed for the surrogate waste salt filler. Measurements of particle size and particle size distribution were made using sieve separations and SEM techniques. Charges of 50 grams of spray dried salt were placed in the sieve setup listed in Table B.1. The sieves were vibrated for 30 minutes and particles retained in each sieve were weighed.

The results from the sieve analysis were then subjected to SEM and image analysis. The SEM micrographs (see Figures B.1 and B) were used by a Leco Image Analyzer; Feret averages were determined. Five micrographs were used to generate one histogram. An average particle size of 28 microns was determined (see Figure B.2).

Mesh Size	Opening Size	
"#"	microns	inches
100	150	0.0059
140	106	0.0041
200	75	0.0029

Table B.1: Sieve setup for spray dried salt particle analysis.

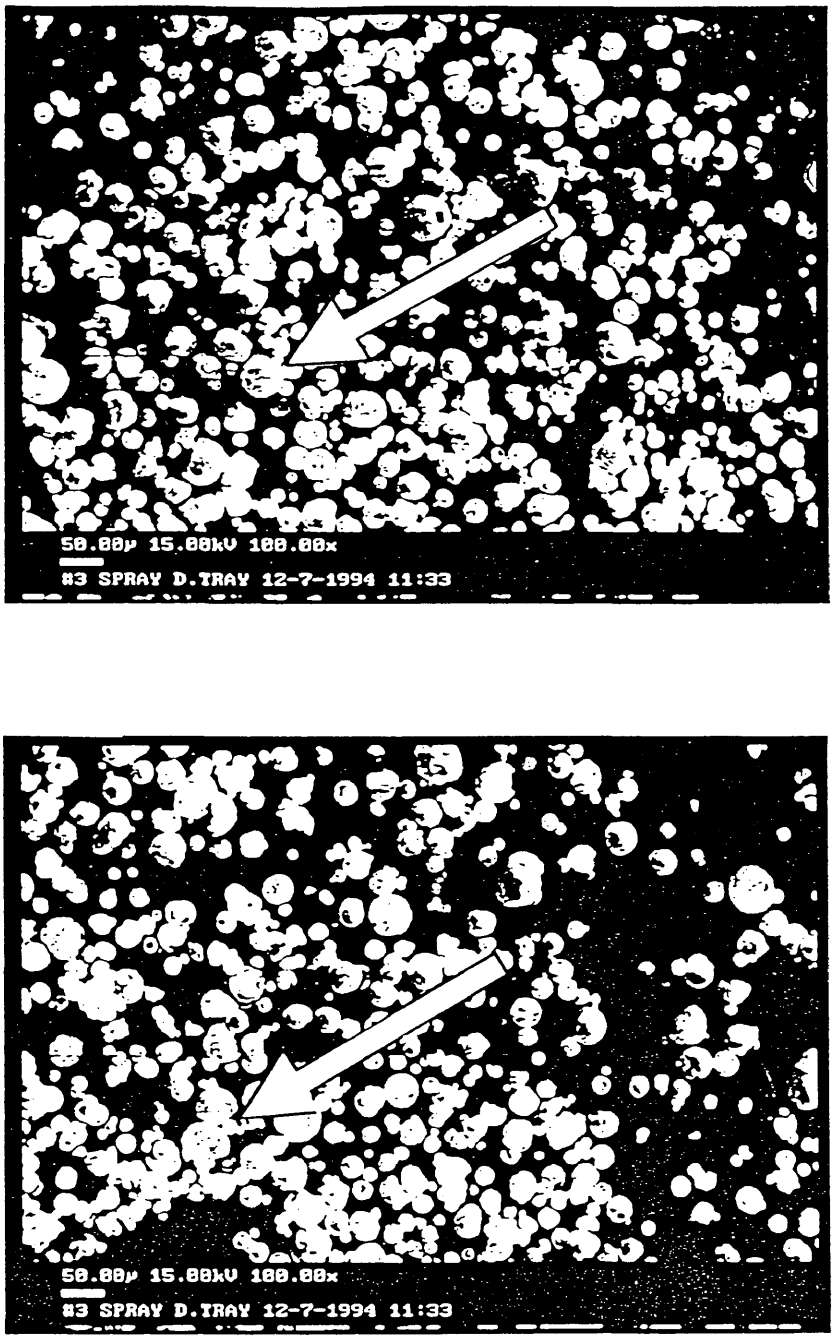

Figure B.1: SEM images of spray dried salt used for image analysis. Notice (arrow) that the particle are indeed hollow spheres which may be crushed during the extrusion operation.

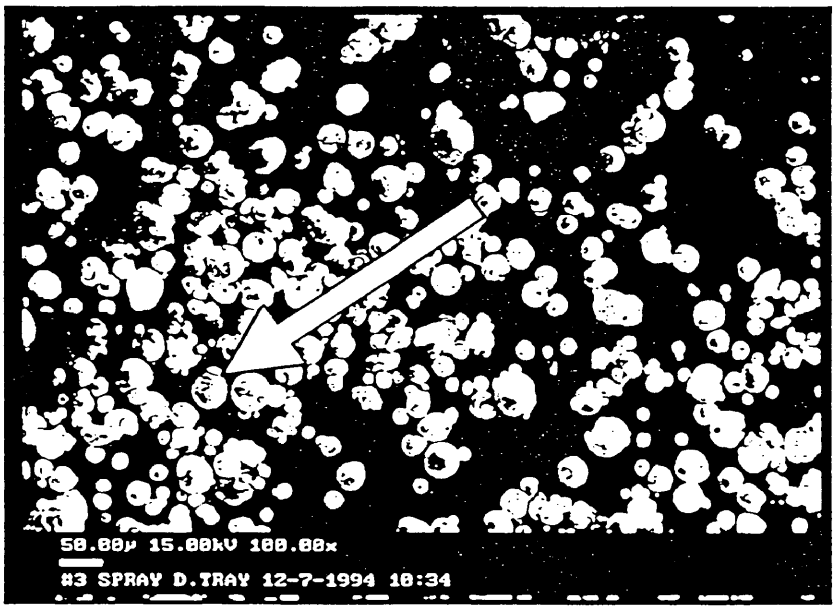

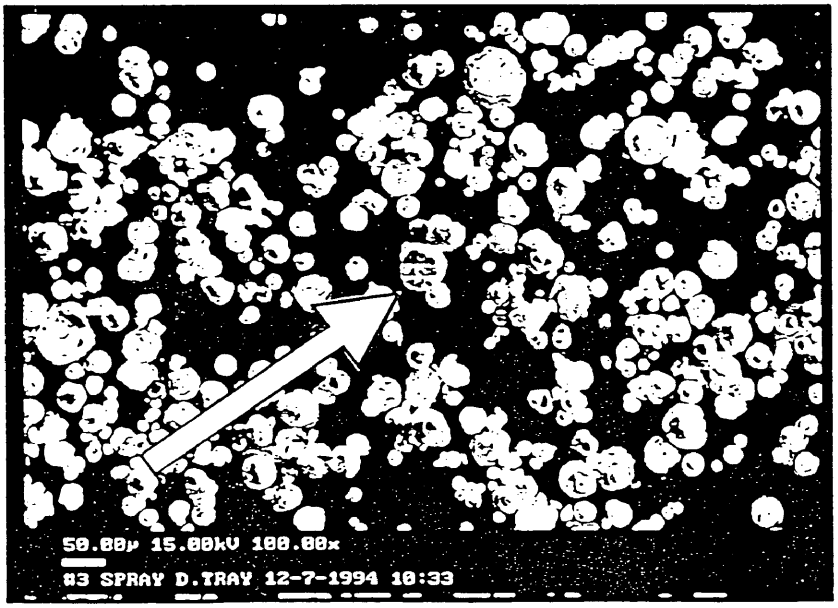

Figure B.1: SEM images continued.

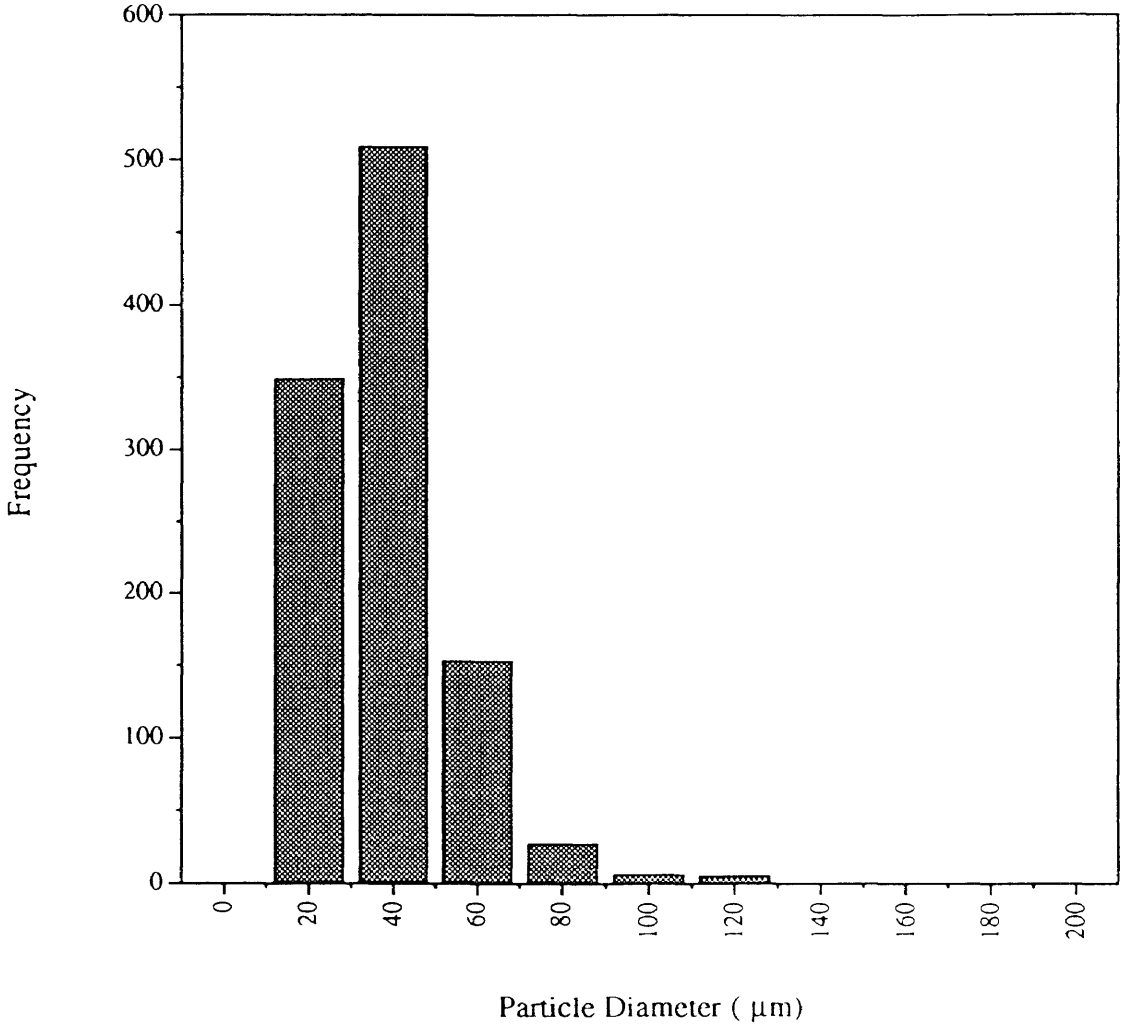

Figure B.2: Histogram generated from image analysis of spray dried salt SEM images.

Thermal analysis of the filled samples was completed to elucidate some the the degradation observed during rheological experimentation. Samples were charged to a Thermogravimetric analyzer and run under conditions of pure N_2 and 30% O_2 (He balance). The analysis scanned in temperature until combustion. The results for pure N_2 are shown in Figure B.3; Figure B.4 shows results under an air atmosphere.

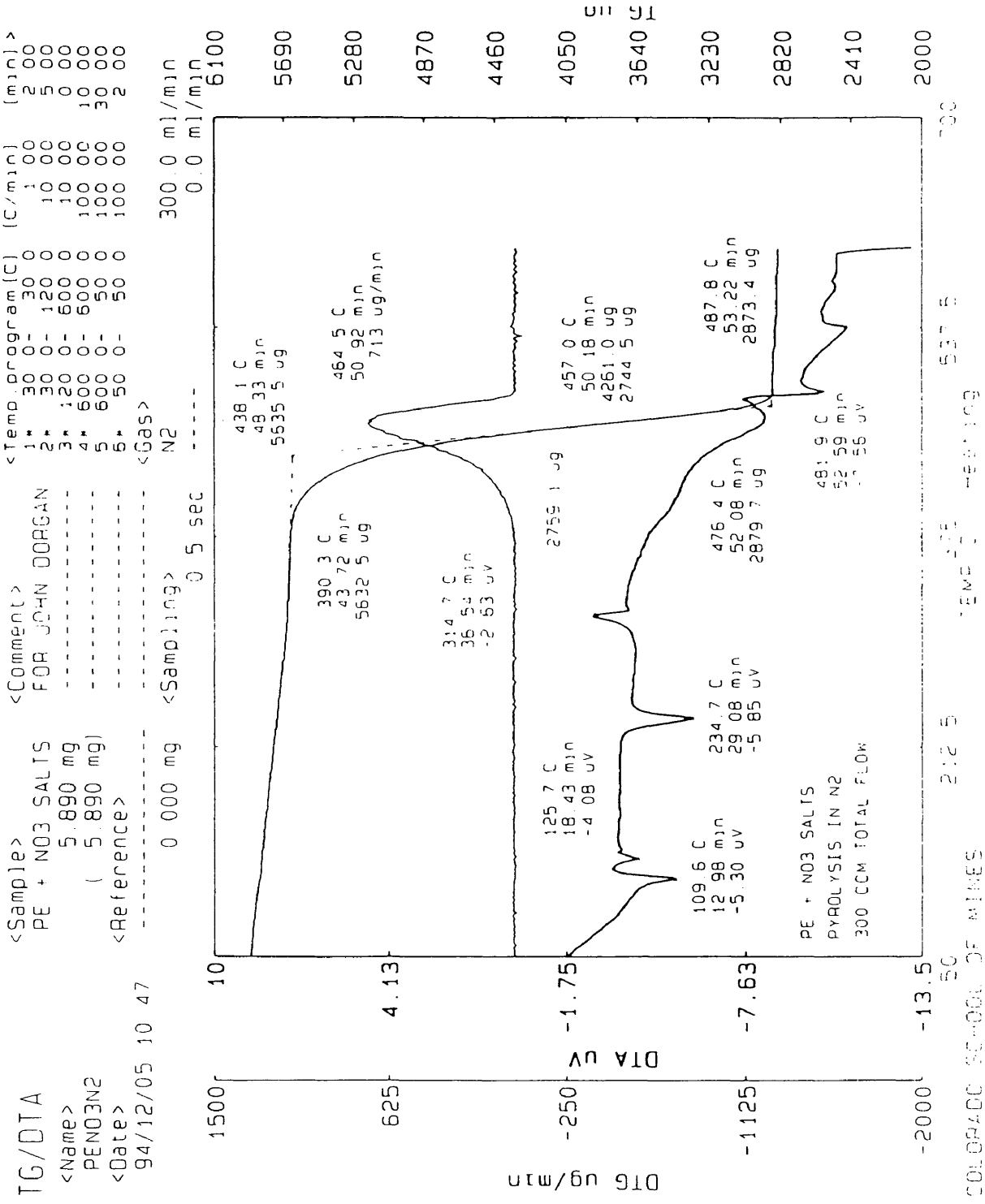

Figure B.3: TGA result for surrogate nitrate salt filled LDPE under pure N_2 sweep gas.

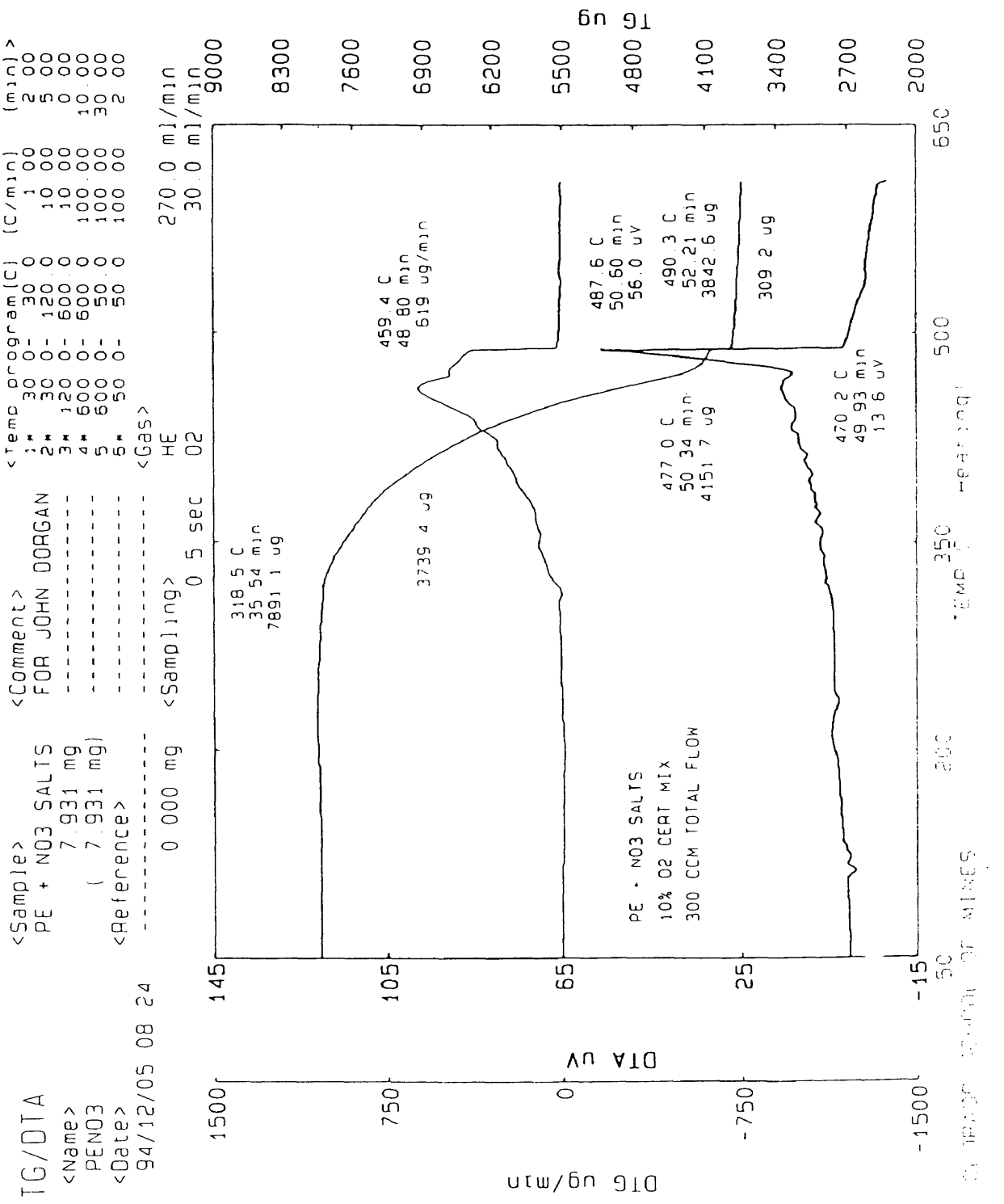

Figure B.4: TGA result for surrogate nitrate salt filled LDPE under conditions of air (30% O_2).